OBSERVABILITY OF THE SCATTERING CROSS-SECTION FOR STRONG AND WEAK SCATTERING

OBSERVABILITY
OF THE
SCATTERING CROSS-SECTION
FOR
STRONG AND WEAK SCATTERING

BY
PATRICK FAYARD , D. Eng.

A THESIS
SUBMITTED TO THE
DEPARTMENT OF ELECTRICAL & COMPUTER ENGINEERING
AND THE SCHOOL OF GRADUATE STUDIES
OF MCMASTER UNIVERSITY
IN PARTIAL FULFILLMENT OF THE REQUIREMENTS
FOR THE DEGREE OF
PH.D DEGREE

Ph.D degree (2010)	McMaster University
(electrical & computer engineering)	Hamilton, Ontario, Canada

TITLE:	Observability of the scattering cross-section for strong and weak scattering
AUTHOR:	Patrick Fayard D. Eng.
SUPERVISOR:	Dr. Timothy R. Field
NUMBER OF PAGES:	xv, 147

Acknowledgements

물심양면으로 많은 도움을 주신 현희씨에게 감사드립니다.
옛날옛날에 아유타에서 "애소 티아오 쿠 맞주아오"했습니다.

I would like to thank my relatives and friends who have supported me during the four years it took me to write the present work.

I have beneficiated from useful technical discussions with A. Sinha and S. Amazit, for my papers (Fayard and Field, 2008) and (Fayard and Field, 2010b), respectively. During a visiting summer position at Academia Sinica in 2010, I also had fruitful interactions with my host, Dr. C. Tsai. I am also grateful to the anonymous reviewers whose suggestions have often improved my manuscripts. The LaTeX template used to compile this thesis is due to S. Patel.

I am finally thankful to my supervisor, Dr. T. Field, whose guidance and advices were instrumental in completing my Ph.D. His technical expertise on this research topic proved invaluable.

I acknowledge the following sources of financial support. Raymond Moore Ontario Graduate Scholarship in Science and Technology (OGSST), Yates Travel Scholarship, Summer in Taiwan scholarship from the Research Council of the Republic of China, Irena and Jim Thomas Foundation.

Résumé

L'amplitude diffusée par une surface rugueuse peut-être décrite par une marche aléatoire avec des variations dans le nombre de pas comme proposé par Jakeman. L'idée sous-jacente est de décomposer l'amplitude reçue comme la somme de contributions indépendantes d'un grand nombre de diffuseurs. Si leur population suit un modèle de naissance-mort-immigration, les statistiques qui s'ensuivent obéissent à une distribution de K et une représentation en termes d'une tavelure Gaussien modulée par la surface équivalente radar (SER) peut-être établie. L'objectif de cette thèse est de proposer des techniques permettant d'inférer la SER, en temps réel, pour rendre plus aisée la détection d'anomalies. En premier lieu, nous démontrons comment la classe des diffusions de Pearson, que nous dérivons sur les bases d'un modèle de population prenant des values entières, couvre à la fois la distribution de Gamma (propre à la distribution de K) et d'autres densités de probabilités pour la texture. Ensuite, nous rappelons comment Field et Tough ont dérivé, à partir de la marche aléatoire, l'évolution temporelle et l'auto-corrélation de l'amplitude diffusée dans le cadre du calcul stochastique d'Itō. En particulier, ils ont démontré comment la SER était observable par le truchement du produit de l'intensité et des fluctuations carrées de la phase. Nous poursuivons ce travail en dérivant une expression analytique de l'erreur propre à cette inférence en même temps qu'une condition pour la réduire au minimum. Nous étendons également ces résultats aux diffusions de Pearson dont l'importance dans ce contexte a été précédemment expliquée. Ensuite, nous nous intéressons à un caveat expériemental, la présence d'un bruit blanc Gaussien qui s'ajoute à l'amplitude reçue. Le filtre à réponse impulsionnelle finie de Wiener permet d'obtenir un estimateur idéal pour éliminer ce bruit. Finalement, nous nous intéressons au rayonnement diffusé avec une distribution non-uniforme de phase. La principale différence avec la situation précédente est la structure de la corrélation entre les composantes radiales et angulaires de l'amplitude diffuse. Une étude détaillée de ces caractéristiques géométriques permet de proposer deux techniques distinctes pour estimer la SER, permettant donc de généraliser les résultats obtenus pour une distribution uniforme de phase.

Abstract

Jakeman's random walk model with step number fluctuations describes the amplitude scattered from a rough medium in terms as the coherent summation of (independent) individual scatterers' contributions. For a population following a birth-death-immigration (BDI) model, the resulting statistics are K–distributed and the multiplicative representation of the amplitude as a Gaussian speckle modulated by a Gamma radar cross-section (RCS) is recovered. The main objective of the present thesis is to discuss techniques for the inference of the RCS in local time in order to facilitate anomaly detection. We first show how the Pearson class of diffusions, which we derive on the basis of a discrete population model analogous to the BDI, encompasses this Gamma texture as well as other texture models studied in the literature. Next we recall how Field & Tough derived, in an Ito calculus framework, the dynamics and the auto-correlation function of the scattered amplitude from the random walk model. In particular, they showed how the RCS was observable through the intensity-weighted squared fluctuations of the phase. Thanks to a discussion of the sources of discrepancy arising during this process, we derive an analytical expression for the inference error based on its asymptotic behaviours, together with a condition to minimize it. Our results are then extended to the Pearson class of diffusions whose importance for radar clutters is described. Next, we consider an experimental caveat, namely the presence of an additional white noise. The finite impulse response Wiener filter enables the design of the optimal filter to retrieve the scattered amplitude when it lies in superposition with thermal noise, thus enabling the usage of our inference technique. Finally, we consider weak scattering when a coherent signal lies in superposition with the aforementioned (strongly) scattered amplitude. Strong and weak scattering patterns differ regarding the correlation structure of their radial and angular fluctuations. Investigating these geometric characteristics yields two distinct procedures to infer the scattering cross-section from the phase and intensity fluctuations of the weakly scattered amplitude, thus generalizing the results obtained in the strong scattering case.

List of Contributions

- P. Fayard and T.R. Field. "Optimal inference of the scattering cross-section through the phase de-coherence". *Waves Rand. Comp. Media*, 18(4):571–584, Nov 2008.

- P. Fayard and T.R. Field. "Optimal inference of the inverse Gamma texture for a compound-Gaussian clutter". In *2009 IEEE ICASSP*, pages 2969–2972, Apr 2009.

- P. Fayard and T.R. Field. "Inference of a generalized texture for a compound–Gaussian clutter". *IET Radar, Sonar and Navigation*, 4(2):187–194, Apr 2010a.

- P. Fayard and T.R. Field. "Estimation of the K–scattered amplitude in additive noise". *IEEE Aero. Elec. Syst.*, 7, October 2010b[1].

- P. Fayard and T.R. Field. "Geometrical implications of the compound representation for weakly scattered amplitudes". *Waves Rand. Comp. Media*, in press, 2010c.

- P. Fayard and T.R. Field. "Discrete models for scattering populations". *J. Appl. Proba*, under review, 2010d.

[1]for this paper, the authors' names are given in alphabetical order

"Entre le sexe et les mathématiques, il n'existe rien ! Rien ! C'est le vide !"

Louis-Ferdinand Céline

Contents

Acknowledgements iii

Résumé iv

Abstract v

Publications vi

Table of contents viii

List of Figures xiii

List of Tables xv

1 Introduction 1

1.1 Radars in a maritime environment . . . 1
1.2 Existing techniques . . . 2
1.3 Observability of the cross-section . . . 5
1.4 Organization of the thesis . . . 9

2 Scattering from random media 13

2.1 Scattering from a rough surface . . . 13
2.1.1 Physical description . . . 13
2.1.2 Gaussian statistics . . . 15
2.1.3 Step number fluctuations . . . 18
2.1.4 Texture and local power . . . 20
2.1.5 Moments . . . 21
2.2 Diffusion model for the scattering cross-section . . . 22
2.2.1 Fokker–Planck description . . . 22
2.2.2 Birth-death-immigration process . . . 24
2.2.3 Continuous limit . . . 25
2.2.4 The K–distribution . . . 27

2.3 Extension to other diffusion models 28
2.3.1 Class of Pearson diffusions 28
2.3.1.1 Definition 28
2.3.1.2 Importance for scattering applications 29
2.3.2 Associated population model 31
2.3.3 Observability of associated population model 33

3 Dynamical stochastic model **37**
3.1 Random walk model and compound presentation 37
3.1.1 Rayleigh scattering 37
3.1.2 Compound representation 40
3.2 Strong scattering dynamics 41
3.2.1 Field equation 41
3.2.2 Intensity and phase dynamics 43
3.2.3 Correlation of fluctuations 45
3.3 Weak scattering dynamics 45
3.3.1 Definition 45
3.3.2 Scattering dynamics 47
3.4 Spectral properties of the K–distributed noise 49
3.4.1 Autocorrelation function 49
3.4.2 Spectral properties of the scattered intensity 51
3.5 Numerical methods 52
3.5.1 Rationale 52
3.5.2 Cross-section 55
3.5.3 Strong scattering 55
3.5.4 Weak scattering 55

4 Observability of the RCS for strong scattering **59**
4.1 Intensity-weighted fluctuations of the phase 59
4.1.1 Objective 59
4.1.2 Inference 60
4.1.3 Experimental implications 62
4.1.4 Examples 63
4.1.4.1 Gamma distributed texture 63
4.1.4.2 Other Pearson distributions 63
4.1.5 Anomaly detection: toy example 64
4.2 Optimization 66
4.2.1 Propositions 66
4.2.2 Proof 68
4.2.2.1 Rationale 68

4.2.2.2 Error due to the x_i's . . . 69
4.2.2.3 Error due to the n_i's . . . 72
4.2.3 Evaluation of Δ^{opt} . . . 72
4.2.4 Experiment . . . 73
4.2.5 Sensitivity to parameters . . . 74
4.2.6 Extension for a generalized population . . . 77
4.3 Scattered amplitude in additive noise . . . 78
4.3.1 Additional thermal noise . . . 78
4.3.2 Filtering out the thermal noise . . . 81
4.3.2.1 Filter derivation . . . 81
4.3.2.2 Non-causal solution . . . 82
4.3.2.3 Filtering error . . . 83
4.3.3 Simulation . . . 84
4.3.3.1 Filtering . . . 84
4.3.3.2 Parameter Estimation . . . 85
4.3.3.3 Anomaly detection: additional white noise . . . 87

5 Observability of the RCS for weak scattering 89
5.1 Volatility of a weakly scattered amplitude . . . 89
5.1.1 Objective . . . 89
5.1.2 Decomposition of the amplitude fluctuations . . . 90
5.1.3 Scattering vector . . . 92
5.1.3.1 Proposition . . . 92
5.1.3.2 Proof . . . 93
5.1.4 Geometry of amplitude fluctuations . . . 95
5.2 Geometrical inference of the RCS . . . 98
5.2.1 Phase fluctuations . . . 98
5.2.2 Intensity fluctuations . . . 99
5.3 Experimental implications . . . 100
5.3.1 Phase fluctuations . . . 101
5.3.2 Intensity fluctuations . . . 104
5.4 Discussion . . . 104
5.4.1 Optimization . . . 104
5.4.2 Link with the strong scattering case . . . 105

6 Conclusion 109
6.1 Summary . . . 109
6.2 Discussion . . . 111
6.3 Future research . . . 115

A BDI model **121**

A.1 PDE for the partition function of a BDI model 121

A.2 Partition function for a BDI population 122

A.2.1 Forward Kolmogorov equation 122

A.2.2 Birth-death process 123

A.2.3 Effect of immigration 124

B Ito calculus **127**

B.1 Brownian motion 127

B.1.1 Derivation 127

B.1.2 Properties 128

B.2 Stochastic Differential Equation 129

B.3 Ito integral 129

B.4 Ito's formula 130

B.5 Ito product rule 130

B.6 Stratonovich vs Ito integrals 131

C Useful mathematical facts **133**

C.1 Probability distributions 133

C.1.1 Poisson distribution 133

C.1.2 Negative binomial aka Pascal 134

C.1.3 Gaussian 134

C.1.4 Gamma 134

C.1.5 Cauchy 135

C.1.6 Rayleigh 135

C.1.7 K-distribution 135

C.2 Special functions 136

C.2.1 Bessel functions 136

C.2.2 Gamma function 137

C.2.3 Hypergeometric function 138

C.3 Formulae 138

Bibliography **138**

List of Symbols **149**

List of Acronyms **153**

List of Figures

2.1 Geometry of the random walk 16
2.2 First-order transition rates 23
2.3 Inverse Gamma distribution 30
2.4 Beta distribution of the first kind 30
2.5 Beta prime distribution 31

3.1 Sea-state and parameter α 54
3.2 Dynamics of three Pearson diffusions 54
3.3 Dynamics of the speckle 56
3.4 Dynamics of the K–scattered amplitude 56
3.5 Rice weakly scattered amplitude simulation 57
3.6 HK weakly scattered amplitude simulation 57
3.7 GK weakly scattered amplitude simulation 58

4.1 Inference for a Gamma texture 63
4.2 RCS inference for Pearson diffusions 65
4.3 Presence of a target / RCS inference 66
4.4 Optimization inference process for a Gamma distribution (MSE) . . . 75
4.5 Optimization inference for a Gamma distribution (correlation) 76
4.6 Optimization of the inference Pearson diffusions 79
4.7 Filtering K–distributed scattered amplitude plus white noise 85
4.8 Anomaly detection for a noisy scattered amplitude 88

5.1 Orthogonal dyad for a weakly scattered amplitude 98
5.2 Homodyned weak scattering / Phase fluctuations 102
5.3 Generalized weak scattering / Phase fluctuations 102
5.4 Generalized weak scattering / Intensity fluctuations 103
5.5 Homodyned weak scattering / Intensity fluctuations 103
5.6 Weak scattering inference optimization 106

B.1 Wiener process 129

Chapter 1

Introduction

1.1 Radars in a maritime environment

Since the introduction of radars in the 1930s, their applications to maritime environments have attracted continuing interest (one could reflect upon the fact that the earth is mostly covered with water). Motivated by military demands or more recent civilian uses (e.g., remote-sensing of the environment), a wide body of knowledge was constructed to meet the specificities of sea surfaces. The present work places itself in these continuing efforts by investigating procedures to facilitate detection in a maritime context. Sea surfaces are often referred to as *rough* surfaces owing to the asperities originating from the water currents that have a tendency make more complex the scattering of an incident radar wave. A witty definition of a rough surface reads as follows (Beckmann and Spizzichino, 1987): "*a surface which will scatter the energy of an incident wave into various directions, whereas a surface that reflects specularly will be called smooth*". To be more specific, the amplitudes scattered from a rough surface often exhibit undesired backscattered returns when illuminated by an incident radar wave. These sea clutters do not convey any information[1] and passively interfere with the legitimate radar target. As they can have large magnitude, their study is not only of theoretical but also of practical importance since otherwise

[1]in contrast, for synthetic aperture radar (SAR) applications, sea clutter is desirable since they provide valuable information on the large scale features of the ocean

the detection of small targets (aircrafts flying at low altitude, Somali skiffs, submarine periscopes) would not be possible. Their characteristics are determined by the interaction between the sea level and the wind as well as by the radar parameters (e.g., wavelength, polarization, grazing angle). Radar experimentalists have observed that sea clutters are more important as the grazing angle decreases and as the radar resolution range becomes higher. On the other hand, Maxwell's equations governing the scattering of an incident wave at high (Hughes, 1978; Holliday et al., 1987) or medium (e.g. Wright, 1968) grazing angles may be solved analytically whereas only empirical models exist for low grazing angle (Horst et al., 1978). Since modern radars are operating with higher resolution, sea clutter modeling has attracted much attention for the radar specialist to face these experimental limitations. In particular, the stochastic[2] nature of the radar returns was shown to be greatly helpful.

1.2 Existing techniques

Owing to the complexity of the interaction between the incident wave and the rough surface, it is easier to provide a statistical description of the scattering process as opposed to one based on solutions of Maxwell's equations with boundary conditions (Blackledge, 2009). Earlier strategies following a Gaussian approach, a school of thought initiated by the classical work of Rice (1951), yielding Rayleigh distributed amplitudes were shown to face limitations as the radar resolution increased at low grazing angles. To account for the numerous high amplitude samples Rayleigh statistics failed to capture, a variety of distributions with heavier tails were proposed, the log-normal distribution (Trunk and George, 1970), the Weibull distribution (Fay et al., 1977) and the K–distribution (Jakeman and Pusey, 1976). The latter gained prominence, in particular because it postulates that the received amplitude may be written as a Gaussian speckle modulated by a root-Gamma texture. The texture is particulary interesting since it varies more slowly than the speckle. A target may thus be detected through by a sudden change in the radar cross-section (RCS) time-series. This multiplicative representation coincides with experimental observations

[2]from the Greek $\alpha\rho\rho o\omega$ arrow

(Ward, 1981) that the received amplitude has two different components, varying over timescales of different order. The compound K–distribution, or compound Gaussian-model, was further extended to cover additional situations: coherent signal in K–distributed clutter (Jakeman, 1980), presence of a white noise (Watts, 1985, 1981) or discrete spikes (Middleton, 1983, 1999). Other sea clutter statistical models oriented for SAR applications may be found in Bucciarelli et al. (1996) which postulates Weibull speckle or in Anastassopoulos et al. (1999) which provides a parametric generalization of the existing literature. Also to be introduced are the concepts of strong and weak scattering. In the former situation, the dynamics and the asymptotic distributions of the backscattered signal are invariant to multiplication by $\exp(i\Lambda)$ for constant Λ. In the latter case, the strongly scattered amplitude lies in superposition with a coherent offset, and the resultant scattered amplitude has a preferred phase. Also, these statistical models enable the derivation of realistic simulation schemes (see Tough and Ward, 1999). Thus, easier and cheaper simulations enable one to reduce the costs of live testing of radar performance (cf. discussion in Ward et al., 2006, Chap. 11).

The radar signal consists of a collection of samples that will be characterized by an anomalous sample of higher amplitude in the presence of a target. Radar engineers therefore set up a threshold to separate clutter plus target from clutter only samples. The magnitude of this threshold is obtained from a trade-off between the probability of detection and the probability of false alarms. Given a measurement of the scattered intensity z , it is assigned either to the distribution $\mathbb{P}_{\mathbf{z}_\mathrm{A}}(z)$ that models the set of values $\mathbf{z}_\mathrm{A}$ corresponding to the clutter (for example, a Rayleigh distribution) or to the distribution $\mathbb{P}_{\mathbf{z}_\mathrm{B}}(z)$ for signal plus clutter (e.g., Rice distribution). Thereafter, the detection and false alarm densities are defined as (Skolnik, 1980)

$$\mathbb{P}_\mathrm{D} = \int_{\mathbf{z}_\mathrm{A}} \mathbb{P}_{\mathbf{z}_\mathrm{A}}(z)dz \tag{1.1}$$

$$\mathbb{P}_\mathrm{FA} = \int_{\mathbf{z}_\mathrm{B}} \mathbb{P}_{\mathbf{z}_\mathrm{B}}(z)dz. \tag{1.2}$$

Building on the statistical models for the sea clutter and for the target(cf. Swerling, 1960, 1997, for a description of target models), these probabilities may be evaluated, at least numerically. Thereafter, a given sample z is ascribed clutter only or clutter plus signal. Under the Neyman–Pearson criterion (Pearson, 1966), the optimal decision rule is to compare the likelihood ratio with a threshold

$$\Lambda(z) = \frac{\mathbb{P}_{\mathbf{z}_\mathrm{A}}(z)}{\mathbb{P}_{\mathbf{z}_\mathrm{B}}(z)} > \lambda, \tag{1.3}$$

which may be generalized if the distributions parameters are not known (cf. Ward et al., 2006, Chap. 6, for a more detailed exposition and illustration examples) . In particular, it is possible to derive sub-optimal but tractable estimators for the K–distribution parameters. A salient feature of the compound representation of the scattered amplitude in terms of a speckle and a texture with different correlation properties is the possibility to de-correlate the speckle by frequency agility whilst the texture remains unchanged. For a given radar system[3], the compound K–representation therefore enables one to compute the probabilities of detection and false alarms, hence the specifications of a radar. A common configuration for radars is the constant false alarm rate (CFAR) requirement for which a variety of techniques optimize the detection for various experimental situations (Ward et al., 2006, Chap. 9) by averaging the received signal over adjacent spatial cells. In particular, CFAR techniques may adjust the detection threshold to manage a changing clutter.

With coherent radars which can measure both the amplitude and the phase of the received signal, the radar signal can be represented as a vector in the complex plane. Researchers have suggested different models for the resulting power spectrum (Doppler). They may take the return spectrum as the summation of Gaussian (Walker, 2000) or Lorentzian/Voigtian terms (Lee et al., 1998). A more recent contribution suggested a stochastic description that encompasses these two cases (Lacaze, 2006). These models are empirical, in contrast to the spectral properties of a K–amplitude derived from first principles in Field and Tough (2003b). Nonetheless, they are useful to understand underlying physics (in particular, about the differences observed between polarization). These models help to detect moving targets from their shifts from the sea clutter spectrum.

[3]there exist empirical models to express the parameter of the K–distribution in terms of the radar configuration (for instance, the so-called GIT model (Horst et al., 1978)).

A long-term work by Haykin *et* coworkers (e.g. Haykin and Puthusserypady, 1997) has attracted considerable interest for a few years. Burning the boats with the well-accepted statistical description of sea clutter, it aimed to classify them as chaotic (as opposed to stochastic) processes. If this were to be the case, the complexity of sea clutters dynamics could be down-sized to a system of non-linear (but deterministic) equations. Although later work has questioned the techniques used to assert the chaotic nature of clutters (Unsworth et al., 2002), this work had the merit to devote itself to the study of the sea clutter *dynamics* rather than to its statistical characteristics.

1.3 Observability of the cross-section

Except for Haykin's work, the statistical nature of the sea clutter has not been cast in any doubt. The stance adopted in this thesis is broader since we shall consider a *dynamical* description of the sea clutter, that yields the *statistical* description in its asymptotic limit, in sense of large number of samples. That is, we consider the temporal evolution of an amplitude scattered from a rough medium rather than its ensemble averaged quantities. Statistical and dynamical representations are closely connected and do share common physical justifications. This methodology, building on a series of papers (Field and Tough, 2003b; Field, 2005; Field and Tough, 2005) summarized in Chapter 3, represents a shift of viewpoint in the design of target detection strategies. We aim to derive procedures to extract the RCS, in local time, from the scattered amplitude time-series alone. As we shall see in detail, our results stem from first principles based on the mathematical structure of the received amplitude and are closely connected to its geometrical structure.

A major element of our approach is to describe the scattered amplitude in an Ito stochastic framework. It bears a close resemblance with the anterior work of Tough (1987) and his Fokker–Planck description. Ito calculus, developed in the 1940s by Kiyoshi Ito[4], is a generalization of standard calculus that enables the differentiation of certain random processes (Karatzas and Shreve, 1988; Øksendal, 1988, or the brief exposition in Appendix B). In Ito calculus, the analog of an ordinary differential equation (ODE) is the stochastic differential equation (SDE) which incorporates an additional term driven by a Brownian motion in addition to the usual differentiable term. One of the salient features of a Brownian motion is to have positive quadratic variation (cf. Appendix B). Brownian motion is a simple instance of a continuous valued continuous time stochastic process. It is named after a nineteenth century Scottish botanist, Robert Brown, who observed that pollen grains suspended in water obeyed a quivering motion (an experiment he repeated for dust particles). A theoretical explanation for this phenomenon was only given nearly a century later by Einstein (1905).

Jakeman's random walk model with step number fluctuations (Jakeman, 1980) decomposes the received scattered amplitude in terms of the summation of individual scatterers' contributions. Their population is taken to be driven by a birth-death-immigration (BDI) population scheme to recover the Gamma distribution of the texture. The BDI process (Bartlett, 1966) posits a linear dependence of the population changes on its current value. We prove that a BDI process with additional quadratic terms paves the way towards a class of diffusion processes, the Pearson class[5], which is important for our discussion since four different texture models considered in the literature (Delignon and Pieczynski, 2002; Balleri et al., 2007) may be obtained as particular instances of this class. These results establish the scope of the observability techniques presented in the thesis.

In the strong scattering case, an earlier contribution from Field (2005) demonstrated how the RCS was observable through the (smoothing over a sample window of the) intensity-weighted instantaneous (squared) fluctuations of the phase. However, the closeness (in terms of the correlation coefficient) between the hidden population (exact cross-section) and the population obtained through the highly volatile phase de-coherence (inferred cross-section) was heavily influenced by the smoothing process,

[4]an earlier and ground-breaking contribution of Wolfrang Döblin was acknowledged only after Ito's work (Yor and Bru, 2002)

[5]thoroughly studied in Wong (1963)

i.e., over how many pulses the phase de-coherence was averaged. In our stochastic framework, we derive an expression for the error between the hidden and the estimated cross-sections. Moreover, we provide analytical formulae for the optimal window length (a value to be used for experimental situations) and for the corresponding error. We also demonstrate that these findings can readily be extended to encompass the broader range of Pearson diffusions. Then, we address an experimental caveat, the presence of an additional measurement noise (Watts, 1985). In this case, the local power incorporates an additional thermal noise term - a situation for which we give a dynamical representation suitable to our Ito framework. To overcome this experimental obstacle, a method to retrieve the original sea clutter is proposed. From the spectral dynamics of the K–scattered amplitude (derived from first principles in Field and Tough, 2003b), we derive the Wiener filter which permits to recover optimally, in the sense of the minimum mean square error (MMSE) criterion, the pure K-distributed amplitude from the surrounding noisy environment. This enables the inference of the RCS by the same token as in the absence of measurement noise.

Next, we direct our attention towards weak scattering, when the scatterers' phases are no longer isotropic. An important feature of a strongly scattered amplitude is the independence between its angular and radial fluctuations. For a weakly scattered amplitude however, the presence of an additional offset spoils this useful geometrical property. Nevertheless, the structure of the angular-radial cross-volatility conveys information about the hidden cross-section if we introduce an orthogonal dyad w.r.t. which resultant amplitude fluctuations de-correlate. Exploring the angle of rotation of this dyad from that aligned to the instantaneous radial direction, enables us to demonstrate how the scattering cross-section may be inferred through the (intensity-weighted) fluctuations of the phase, minus a correcting term accounting for the angular-radial cross-volatility. We thus establish that the earlier result reported in Field (2005) for the K-scattered amplitude (where the correction term vanishes by virtue of the independence between the angular and radial fluctuations) is a particular instance of a broader situation. We also derive a companion formula giving the cross-section in terms of the intensity fluctuations (weighted by the reciprocal intensity). These two techniques enable the inference of the RCS from the time-series of a weakly scattered amplitude - thus facilitating anomaly detection. Since state estimates are obtained in local time, this approach is computationally lighter than the usual statistical approach which requires large batches of data. Finally, we discuss how this inference might be optimized by the same token as for the strong scattering case and we discuss the relationship between the strong and weak scattering situations.

Besides its mathematical elegance, the dynamical description of the scattered amplitude possesses numerous advantages. For instance, the auto-correlation function (ACF) of the received amplitude may be derived analytically by finding the propagators (Wong, 1963) of the SDEs pertaining to the texture and to the speckle(Field and Tough, 2003b). These formulae may then be used to retrieve the pure K-distributed amplitude in the presence of an additional noise. Also, our techniques to infer the RCS, for strong and weak scattering, provide an estimate for the RCS in local time without using ensemble averages most characteristic of a statistical approach[6]. Thus, anomalies in the radar signal may be detected in real-time. Moreover, the proposed techniques are not restricted to a single experimental situation. Whereas in a statistical framework the detection procedures depend, for example, on the texture distribution, our techniques are valid for an arbitrary texture for a weakly or strongly scattered amplitude. Next, they make essential use of coherent data since the inference process exploits the geometrical properties of the received amplitude represented in the complex plane.

The techniques presented in this work are not restricted to anomaly detection, even if they were developed for radar applications. Their range covers that of waves scattering from random media in general. A closely related field is SAR applications, when one aims to detect the large-scale correlated structures of the sea/ocean. Since the compound-Gaussian model of the sea clutter has been validated in this context (Blacknell and Tough, 1995), our techniques may also be pertinent. More generally, they also cover scattering of acoustic waves with applications to sonar (Jahangir and Oliver, 1997). Finally, as discussed upon in the conclusion, our findings may also be useful for nuclear magnetic resonance (NMR) applications as the underlying physics bears mathematical resemblance to that of scattering from a rough medium (cf. Field, 2006, for an account on the analogies between NMR and sea clutter).

[6]computing higher-order moments requires a large number of samples

1.4 Organization of the thesis

The thesis is organized as follows. In Chapter 2, we discuss how an incident radar wave is scattered from a rough marine surface, since the detection of a target over the sea surface is the primary application of our work. This purely physical description is translated into radar terminology and quantities such as the speckle and the texture components are defined. Next, starting with a random walk model with step number fluctuations, we recall from Jakeman (1980) the K–distribution, a statistical model that suits actual experimental radar returns. In particular, we discuss how a BDI process for the step number fluctuations yields the Gamma distributed texture characteristic of the K–distribution. Furthermore, we show how several other texture models studied in the literature may be obtained as the asymptotic densities of the Pearson class of diffusion process. We then relate this class of diffusion with the BDI process by showing that the former is an extension of the latter when quadratic terms in the population changes are incorporated. As an alternative to this statistical description, we describe in Chapter 3 a stochastic model (*orig.* Field and Tough, 2003b) on which the present thesis elaborates. In this Ito framework, the random walk with step number fluctuations yields a compound representation of the scattered amplitude as a Rayleigh speckle modulated by the (square-root of the) RCS. Equipped with Ito's formula, we derive a SDE for the latter and also show how the BDI process yields a SDE for the RCS when the number of scatterers gets large. Consequently, the temporal evolution of the scattering process may be fully described by a set of coupled SDEs accounting for the scattered amplitude, intensity and phase. At this point, we introduce a distinction between strong scattering, where the random walk's phasors are uniformly distributed in phase, and weak scattering, where the random walk is biased. For the former, considering the propagators of the texture and speckle SDEs enables the derivation of the ACF and spectral properties. The weak scattering case is alternatively described as a coherent signal lying in superposition with a strongly scattered amplitude. We conclude this Chapter by a presentation of the Euler–Mayamura simulation scheme that shall be used thoroughly to illustrate our claims (Tough, 1987). Building on this anterior stochastic model, we then present the main contributions of the present work concerning the inference of a RCS for a coherent scattered amplitude. Chapter 4 deals with the strong scattering case for which an earlier contribution (Field, 2005) has shown how the RCS was observable through the intensity-weighted phase fluctuations. To enable this inference process in more practical terms, we derive analytical formulae for the smoothing error and a condition to optimize it. We then discuss how these results are not restricted to a K–distributed amplitude and extend to an arbitrary RCS, as illustrated upon with three other instances of statistical models established in the radar literature that relate to the Pearson class we have introduced earlier. Furthermore, we show how an experimental caveat, the presence of an additive white noise, may be addressed by using the spectral properties of the scattered amplitude. They enable the design of a Wiener filter from which the pure K–scattered amplitude may be estimated. After this filtering step, we show how the RCS may be inferred. In Chapter 5, we focus our attention on the weak scattering case, whose dynamics are more cumbersome owing to the presence of a coherent offset. By decomposing the weakly scattered amplitude fluctuations into terms originating from the speckle and the texture, we show how their geometrical features have useful practical consequences. Incidently, we derive analytical expressions for the drift and volatility tensors of a weakly scattered amplitude for an arbitrary coherent offset. Based on the scattered amplitude fluctuations' geometry, we provide two distinct techniques the inference of the RCS that are closely related to the analogous result described earlier for strong scattering.

Nearly all the results given in this thesis first appeared in various peer-reviewed papers co-authored with the author's supervisor, Dr. Field. These publications are mapped with the thesis contents as follows. Section 2.3, where we discuss diffusion models for the RCS derived on the basis of discrete population models roughly corresponds to Fayard and Field (2010c). Chapter 4 discusses how the RCS can be optimally inferred from the intensity-weighted phase fluctuations of a strongly scattered amplitude. The main results were first published in Fayard and Field (2008) as well as in a consecutive conference publication (Fayard and Field, 2009). An extension of these results for a more general RCS (Fayard and Field, 2010a) is recalled in Sections 4.1.4,4.1.5 and 4.2.6. To overcome an experimental challenge, namely the presence of an additional white noise, we discuss in 4.3 how this undesired component can be optimally filtered out, thus enabling again the inference of the RCS (*orig.* Fayard and Field, 2010b). Our most recent contribution (Fayard and Field, 2011) demonstrated that similar inference/optimization techniques can also be used for a weakly scattered amplitude, as exposed in Chapter 5.

Throughout we shall consistently adopt the notation for a continuous time stochastic process q_t, with Ito differential $\mathrm{d}q_t$ and diffusion coefficients $\mathrm{d}q_t\mathrm{d}p_t = \Sigma_t^{(q,p)}\mathrm{d}t$ and abbreviate via $\mathrm{d}q_t^2 = \Sigma_t^{(q)}\mathrm{d}t$.

Chapter 2

Scattering from random media

2.1 Scattering from a rough surface

2.1.1 Physical description

Scattering of waves from a rough surface is a proliferous field for research due to the broadness of the possible applications. The tremendous complexity of the underlying physics phenomena (e.g., the various layers of waves' motion of the sea surface) prohibits a complete analytical description of the scattered wave (that would in any case be too complex for further handling). Cohorts of researchers (see Rice, 1951; Beckmann and Spizzichino, 1987; Valenzuela, 1978; Alpers and Hennings, 1984, for historical references) have therefore attempted to propose some simplifying empirical models. In particular, the physics pertaining to the scattering of the incident wave on a rough sea surface may reasonably be described at medium or high grazing angle. Unfortunately, the hypotheses enabling a simplified solution do not hold at low grazing angle and/or for high resolution radar, urging the introduction of more elaborated scattering models.

Consequently, an experimental description of the sea surface returns is prompted. The sea-surface does not appear to be purely chaotic but possesses some significant structures that are maintained over time. For instance, small ripples are generated as the wind is blowing, ripples that grow before transferring their energy to longer waves. This latter wave will reach a maximum height after which it breaks out. Consequently, the average power received from a particular radar cell will fluctuate along the complex structure of these waves. Accordingly, the RCS is defined by the area reflectivity and fluctuates extensively around its mean value. It is characterized by temporal and spatial correlation.

An additional challenge arises from the impact of the incident wave's polarization on the response of the sea surface. The plane of polarization is defined by the vector **E**, i.e., either horizontal (H) or vertical polarization (V). Consequently, the transmitted and received polarized waves are described by a pair of symbols: HH,VV,HV,VH (Skolnik, 1980) [1]. Any candidate model for the radar returns needs to be sufficiently flexible to account for these various polarizations.

Radar returns will also be influenced by the roughness of the sea (speed of the wind, height of the waves). A measure for the latter is the sea-sate such as standardized by maritime organizations (cf. Long, 1983, Tab. 2.1). An alternative parameter is the ratio of the variance of the RCS to its squared mean.

Experimentalists have established three different origins of scattering phenomena (Lamont-Smith et al.)

- Scattering from small ripples riding on top of longer ocean waves. This yields polarization dependent scattering described by the composite model (Valenzuela, 1978). The scattering is stronger (respectively, weaker) when the the long wave is tilting the patch towards (respectively, away from) the radar.

- Scattering from the very rough whitecaps of broken waves. This component does not change with the polarization and is localized around the *white-cap* of the wave. The RCS mean value is noted to be much higher than that of the corresponding resonant scattering.

- Specular scattering from the crest of the wave, just before it spills. It causes a burst of scattering of much shorter timescale (of order up to 200 ms). The

[1] for instance, HH for a horizontally transmitted, horizontally received signal

mean value of the RCS depends heavily on the polarization, HH being much higher than VV.

The radar resolution impacts the received signal by determining which features of the sea surface are resolved. The structure of the sea surface is characterized by many length scales, ranging from 1 cm or less (foams, ripples) to tens of meters (swell structure). (cf. discussion of scattering phenomena). If the range of the radar is of several order the characteristic length of the greater substructure, its frequency spectrum will have two distinct frequency components: from the order of tens of milliseconds to the order of many seconds, if not minutes (Ward et al., 2006, pp. 106–107). For a low resolution radar, only scattering phenomena with a long timescale are captured, for which the resulting amplitude obeys Gaussian statistics. A supplementary feature of the sea clutter emerges as the resolution range increases. When the RCS resolution is resolved two sources of fluctuations for the scattered amplitude emerge. Many small structures (often called scatterers) will contribute to the texture, whose magnitude is the envelope of the received signal. At a longer range scale, the structure of the long waves will alter the mean power of the scattered amplitude.

2.1.2 Gaussian statistics

Confronted to the tremendous difficulty of the scattering phenomena involved in the scattering of the incident radar wave on a rough sea surface, radar engineers have adopted for several decades the strategy of giving a statistical description of the scattered amplitude. Such a method is not as precise as would be an analytical solution based on Maxwell's equation but provides a picture of the scattered signal sufficiently detailed for practical purposes. In this vein, the speckle mentioned in Section 2.1.1 is conveniently described by the following random walk

$$\varrho_t^{(N)} = \sum_{j=1}^{N} a_j \exp[i\varphi_t^{(j)}] \tag{2.1}$$

where the form factors $\{a_j\}$ are a collection of i.i.d. random variables and where the phases' shifts $\{\varphi_t^{(j)}\}$ are uniformly distributed in the interval $[0, 2\pi)$. The representation (2.1) holds for both horizontal and vertical scattered wave polarizations and $\varrho_t^{(N)}$ depicts the relevant (complex) component. N denotes the number of scatterers . Fig. 2.1 illustrates the geometry of the scattered amplitude. The resulting scattered amplitude, displayed in red, is the summation of $N = 10$ scatterers' contribution (dotted blue line). Each one of the individual phasors is characterized by a phase (for instance, $\varphi_t^{(1)} = 185°$) and therefore takes value in a circle of radius a_j. The first moment of the $\varrho_t^{(N)}$ is zero whereas its the second moment obeys

$$\mathbb{E}\left[\varrho_t^{(N)}\varrho_t^{(N)*}\right] = \langle a^2\rangle N. \tag{2.2}$$

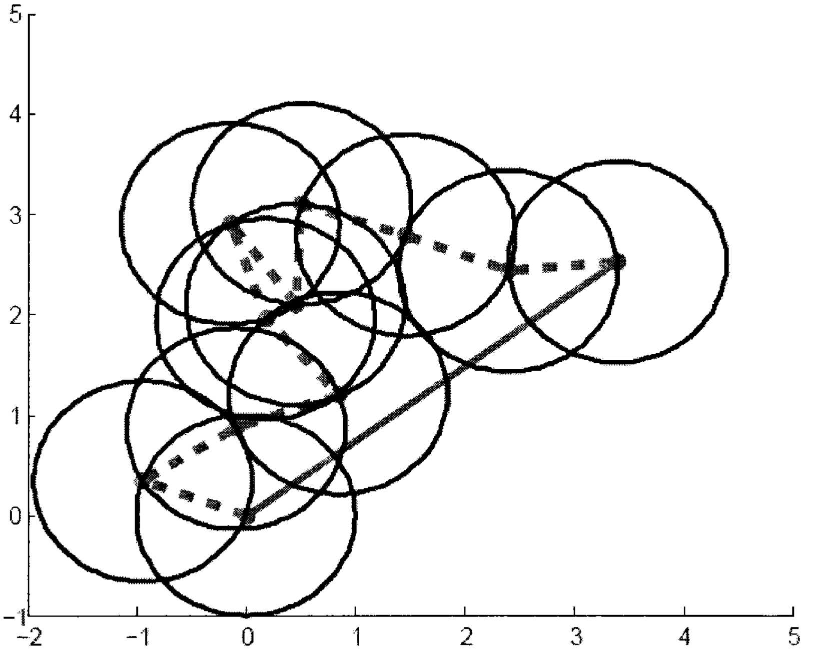

FIGURE 2.1: Geometry of the random walk

Over a low resolution range (that does not resolve the longer waves structure), the radar return consists of the (independent) contributions of a large number of scatterers, that is of the numerous small structures from which the incident signal is backscattered, the total received amplitude being written as the summation of these individual contributions. The random walk model is supported by experimental scattering patterns whereas it cannot be justified solely on the scattering physics (cf. discussion in Jakeman and Pusey, 1976).

To pursue a statistical description of the resulting scattered amplitude, let us introduce the characteristic functions $C_N(\mathbf{u})$

$$C_N(\mathbf{u}) = \langle \exp\left[i\mathbf{u}\varrho\right]\rangle. \tag{2.3}$$

Owing to the independence between the individual scatterers' contributions, the characteristic function can be expressed in terms of a zeroth-order Bessel function (see definition in (C.20) or in Jeffreys and Jeffreys (1956))

$$\begin{aligned} C_N(\mathbf{u}) &= \langle \exp\left[i\mathbf{u}a_j\right]\rangle^N \quad (2.4)\\ &= \langle J_0(\mathbf{u}a_j)\rangle^N. \quad (2.5)\end{aligned}$$

As described in Jakeman (1980), the asymptotic distribution for the case of a large number of scatterers is obtained by normalizing the step magnitude by a factor $\sqrt{N}$ in (2.3). Correspondingly, the scattered amplitude $\varrho_t^{(N)}/\sqrt{N}$ is determined by the following characteristic function for a large number of scatterers

$$\lim_{N\to\infty} C_N(\mathbf{u}) = \exp\left[-\frac{1}{4}\mathbf{u}^2\langle a^2\rangle\right] \tag{2.6}$$

which corresponds to the Rayleigh distribution

$$\mathbb{P}(E) = \frac{2E}{\langle E^2\rangle}\exp\left[-E^2/\langle E^2\rangle\right]. \tag{2.7}$$

The envelope E (i.e., non-coherent statistics obtained through a linear detector) describes the effect of many small scattering structures for a low range radar that does not resolve the fluctuations of the RCS. Consistently, the scattering pattern can be described by the received intensity (square law detector) $z = E^2$ which obeys an inverse exponential distribution

$$\mathbb{P}[z] = \frac{1}{\langle z \rangle} \exp\left[-z/\langle z \rangle\right]. \tag{2.8}$$

Equations (2.7) and (2.8) show explicitly the Gaussian nature of the radar return for a low resolution range or at medium/high grazing angle. It can be seen as a special case of the central limit theorem (CLT) (Papoulis, 1984) since there is a large number of i.i.d. scatterers' contributions. Although these distributions were the first ones to be used to model scattering data (e.g. Goldstein, 1951), they fail to account for scattering patterns with a high-resolution radar at low grazing angle.

2.1.3 Step number fluctuations

We have demonstrated how a constant (but large) number of steps in the random walk (2.1) yields a resulting Gaussian amplitude. Scattering patterns, particulary those obtained with a high-resolution radar, may deviate from Gaussian statistics, urging a more elaborated model. This situation is conveniently addressed by introducing step-number fluctuations, i.e., by considering temporal fluctuations in the population of scatterers. In the steps of Jakeman (Jakeman and Pusey, 1976; Jakeman, 1980), let us posit a negative binomial distribution for the population of scatterers N whose probability mass function (PMF) reads

$$\mathbb{P}[N] = \begin{pmatrix} N+\alpha \\ N \end{pmatrix} \frac{(\overline{N}/\alpha)^N}{(1+\overline{N}/\alpha)^{N/\alpha}}. \tag{2.9}$$

where $\begin{pmatrix} a \\ b \end{pmatrix} = a!/(b!(a-b)!)$ denotes the binomial coefficient and $\overline{N}$ denotes the average number of steps.

To investigate the statistical distribution of the number of scatterers N, let us consider the characteristic function (2.3) averaged over the fluctuations of N

$$C_{\overline{N}}(\mathbf{u}) = \sum_{N=0}^{\infty} C_N(\mathbf{u}) P_N \tag{2.10}$$

$$= \left[1 + \left(\frac{\overline{N}}{\alpha}\right)\left(1 - \langle J_0(\mathbf{u}a/\sqrt{\overline{N}})\rangle\right)\right]^{-\alpha} \tag{2.11}$$

whose asymptote reads

$$\lim_{\overline{N}\to\infty} C_{\overline{N}}(\mathbf{u}) = \left[1 + \frac{u^2\langle a^2\rangle}{4\alpha}\right]^{-\alpha}. \tag{2.12}$$

As a constant number of scatterers yields the familiar Rayleigh distribution, so does a population distributed along (2.9) result in a K–distributed envelope (cf. C.32)

$$\mathbb{P}[E] = \int_0^{\infty} \frac{(\mathbf{u}E) J_0(\mathbf{u}E) \mathrm{d}\mathbf{u}}{\left[1 + \frac{u^2\langle a^2\rangle}{4\alpha}\right]^{\alpha}} \tag{2.13}$$

$$= \frac{4b^{(\alpha+1)/2} E^{\alpha}}{\Gamma(\alpha)} K_{\alpha-1}(2E\sqrt{b}) \tag{2.14}$$

where $b = \alpha/\langle E^2\rangle$ and where K denotes the modified Bessel function of the second kind, see (C.23) for its definition (Jeffreys and Jeffreys, 1956). *Non tantum* is the K–distribution physically motivated by the random walk model *sed etiam* it was validated by experimental tests over the last three decades (see for instance (Jakeman and Pusey, 1976) or (Conte et al.) for a more recent work). It combines the advantages of having an elegant justification in terms of a random walk model, and of suiting scattering data fairly well. Typically the parameter α falls in the range $0.1 \leq \alpha \leq \infty$ (Ward et al., 2006). Rayleigh scattering is recovered for $\alpha \to \infty$ whereas small values of α account for spiky clutter.

2.1.4 Texture and local power

The probability density of the scattered envelope was obtained through its characteristic function. It might be described in an alternative (but equivalent) fashion by positing that the fluctuations in the number of steps induce variations in the average backscattered power. As a result, $\langle E \rangle$ in (2.7) is related to the random local power, x_t, the RCS.

In this vein, (2.7) depicts the (magnitude of) the amplitude scattered from an object with a fixed RCS and non-Gaussian statistics are addressed by considering fluctuations in the RCS. As discussed earlier, we reckon the mean value of the scattered intensity as

$$\langle E^2 \rangle = x \tag{2.15}$$

whilst describing the resulting envelope distribution through a Bayesian scheme

$$\mathbb{P}[E] = \mathbb{P}[E|x]\mathbb{P}[x] \tag{2.16}$$

where $\mathbb{P}[x]$ is the distribution of the cross-section and $\mathbb{P}[E|x]$ the likelihood (i.e., the Rayleigh amplitude due to a single point).

Accordingly, the K–distributed enveloped (2.14) is decomposed into

$$\mathbb{P}[E] = \int_x \frac{2E}{x} \exp\left[-E^2/x\right] \mathbb{P}[x]. \tag{2.17}$$

As seen from (C.31), by identification with (2.14), we obtain a Gamma distributed RCS

$$\mathbb{P}[x] = \frac{b^\alpha x^{\alpha-1} \exp(-bx)}{\Gamma(\alpha)}. \tag{2.18}$$

2.1.5 Moments

In the Gaussian limit, the normalized moments of the scattered intensity (2.8) satisfy

$$\frac{\langle z^n \rangle}{\langle z \rangle^n} = n!. \tag{2.19}$$

Higher resolution clutters usually display normalised intensity moments greater than (2.19). The statistics of the clutter therefore offer a key to reckon non-Gaussian radar returns. On the contrary, a scattered intensity conforming to the multiplicative representation (2.17) has moments

$$\begin{aligned} \langle z^n \rangle &= \int_0^\infty \mathbb{P}[x] \left[2 \int_0 E^{2n+1} \exp\left(-E^2/x\right) \mathrm{d}E \right] \mathrm{d}x & (2.20) \\ &= n! \int_0^\infty x^n \mathbb{P}[x] \mathrm{d}x. & (2.21) \end{aligned}$$

Since x represents the local power, the normalized moments of the scattered intensity are governed by (see Chap.4 in Ward et al. (2006))

$$\frac{\langle z^n \rangle}{\langle z \rangle^n} = n! \, \frac{\langle x^n \rangle}{\langle x \rangle^n} \tag{2.22}$$

which reduces to

$$\frac{\langle z^n \rangle}{\langle z \rangle^n} = n! \, \frac{\Gamma(n+\alpha)}{\Gamma(\alpha)\alpha^n} \tag{2.23}$$

in the K–distributed case. As evidenced upon by (2.19) and (2.22), a non-Gaussian distribution (like the K–distribution) might be seen as Gaussian distributions where an additional ingredient, the fluctuations of the RCS, modifies the recurrence relationship for the moments.

2.2 Diffusion model for the scattering cross-section

2.2.1 Fokker–Planck description

The negative binomial distribution of the number of steps (2.9) was justified on the basis of a discrete population model (Jakeman and Pusey, 1976; Jakeman, 1980). More precisely, a discrete population model accounting for the fluctuations in the number of scatterers N yields (2.9) from its asymptotic distribution, thus reinforcing the random walk model (2.1). In what follows, we shall discuss further this population model.

For a time-dependent population consisting of N scatterers, let us introduce the probability density

$$\mathcal{P}_N(t) \quad = \quad \mathbb{P}[X_t = N] \tag{2.24}$$

which captures the continuous time evolution of the integer-valued process N. If we restrict the model to first-order transitions, only transitions from the neighboring states $N-1$ and $N+1$ are possible. Accordingly, the probability density is governed by (Bartlett, 1966)

$$\frac{\mathrm{d}\mathcal{P}_N}{\mathrm{d}t} \quad = \quad G_{N-1}\mathcal{P}_{N-1} - (G_N + R_N)\mathcal{P}_N + R_{N+1}\mathcal{P}_{N+1} \tag{2.25}$$

where $G_N(t)$ and $R_N(t)$ denote, respectively, the generation and recombination rates for the state N (as shown in Fig. 2.2).

A Taylor expansion of (2.25) with step size l, via the identity $f(x \pm l) = \exp(\pm\partial/\partial x)f(x)$, yields the alternative expression for the master equation, in terms of the continuous-valued counterpart x_t of the discrete N_t,

$$\begin{aligned}\frac{\partial\mathcal{P}(x,t)}{\partial t} \quad = \quad & \left[\exp\left(-l\frac{\partial}{\partial x}\right) - 1\right](G(x,t)\mathcal{P}(x,t)) \\ & + \left[\exp\left(l\frac{\partial}{\partial x}\right) - 1\right].(R(x,t)\mathcal{P}(x,t)).\end{aligned} \tag{2.26}$$

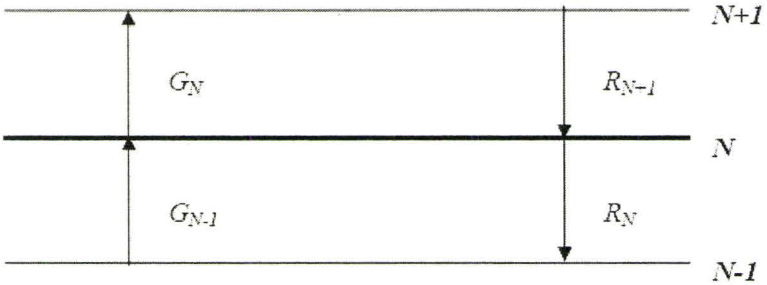

FIGURE 2.2: First-order transition rates

This expression is to be compared with the *Kramers–Moyal* expansion for the evolution of the probability (Kramers, 1940; Moyal and Bartlett, 1949) density

$$\frac{\partial \mathcal{P}}{\partial t} = \sum_{n=1}^{\infty} \left(-\frac{\partial}{\partial x}\right)^n [\mathcal{D}^{(n)}\mathcal{P}], \tag{2.27}$$

where the Kramers–Moyal coefficients, defined as

$$\mathcal{D}^{(n)} = \frac{1}{n!} \lim_{\delta_t \to 0} \left\langle \frac{(X_{t+\delta_t} - X_t)^n}{\delta_t} \right\rangle \tag{2.28}$$

are, by inspection of (2.26), connected to the transition rates as (cf. Risken, 1989; Field and Tough, 2003a)

$$\mathcal{D}^{(n)} = \frac{l^n}{n!}[G(x,t) + (-1)^n R(x,t)]. \tag{2.29}$$

In fact, the order of this expansion does not have much degree of freedom. In effect, Pawula theorem states that Kramers–Moyal expansion (2.27) either truncates for $n = 2$ or is a infinite order (its proof relies on the density's positiveness (Øksendal, 1988)).

For the sake of formalism, let us rewrite (2.27) in terms of normalized population $x_{\mathrm{nor}} = x/\overline{N}$. The Kramers–Moyal expansion of x_{nor} (for a step size $l = 1$) w.r.t.

the re-scaled time parameter $t' = t/\overline{N}$ reads

$$\frac{\partial \mathcal{P}}{\partial t'} = \sum_{n=1}^{\infty} \frac{1}{\overline{N}^{n-1}} \left(-\frac{\partial}{\partial x_{\text{nor}}} \right)^{n} [\mathcal{D}^{(n)} \mathcal{P}]. \tag{2.30}$$

in which, the indices shall be omitted for future references. This Fokker–Planck description captures the temporal properties of the RCS (as opposed to its statistical distribution).

2.2.2 Birth-death-immigration process

The negative binomial distributed number of steps (2.9) and its associated Gamma distributed texture are recovered from (2.25) for a BDI population model. The latter (see Bartlett, 1966, for a thorough discussion) posits that the transition rates $G(N)$ and $R(N)$ are linear w.r.t. the population state N, that is

$$\begin{cases} G(N,t) = \lambda N + \nu \\ R(N,t) = \mu N \end{cases} \tag{2.31}$$

expressed in terms of the birth, death, immigration rates respectively denoted by λ, μ and ν. Alternatively, the population parameters may be understood as follows

$$\mathbb{P}[1 \text{ individual dies during } \delta_t] = \mu \delta_t \tag{2.32}$$

with similar expressions for λ or ν.

A more detailed account of the BDI process is proposed in Appendix A. The BDI process originates from attempts to model the growth of human population, (cf. Bowley, 1924, for a reference of historical interest). Besides its application for radar data analysis described here, it has been applied to a variety of domains: cosmology (Bartlett, 1966), quantum populations (Jakeman, 2005), anthropology (for example Tavaré, 1987), gene mutations (see Novozhilov et al., 2006, for a review of recent applications) etc.

Upon the substitution of the transition rates (2.31) in (2.25), we obtain

$$\frac{\mathrm{d}\mathcal{P}_N}{\mathrm{d}t} = (\lambda(N-1)+\nu)\,\mathcal{P}_{N-1} - ((\lambda+\mu)N+\nu)\,\mathcal{P}_N + (\mu(N+1))\,\mathcal{P}_{N+1}. \quad (2.33)$$

Rather than solving (2.33) for the (infinitely many) $\mathcal{P}_N$, let us introduce the partition function $\Pi_t(z)$ [2], a gadget that incorporates all these solutions,

$$\Pi_t(z) = \langle z^N \rangle = \sum_{N_t=0}^{\infty} z^N \mathcal{P}_N(t). \quad (2.34)$$

By considering the summation of (2.33) weighted by z^N for any N, we can obtain a partial differential equation (PDE) for the partition function. For $\lambda < \mu$, the corresponding steady-state partition function reads (cf. Appendix A)

$$\Pi_\infty(z) = \left(\frac{\mu - \lambda z}{\mu - \lambda}\right)^{-\nu/\lambda}. \quad (2.35)$$

which can be identified with the characteristic function of an inverse binomial distribution (C.3)[3]. Consequently, the PMF of the number of steps postulated in (2.9) is recovered. As a direct consequence of (2.35), the population mean given by $\partial\Pi/\partial z\ _{z=0}$ reads

$$\overline{N} = \frac{\nu}{\mu - \lambda} \quad (2.36)$$

which tends to infinity as λ approaches μ from below while maintaining ν finite.

2.2.3 Continuous limit

The negative binomial distribution for the number of steps (2.9) has just been derived on the basis of a BDI process. The following paragraph explores how the Gamma distributed texture may also be obtained from this population scheme. Let us consider

[2] which is nothing but an abstraction of the partition function in statistical mechanics

[3] indeed, from a comparison of (2.35) and (C.3) we observe that the distribution for the number of steps (2.9) is recovered for $p = 1 - \lambda/\mu$, $\alpha = \nu/\lambda$

the density of the RCS $x = N/\overline{N}$ which conforms to $\mathcal{P}(x,t) = \mathcal{P}_N(t) = \mathcal{P}_{\overline{N}x}(t)$. Taking a Taylor expansion of (2.33) with step $1/\overline{N}$ yields

$$\begin{aligned} \frac{1}{\overline{N}}\frac{\partial \mathcal{P}}{\partial t} &= \mu\left(x+\frac{1}{\overline{N}}\right)\mathcal{P}(x+\frac{1}{\overline{N}},t) - \left[(\lambda+\mu)x+\frac{\nu}{\overline{N}}\right]\mathcal{P}(x,t) \\ &\quad + \left(\lambda x + \frac{\nu-\lambda}{\overline{N}}\right)\mathcal{P}(x-\frac{1}{\overline{N}},t) \qquad (2.37) \\ &= \frac{1}{\overline{N}^2}\left[\overline{N}(\mu-\lambda)\frac{\partial[x\mathcal{P}]}{\partial x} - \nu\frac{\partial \mathcal{P}}{\partial x} + (\mu-\lambda)\left(\frac{1}{2}x\frac{\partial^2\mathcal{P}}{\partial x^2}+\frac{\partial \mathcal{P}}{\partial x}\right)\right]. \qquad (2.38) \end{aligned}$$

With respect to the re-scaled time $t \to t/\overline{N}$, considering the limit $\overline{N} \to \infty$ yields

$$\frac{\partial \mathcal{P}}{\partial t} = \lambda\frac{\partial^2}{\partial x^2}[x\mathcal{P}] + \nu\frac{\partial}{\partial x}[(x-1)\mathcal{P}] \qquad (2.39)$$

that is a Fokker–Planck equation (FPE) for the RCS (i.e., a truncation of the Kramers–Moyal expansion (2.30) for $n = 2$[4]). The asymptotic distribution of the RCS (2.18) is recovered by setting the l.h.s in (2.39) to zero

$$\mathbb{P}[x] = \lim_{t\to\infty}\mathcal{P}(x) = \frac{\alpha^\alpha}{\Gamma(\alpha)}\mathrm{e}^{-\alpha x}x^{\alpha-1} \qquad (2.40)$$

for $\alpha = \nu/\lambda$.

The FPE obtained for a BDI process (2.39) is a simple case of a broader definition

$$\frac{1}{\mathcal{A}}\frac{\partial \mathcal{P}}{\partial t} = -\frac{\partial[b\mathcal{P}]}{\partial x} + \frac{\partial^2[\sigma\mathcal{P}]}{\partial x^2} \qquad (2.41)$$

where b, σ denote, respectively, the drift and volatility parameters and where $\mathcal{A}^{-1}$ is the process characteristic timescale. It appears from (2.41) that any two of the asymptotic distribution $\mathcal{P}_\infty$, b and σ determine the other. More precisely, (cf. Lemma 3.2

[4]which is, by virtue of Pawula theorem, the only finite expansion of the probability density

in Field and Tough, 2003a)

$$\mathcal{P}_\infty = \frac{K}{\sigma}\exp\left(\int^x \frac{b}{\sigma}\right) \tag{2.42}$$

$$b = \sigma\partial_x \log\left(\sigma\mathcal{P}_\infty\right) \tag{2.43}$$

$$\sigma = \frac{k}{\mathcal{P}_\infty} + \frac{\int^x b\mathcal{P}_\infty}{\mathcal{P}_\infty} \tag{2.44}$$

2.2.4 The K–distribution

As discussed earlier, the complexity of the physics phenomena involved in the scattering of an incident wave on a rough surface (maritime radar) described in Section 2.1.1 prevents any analytical description of the scattering process. Nevertheless, Section 2.2 provides some physical insight into the behaviour of the scattered amplitude in terms of the summation of N scatterers' contributions labelled the speckle, with a number of individual scatterers driven by a BDI process (the RCS, which modulates the speckle). The resulting K–distribution is therefore a strongly motivated model for the distribution of the radar returns.

The application of the K–distribution for radar applications was pioneered by Jakeman who demonstrated its significance for scattering experiments (Jakeman and Pusey, 1978). It was also used to describe land-clutter (Jao, 1984.) and SAR images (Joughin et al., 1993). The K–distribution is referred to as a double stochastic distribution since it embodies two degrees of freedom (see for instance Yasuda, 1975, where it was derived from the Gamma distributed stopping time of a Rayleigh random walk in a human population context). It has also been used in a variety of other contexts (e.g., ultrasound imaging Weng et al., 1991).

The K–distribution has been extensively confronted with actual scattered data (as early as Ward, 1981). Among other distributions, especially the Weibull and the log-normal types, it was shown to provide a satisfactory fit to actual radar returns even though the tail of the K–distribution does not fit well large intensity values. In the same multiplicative framework (2.17), various authors have proposed texture models extending beyond the Gamma distribution (Delignon et al., 1997; Gini et al., 2000; Delignon and Pieczynski, 2002; Balleri et al., 2007). The following section discusses how the BDI process could be extended to cover these additional situations.

2.3 Extension to other diffusion models

2.3.1 Class of Pearson diffusions

2.3.1.1 Definition

Let us now consider a class of (continuous-valued) diffusion processes: the Pearson diffusions (Pearson, 1916; Forman and Sørensen, 2008) which are the stationary solutions to a FPE bearing a close resemblance to (2.39)

$$\frac{\partial \mathcal{P}}{\partial t} = \frac{\partial}{\partial x}[\mathcal{A}(x-m)\mathcal{P}] + \frac{\partial^2}{\partial x^2}[\mathcal{A}(ax^2+bx+c)\mathcal{P}] \tag{2.45}$$

An associated SDE reads

$$\mathrm{d}x_t = -\mathcal{A}(x_t-m)\mathrm{d}t + \sqrt{2\mathcal{A}(ax_t^2+bx_t+c)}\mathrm{d}W_t^{(x)}. \tag{2.46}$$

where $\mathcal{A} > 0$ is a time scaling parameter and a, b, c are the process' state parameters. If it exists, the mean of the asymptotic distribution for x_t is given by $\langle x_t \rangle = m$. The domain of x_t is constrained to ensure that the square-root in (2.45) is well-defined. This condition may be fulfilled by setting $c = 0$ (like in Delignon and Pieczynski (2002)), but we shall consider here a broader range of processes. This process is a diffusion (rather than a mere Ito process) since the drift $b_t = m - x_t$ and volatility $\sigma_t^2 = ax_t^2 + bx_t + c$ coefficients are state-dependent (i.e., functions of x_t). Pearson diffusions may alternatively be defined through the following differential equation satisfied by their asymptotic distributions $W(x)$

$$\frac{\mathrm{d}W(x)}{\mathrm{d}x} = -\frac{(2a+1)x-m+b}{ax^2+bx+c}W(x), \tag{2.47}$$

the so-called Pearson system. The first investigation of the equivalence between the probability densities satisfying the Pearson system and the stationary distributions for processes represented by (2.45) was performed by Wong (1963).

2.3.1.2 Importance for scattering applications

From (2.17), the dynamics of the scattered amplitude $\psi = |E|$ are uniquely determined by the dynamics of x. Keeping this in mind, the Pearson class is of interest since it covers a variety of probability distributions used by experimentalists to model the texture of a compound-Gaussian distribution for the scattered amplitude. The Pearson class encompasses heavy-tailed distributions which, by virtue of (2.17), yield a resulting amplitude distribution that is also heavy-tailed. For a volatility coefficient given by $\sigma^2 = kx$, the RCS is asymptotically Γ–distributed with scale parameter k and shape parameter m/k. The resulting scattered envelope will have a K–distribution where the usual parameters b and ν are given, respectively, by $b = 1/k$ and $\nu = m/k$. For maritime radars, the normalized variance $R = \mathrm{Var}[x]/\langle x \rangle^2 = \nu$ is a measure of the sea-state which is high or calm for, respectively, a large or small R. Another Pearson diffusion with parameters $b = (\alpha - x)$ and $\sigma = \beta x^2$ yields a texture that has an inverse Gamma distribution with scale parameter $\beta = a/m$ and shape parameter $\alpha = 1 - 1/a$

$$\mathbb{P}[x] = \lim_{t\to\infty} \mathcal{P}(x) = \frac{\beta^\alpha}{\Gamma(\alpha)} x^{-(\alpha+1)} \mathrm{e}^{-\beta/x} \quad \text{for } x \geq 0. \tag{2.48}$$

which is displayed in Fig. 2.3. Experimental data (Balleri et al., 2007) have assessed the performances of this texture against lake-clutter.

The last two diffusions were used in a slightly different context (synthetic aperture radar interferometry). The first one yields a Beta distribution of the first kind (cf. Fig. 2.4)

$$\mathbb{P}[x] = \frac{\Gamma(p+q)}{\beta^{p+q-1}\Gamma(p)\Gamma(q)} x^{p-1}(\beta - x)^{q-1}, \quad \text{for } 0 \leq x \leq \beta \tag{2.49}$$

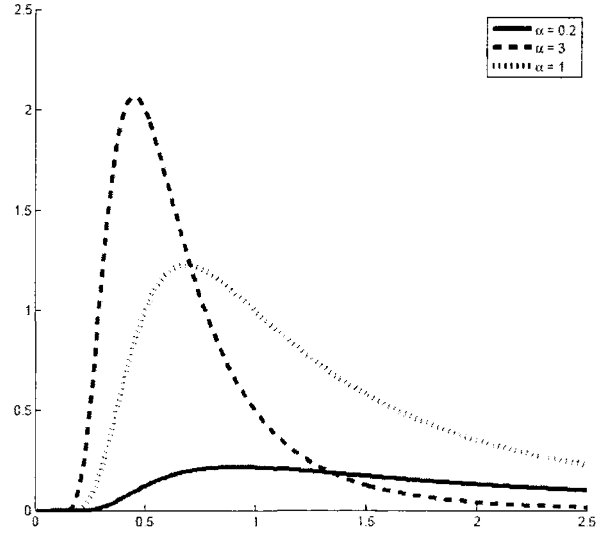

FIGURE 2.3: Inverse Gamma distribution

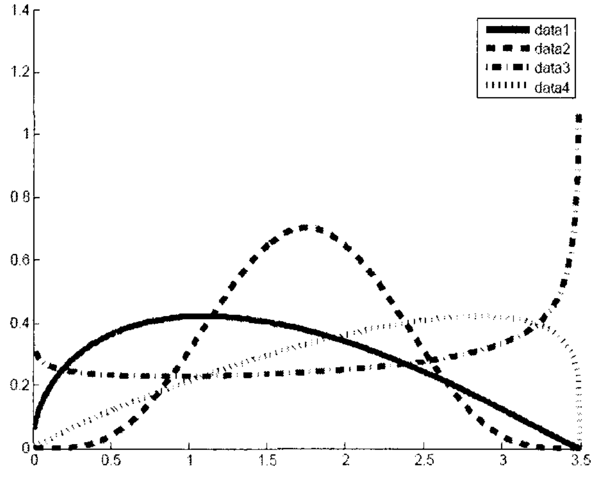

FIGURE 2.4: Beta distribution of the first kind

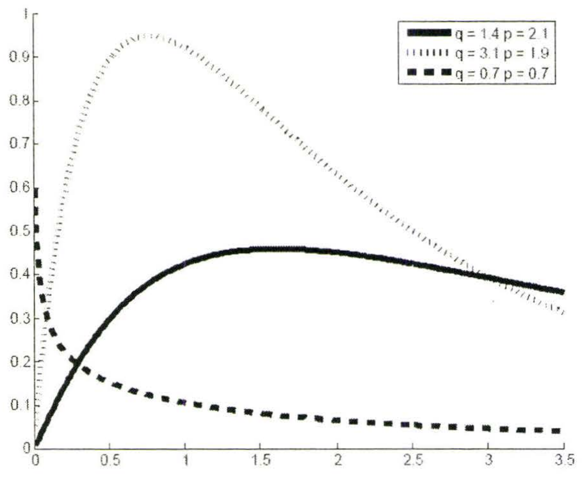

FIGURE 2.5: Beta prime distribution

whose drift and volatility coefficients are given, respectively, by $b = \beta p/(p+q) - x$ and $\sigma = \beta(x - x^2)/(p+q)$. The second one is associated with a Beta prime distribution ($b = \beta p/(q-1) - x$ and $\sigma = (\beta x + x^2)/(q-1)$), shown in Fig. 2.5,

$$\mathbb{P}[x] = \frac{\beta^q \Gamma(p+q)}{\Gamma(p)\Gamma(q)} \frac{x^{p-1}}{(\beta + x)^{p+q}} \quad \text{for } x \geq 0. \tag{2.50}$$

The first two moments of the Beta distribution of the first kind (2.49) are given by $\langle x \rangle = \beta p/(p+q)$ and $\mathrm{Var}[x] = \beta^2 pq(p+q)^{-2}(p+q-1)^{-1}$ whereas these expressions read $\langle x \rangle = \beta p/(q-1)$ and $\mathrm{Var}[x] = \beta^2 p(p+q-1)(q-2)^{-1}(q-1)^{-2}$ for the Beta prime distribution (2.50) (which exist, respectively, for $q > 1$ and $q > 2$).

2.3.2 Associated population model

We have described above the pertinence of the Pearson class for scattering applications. Motivated by the derivation of (2.39) on the basis of a discrete population model in the continuum limit, we attempt to derive the class of the Pearson diffusions on a similar basis of equivalent underlying discrete-valued population models. To this end, let us first extend the BDI process as follows

$$\begin{cases} G = \nu + \lambda N + \bar{\epsilon} N^2 \\ R = \mu N + \bar{\epsilon} N^2 \end{cases} \tag{2.51}$$

where the non-negative parameter $\bar{\epsilon} = \epsilon/\overline{N}$ is of order $\overline{N}^{-1}$ to ensure that the continuous limit of the resulting population is of diffusive type (cf. discussion in Field and Tough (2003a), Section II). Following the same token as for a BDI process, if we substitute the transition rates (2.51) in (2.25) and consider a Taylor expansion, the SDE associated with the resulting FPE reads

$$\mathrm{d}x_t = \nu(1 - x_t)\mathrm{d}t + \sqrt{2(\lambda x_t + \epsilon x_t^2)}\mathrm{d}W_t^{(x)}. \tag{2.52}$$

By virtue of Ito calculus, the transformed cross-section $x \mapsto m\,(x + p)\,/(1 + p)$ is also a Pearson diffusion with *ad hoc* parameters, as captured by the following result for constant p identified below .

Proposition 2.1. *The class of Pearson diffusions, as embodied by (2.45) or (2.46), emerges as the affine transformed version $x \mapsto m\,(x + p)\,/(1 + p)$ of the continuous limit of a discrete-valued population model with transition rates $G = \nu + \lambda N + \bar{\epsilon} N^2$, $R = \mu N + \bar{\epsilon} N^2$ with*

$$\begin{aligned} \nu &= \mathcal{A} \\ \epsilon &= \mathcal{A} a \\ \lambda &= \mathcal{A}\left[b(1+p)/m + 2ap\right] \\ p &= \frac{-(2c + mb) + m\sqrt{b^2 - 4ac}}{2(am^2 + bm + c)} \end{aligned}$$

where μ is a free parameter that determines the asymptotic population mean $\overline{N}$.

2.3.3 Observability of associated population model

We have discussed in Section 2.1.5 how the multiplicative representation of the scattered amplitude enables the expression of its moments in terms of the texture statistics. In the same vein, for Pearson diffusions, a recursive expression for the moments of the RCS proceeds from Ito's formula applied to the process $y_t = x_t^n$ in (2.46)

$$\begin{aligned} \mathrm{d}\left(x_t^n\right) &= -\mathcal{A}nx_t^{n-1}(x_t - m)\mathrm{d}t + \mathcal{A}(ax_t^2 + bx_t + c)n(n-1)x_t^{n-2}\mathrm{d}t \\ &\quad + nx_t^{n-1}\sqrt{2\mathcal{A}(ax_t^2 + bx_t + c)}\,\mathrm{d}W_t^{(x)} \end{aligned} \tag{2.53}$$

Taking the expectation removes the Brownian term and yields the well-known recurrence relation for the moments of a Pearson diffusion (Kenney and Keeping, 1951)

$$\langle x_t^n \rangle = \frac{(m + (n-1)b)\,\langle x_t^{n-1}\rangle + (n-1)c\langle x_t^{n-2}\rangle}{1-(n-1)a}, \tag{2.54}$$

initialized with $\langle x_t^0\rangle = 1, \langle x_t^1\rangle = m$ [5]. On the other hand, we have seen that for a compound-Gaussian clutter the moments of the RCS x_t and of the intensity z_t are related according to (2.22) so a recursive relation also exists for the former. Conversely, if a probability distribution for the scattered intensity does not exhibit such a recurrence relation for the intensity moments (e.g., the Weibull distribution $\langle z^n\rangle = a^n\Gamma(n/\beta+1)$), one cannot postulate a speckle distribution belonging to the Pearson system (although a compound distribution may exist[6]). Combining (2.22) and (2.54) enables the expression of the Pearson diffusion parameters in terms of the

[5] the n^{th} moment exists for $a < 1/(n-1)$ as observed from the asymptotic distribution obtained from these drift and volatility coefficients (2.42).

[6] a compound model of a Rayleigh speckle modulated by a Weibull texture has been considered in Bucciarelli et al. (1996) for clutter that deviate heavily from Gaussian statistics

first four moments of the intensity, if they exist, by

$$a = \frac{\begin{vmatrix} \langle z_t^2\rangle - 2\langle z_t\rangle^2 & 2\langle z_t\rangle & 2 \\ \langle z_t^3\rangle - 3\langle z_t^2\rangle\langle z_t\rangle & 6\langle z_t^2\rangle & 12\langle z_t\rangle \\ \langle z_t^4\rangle - 4\langle z_t^3\rangle\langle z_t\rangle & 12\langle z_t^3\rangle & 36\langle z_t^2\rangle \end{vmatrix}}{\begin{vmatrix} \langle z_t^2\rangle & 2\langle z_t\rangle & 2 \\ 2\langle z_t^3\rangle & 6\langle z_t^2\rangle & 12\langle z_t\rangle \\ 3\langle z_t^4\rangle & 12\langle z_t^3\rangle & 36\langle z_t^2\rangle \end{vmatrix}} \tag{2.55}$$

$$b = \frac{\begin{vmatrix} \langle z_t^2\rangle & \langle z_t^2\rangle - 2\langle z_t\rangle^2 & 2 \\ 2\langle z_t^3\rangle & \langle z_t^3\rangle - 3\langle z_t^2\rangle\langle z_t\rangle & 12\langle z_t\rangle \\ 3\langle z_t^4\rangle & \langle z_t^4\rangle - 4\langle z_t^3\rangle\langle z_t\rangle & 36\langle z_t^2\rangle \end{vmatrix}}{\begin{vmatrix} \langle z_t^2\rangle & 2\langle z_t\rangle & 2 \\ 2\langle z_t^3\rangle & 6\langle z_t^2\rangle & 12\langle z_t\rangle \\ 3\langle z_t^4\rangle & 12\langle z_t^3\rangle & 36\langle z_t^2\rangle \end{vmatrix}} \tag{2.56}$$

$$c = \frac{\begin{vmatrix} \langle z_t^2\rangle & 2\langle z_t\rangle & \langle z_t^2\rangle - 2\langle z_t\rangle^2 \\ 2\langle z_t^3\rangle & 6\langle z_t^2\rangle & \langle z_t^3\rangle - 3\langle z_t^2\rangle\langle z_t\rangle \\ 3\langle z_t^4\rangle & 12\langle z_t^3\rangle & \langle z_t^4\rangle - 4\langle z_t^3\rangle\langle z_t\rangle \end{vmatrix}}{\begin{vmatrix} \langle z_t^2\rangle & 2\langle z_t\rangle & 2 \\ 2\langle z_t^3\rangle & 6\langle z_t^2\rangle & 12\langle z_t\rangle \\ 3\langle z_t^4\rangle & 12\langle z_t^3\rangle & 36\langle z_t^2\rangle \end{vmatrix}} \tag{2.57}$$

In other words, the state parameters a, b, c of (2.45) and (2.47) can be extracted from the intensity moments, which are observable. Since these state parameters also specify the discrete valued underlying population model (via Proposition 2.1), it is possible to express the transition rates of the latter in terms of the intensity raw moments (which are directly observable). A precise knowledge of the underlying population model parameters provides some insight into the underlying physical phenomena. For instance, experimental data show that the scattering pattern depends on the incident wave polarization (e.g., (Farina et al., 1997)). Comparing the population parameters for different polarizations may improve the understanding of this discrepancy.

Besides the state parameters, the knowledge of the characteristic frequency constant $\mathcal{A}$ is also required to fully determine the population model. This quantity may also be extracted from the observed time-series of the intensity (as discussed in Fayard and Field (2008)). As a result, the discrete population model driving the speckle can be entirely inferred from the intensity time series alone (Fayard and Field, 2010c).

Chapter 3

Dynamical stochastic model

3.1 Random walk model and compound presentation

3.1.1 Rayleigh scattering

In Chapter 2, the scattered amplitude/intensity were only considered from a statistical point of view. This description has been successfully applied to actual scattered situations for several decades but fails to capture the instantaneous variations in the scattered signal. This ensemble-average approach may be sublimed by reconsidering the random walk model (2.1) in a stochastic calculus framework. Appendix B proposes an overview of this Ito framework (see also Karatzas and Shreve, 1988; Øksendal, 1988). This SDE description shares the same principles than the FPE description anteriorly proposed in Tough (1987).

Let us recall the random walk model (2.1)

$$\varrho_t^{(N)} = \sum_{j=1}^{N} a_j \exp[i\varphi_t^{(j)}]. \tag{3.1}$$

Rather than considering the characteristic function of $\varrho_t^{(N)}$ which is a statistical tool, if we apply Ito's formula to (3.1) it is possible to derive the scattered amplitude dynamics. The random walk (3.1) does contain a dynamical seed but was only characterized in Section 2.1.2 by a statistical tool, the characteristic function $C_N(\mathbf{u})$ which is an ensemble average quantity. On the contrary, Ito calculus makes use of a process differential, thus describing the time-evolution of the process during an infinitesimal time-interval. The superiority of this dynamical description over the more traditional statistical description shall be obvious while cruising through this thesis' results. Besides its natural applications on electromagnetic scattering, the aforementioned model has shown adequacy for the modelling of wireless network (Feng et al., 2007) (more precisely, to predict modifications to the channel spectra) and for NMR applications (Field, 2006; Field and Bain, 2009, where x_t accounts for the spin population).

We have mentioned earlier in Section 2.1.2 that the phases $\{\varphi_t^{(j)}\}$ were taken as uniformly distributed in the interval $[0, 2\pi)$. A corresponding dynamical model is obtained when $\{\varphi_t^{(j)}\}$ are taken as a collection of (displaced) Wiener processes $\{W_t^{(j)}\}$ on a suitable time scale (Field and Tough, 2003b)

$$\varphi_t^{(j)} = \Delta^{(j)} + \mathcal{B}^{1/2} W_t^{(j)} \tag{3.2}$$

with random initializations $\{\Delta^{(j)}\}$, a set of independent random variables uniformly distributed on the interval $[0, 2\pi)$. The Ito differential of the phase satisfies

$$\mathrm{d}\varphi_t^{(j)} = \mathcal{B}^{1/2} \mathrm{d}W_t^{(j)} \tag{3.3}$$

whereas its square reads

$$\mathrm{d}\varphi_t^{(j)^2} = \mathcal{B}\mathrm{d}t \tag{3.4}$$

On the other hand, Ito's formula applied to the random walk model (3.1) yields

$$\mathrm{d}\varrho_t^{(N)} = \sum_{j=1}^{N} \left(i\mathrm{d}\varphi_t^{(j)} - \frac{1}{2}\mathrm{d}\varphi_t^{(j)2} \right) a_j \exp[i\varphi_t^{(j)}] \tag{3.5}$$

which becomes

$$d\varrho_t^{(N)} = \sum_{j=1}^{N} \left(i\mathcal{B}^{1/2} dW_t^{(j)} - \frac{1}{2}\mathcal{B}dt \right) a_j \exp[i\varphi_t^{(j)}] \tag{3.6}$$

once the phase differentials have been substituted. We reckon the first term in (3.6), labeled $d\zeta_t$, as the summation of N independent randomly phased (unscaled) Wiener process (the independence holding if $\{\varphi_t^{(j)}\}$ have negligible correlation[1]), with a variance equal to $(\sum_j a_j^2)\ \mathcal{B}dt$. We can therefore introduce a complex–valued[2] random process $d\xi$ such that $d\zeta = (\sum_j a_j^2)^{1/2}\mathcal{B}^{1/2}d\xi_t$ [3]. Defining the (normalized) Rayleigh amplitude by $\gamma_t = \lim_{N\to\infty}[\varrho_t/N^{1/2}]$ leads to the resultant dynamics (Field and Tough, 2003b)

$$d\gamma_t \;=\; -\frac{1}{2}\mathcal{B}\gamma_t dt + \mathcal{B}^{\frac{1}{2}}\langle a^2\rangle^{\frac{1}{2}} d\xi_t. \tag{3.7}$$

If we re-scale the Rayleigh amplitude according to $\gamma_t \mapsto \langle a^2\rangle^{-\frac{1}{2}}\gamma_t$, then the re-scaled field satisfies (3.7) with the form factors equal to unity. In what follows we shall therefore assume the field to be scaled in this way, i.e., $\langle a^2\rangle = 1$. In light of (2.7) and (3.7), the distinction between *statistical* and *dynamical* descriptions of the scattering process, both originating from a normalized random walk model, is obvious (the former being the asymptotical behaviour of the latter). The speckle γ_t obeys an asymptotic Rayleigh distribution (2.7) whose instantaneous fluctuations are driven by (3.7). It accounts for the Rayleigh nature of the scattered amplitude in the case of the number of steps in (3.1) is fixed. The SDE (3.7) can be solved by considering the stochastic differential $d[\gamma_t \exp(\mathcal{B}t/x)]$

$$\gamma_t \;=\; \exp\left(-\frac{1}{2}\mathcal{B}t\right)\left[\gamma_0 + \mathcal{B}^{\frac{1}{2}}\int_0^t \exp\left(\frac{1}{2}\mathcal{B}s\right) d\xi_s\right], \tag{3.8}$$

[1] a condition fulfilled if $t \geq T$, the relaxation time
[2] that is, $|d\xi_t|^2 = dt$ and $d\xi_t^2 = 0$
[3] cf. the Lévy characterisation of Brownian motion from a collection of continuous martingales (Applebaum, 2004, p. 223).

so that γ_t is a complex Ornstein–Uhlenbeck (COU) process. Consequently, the first two moments of γ_t are given by Field and Tough (2003b)

$$\mathbb{E}[\gamma_t] = \exp(-\frac{1}{2}\mathcal{B}t)\gamma_0 \tag{3.9}$$

$$\mathbb{E}[|\gamma_t|^2] = 1 + \exp(-\mathcal{B}t)(|\gamma_0|^2 - 1) \tag{3.10}$$

and fully determine γ_t as Gaussian variate [4].

3.1.2 Compound representation

The statistics of γ_t are of Gaussian nature, as evidenced by the linear SDE (3.7) [5]. In the same vein than in Section 2.1.3, non-Gaussian statistics might be obtained by introducing a fluctuating number of steps $N \to N_t$ into the random walk model (3.1). In effect, if we define the (continuous-valued) cross-section as $x_t = \lim_{N_t \to \infty}[N_t/\overline{N}]$, the (normalized) resultant amplitude $\psi_t = \lim_{N \to \infty}[\varrho_t^{(N_t)}/\overline{N}^{1/2}]$ has the following compound representation (Field and Tough, 2003b)

$$\begin{aligned} \psi_t &= \lim_{N_t \to \infty}\left[\varrho_t^{(N_t)}/\overline{N}^{1/2})\right] \\ &= \lim_{N_t \to \infty}\left[\left(N_t/\overline{N}\right)^{1/2}(\varrho_t^{(N_t)}/N_t^{1/2})\right] \\ &= x_t^{\frac{1}{2}}\gamma_t \end{aligned} \tag{3.11}$$

with $\gamma_t = \lim_{N \to \infty}[\varrho_t^{(N_t)}/N_t^{\frac{1}{2}}]$, and in which x_t and γ_t are independent processes.

On the other hand, as the speckle has unit power $\mathbb{E}[|\gamma_t|^2] = 1$ (cf. (3.10)) the scattered intensity $z_t = x_t|\gamma_t|^2$ satisfies $\mathbb{E}[z_t] = x_t$ asserting that the texture x_t is nothing but the local power (cf. Equation (2.15)). The dynamics of this RCS are governed by the following SDE corresponding to the FPE (2.41)

$$\mathrm{d}x_t = b_t\mathrm{d}t + (2\mathcal{A}\sigma_t)^{\frac{1}{2}}\,\mathrm{d}W_t^{(x)} \tag{3.12}$$

[4]since the phase distribution is uniform about $\gamma_t = \gamma_0\exp(-\frac{1}{2}\mathcal{B}t)$ (which tends to zero as $t \to \infty$)

[5]this observation is a corollary of Doob's theorem which states the forms of the correlation function, spectral density and probability densities of any random process which is both Gaussian and Markov (Doob, 1942). Since the probability density companion to (3.7) (obtained through (2.42)) conforms to the generic form specified by Doob, the speckle γ_t is Gaussian.

in which the drift b_t and diffusion σ_t parameters are (real-valued) stochastic processes, not necessarily Ito processes, adapted to the filtration $\mathcal{F}_t^{(x)}$ corresponding to the Wiener process $\mathrm{d}W_t^{(x)}$. The Gamma distributed texture, most characteristic of a K-scattered amplitude is recovered for the following SDE

$$\mathrm{d}x_t \;=\; (\alpha - x_t)\mathrm{d}t + (2\mathcal{A}x_t)^{\frac{1}{2}}\,\mathrm{d}W_t^{(x)}, \tag{3.13}$$

which is equivalent to its companion FPE (2.39) for the re-scaled process $x_t \mapsto \alpha x_t$.

3.2 Strong scattering dynamics

3.2.1 Field equation

The compound representation (3.11) coincides with the (experimentally evidenced) multiplicative representation of the sea clutter in terms of a speckle modulated by a texture. In effect, by scrutinizing the time-series of the received scattered signal radar experimentalists have demonstrated that some geometrical structures remain constant over time. More precisely, Ward (1981) has distinguished two components in the radar returns, a geometric pattern kept invariant by frequency agility and a ragged profile for a fixed frequency. Thus, since the compound representation has been experimentally validated, it enables the derivation of the scattered amplitude dynamics from the SDEs for the texture (3.12) and the speckle (3.7). In effect, applying Ito product formula to (3.11) yields

$$\mathrm{d}\psi_t \;=\; x_t^{1/2}\mathrm{d}\gamma_t + \frac{\gamma_t}{2x_t^{1/2}}\mathrm{d}x_t - \frac{\gamma_t}{8x_t^{3/2}}\mathrm{d}x_t^2 \tag{3.14}$$

since x_t and γ_t are independent (hence, $\mathrm{d}\gamma_t\mathrm{d}x_t = 0$). Equipped with the Ito differential x_t and γ_t, the Ito differential of the scattered amplitude, for a *generalized* cross-section (see Section 2.3), reads

$$\begin{aligned}\frac{\mathrm{d}\psi_t}{\psi_t} &= \left[\mathcal{A}\left(\frac{b_t}{2x_t}-\frac{\sigma_t}{4x_t^2}\right)-\frac{1}{2}\mathcal{B}\right]\mathrm{d}t \\ &+\left(\frac{\mathcal{A}\sigma_t}{2x_t^2}\right)^{\frac{1}{2}}\mathrm{d}W_t^{(x)}+\left(\frac{\mathcal{B}^{\frac{1}{2}}}{\gamma_t}\right)\mathrm{d}\xi_t. \end{aligned} \tag{3.15}$$

In the above expression, $\mathcal{A}$ and $\mathcal{B}$ are the reciprocals of the characteristic times for the autocorrelation of the cross-section and the speckle, respectively. (The frequency $\mathcal{A}$ is inherent to the RCS and independent from the incident field whereas $\mathcal{B}$ is proportional to the wavenumber of the illumination radiation $\mathcal{B} \sim c|\mathbf{k}|$.) In the limiting case $\mathcal{A} = 0$, (3.15) reduces to (3.7) and Rayleigh scattering is recovered. Equation (3.15), known as the Field's equation, (*orig.*, Field and Tough, 2003b) is a major result since it captures the instantaneous fluctuations of the scattered amplitude (as opposed to the statistical representation of the scattering envelope $E = |\psi|$ (2.14)).

We note that the squared fluctuations of the scattered amplitude are given by

$$|\mathrm{d}\psi_t|^2 = \left(\frac{\mathcal{A}\sigma_t z_t}{2x_t^2}+\mathcal{B}x_t\right)\mathrm{d}t \tag{3.16}$$

which reduces to

$$|\mathrm{d}\psi_t|^2 = \left(\frac{\mathcal{A}z_t}{2x_t}+\mathcal{B}x_t\right)\mathrm{d}t \tag{3.17}$$

for a K–distributed amplitude. The linearity of the right-hand side in z_t forms the basis of the anomaly detection procedure proposed in Field and Tough (2003a)[6]. In the presence of a target, the correlation between the received intensity of the squared amplitude fluctuations will no longer hold. These claims were illustrated therein from data of K-distributed radar returns from a region of the ocean surface. The correlation between the squared amplitude fluctuations and the intensity were lost in the presence of a target, thus providing a means of anomaly detection.

[6]additionally, the Doppler effect accentuates the correlation between z_t and the squared amplitude fluctuations (Field, 2009, Chap. 11)

3.2.2 Intensity and phase dynamics

From the definition of the scattered intensity $z_t = |\psi_t|^2$, its Ito differential is given by

$$\mathrm{d}z_t \;=\; \psi_t \mathrm{d}\psi_t^* + \psi_t^* \mathrm{d}\psi_t + |\mathrm{d}\psi_t^*|^2, \tag{3.18}$$

that is

$$\begin{aligned}\mathrm{d}z_t \;=\; & \left[\mathcal{A}\left(\frac{b_t z_t}{x_t}\right) + \mathcal{B}(x_t - z_t)\right]\mathrm{d}t \\ & +(2\mathcal{A}\sigma_t)^{\frac{1}{2}}\left(\frac{z_t}{x_t}\right)\mathrm{d}W_t^{(x)} + (2\mathcal{B}x_t z_t)^{\frac{1}{2}}\,\mathrm{d}W_t^{(r)},\end{aligned} \tag{3.19}$$

where the fluctuations of z_t are expressed in terms of the RCS Brownian differential $\mathrm{d}W_t^{(x)}$ and of the radial Brownian differential $\mathrm{d}W_t^{(r)}$

$$(\gamma_t^* \mathrm{d}\xi_t + \gamma_t \mathrm{d}\xi_t^*) \;=\; \left(\frac{2z_t}{x_t}\right)^{\frac{1}{2}}\mathrm{d}W_t^{(r)}. \tag{3.20}$$

We also verify that the squared intensity fluctuations obey

$$\mathrm{d}z_t^2 \;=\; \left(\frac{2\mathcal{A}\sigma_t z_t^2}{x_t^2} + 2\mathcal{B}x_t z_t\right)\mathrm{d}t \tag{3.21}$$

and that, for $\mathcal{A} \ll \mathcal{B}$, the instantaneous scattered intensity and its squared intensity fluctuations are strongly correlated since the first term in (3.21) becomes negligible. The dynamics for the scattering cross-section x_t (3.12) and the (correlated) intensity z_t (3.19) are thus written as a system of coupled SDEs (correlated over their timescale $\mathcal{A}^{-1}$ and $\mathcal{B}^{-1}$, respectively), a model appropriate for scattering from marine surfaces.

To derive the dynamics of the scattering phase, let us express the scattered amplitude in polar form $\psi_t = R_t \exp(i\theta_t)$ and thus, writing $i\theta_t = \log(\psi_t/R_t)$, we deduce from Ito's formula that

$$i\mathrm{d}\theta_t \;=\; \frac{\mathrm{d}\psi_t}{\psi_t} - \frac{1}{2}\left(\frac{\mathrm{d}\psi_t}{\psi_t}\right)^2 - \frac{\mathrm{d}R_t}{R_t} + \frac{1}{2}\left(\frac{\mathrm{d}R_t}{R_t}\right)^2. \tag{3.22}$$

Since the left-hand side is purely imaginary, we can express $\mathrm{d}\theta_t$ in terms of ψ_t alone as

$$\mathrm{d}\theta_t = \frac{1}{2i}\left[\left(\frac{\mathrm{d}\psi_t}{\psi_t} - \frac{1}{2}\left(\frac{\mathrm{d}\psi_t}{\psi_t}\right)^2\right) - \left(\frac{\mathrm{d}\psi_t^*}{\psi_t^*} - \frac{1}{2}\left(\frac{\mathrm{d}\psi_t^*}{\psi_t^*}\right)^2\right)\right], \tag{3.23}$$

or, alternatively, as

$$\mathrm{d}\theta_t = \Im\left[\frac{\mathrm{d}\psi_t}{\psi_t} - \frac{1}{2}\left(\frac{\mathrm{d}\psi_t}{\psi_t}\right)^2\right]. \tag{3.24}$$

Meanwhile, from (3.15)

$$\begin{aligned}\frac{\mathrm{d}\psi_t}{\psi_t} - \frac{1}{2}\left(\frac{\mathrm{d}\psi_t}{\psi_t}\right)^2 &= \left[\mathcal{A}\left(\frac{b_t}{2x_t} - \frac{\sigma_t}{2x_t^2}\right) - \frac{1}{2}\mathcal{B}\right]\mathrm{d}t \\ &\quad + \left(\frac{\mathcal{A}\sigma_t}{2x_t^2}\right)^{\frac{1}{2}}\mathrm{d}W_t^{(x)} + \left(\frac{\mathcal{B}^{\frac{1}{2}}}{\gamma_t}\right)\mathrm{d}\xi_t.\end{aligned} \tag{3.25}$$

Accordingly, the phase is governed by the SDE

$$\mathrm{d}\theta_t = \left(\frac{\mathcal{B}x_t\gamma_t}{2z_t}\right)^{\frac{1}{2}}\mathrm{d}W_t^{(\theta)} \tag{3.26}$$

where the terms involving ξ_t were expressed in terms of a distinct real-valued angular Wiener process

$$\frac{1}{i}(\gamma_t^*\mathrm{d}\xi_t - \gamma_t\mathrm{d}\xi_t^*) = \left(\frac{2z_t}{x_t}\right)^{\frac{1}{2}}\mathrm{d}W_t^{(\theta)}. \tag{3.27}$$

It appears from (3.26) that the phase is a pure volatility process (vanishing drift) which has the important consequence that the cross-section is proportional to the intensity-weighted squared fluctuations of the phase

$$\mathrm{d}\theta_t^2 = \frac{\mathcal{B}x_t}{2z_t}\mathrm{d}t \tag{3.28}$$

whatever the dynamics of x_t. This observation has major consequences since it facilitates the inference of the RCS from the scattered amplitude.

3.2.3 Correlation of fluctuations

We note that the two Wiener processes arising above, $\mathrm{d}W_t^{(r)}$ (3.20) and $\mathrm{d}W_t^{(\theta)}$ (3.27), are independent (the radial and angular fluctuations in the resultant amplitude are statistically independent). This observation, not valid in the weak scattering case described below, is most characteristic of the compound representation in terms of two independent processes. On the other hand, the scattered intensity is correlated with the RCS through (3.11).

We may also investigate the correlation between the scattered amplitude components. Radar signals usually have the I_t,Q_t representation (e.g. Helstrom, 1960) in terms of an in-phase and a quadrature-phase components with $I_t = R_t \cos\theta_t$ and $Q_t = R_t \sin\theta_t$. Owing to the independence between the radial and angular components, we obtain the following geometric relation (Field and Tough, 2003b)

$$\mathrm{d}I_t \mathrm{d}Q_t \quad = \quad \cos\theta_t \sin\theta_t \left(2z_t^{1/2}\mathrm{d}z_t^2 - z_t \mathrm{d}\theta_t^2\right). \tag{3.29}$$

As a result, the I_t and Q_t components of ψ_t are independent if and only if $\Sigma_t^{(z)} = 2z\Sigma_t^{(\theta)}$. This case only occurs for Rayleigh scattering $\mathcal{A} = 0$ for which I_t and Q_t can be described by the imaginary and real parts of the complex Ornstein–Uhlenbeck process (3.7). Radar engineers' assumption that the I_t and Q_t components are independent is therefore only legitimate for certain contexts.

3.3 Weak scattering dynamics

3.3.1 Definition

The strong scattering amplitude was derived for uniformly distributed scatterers' phases. This assumption is no longer satisfied for a *weakly scattered amplitude* where the random walk individual contributions will have a preferred direction - the random walk will be biased (Jakeman and Tough, 1987). Weak scattered distributions are also relevant to describe wireless network communications (e.g., the channel fading of a radio signal has weakly scattered statistics (Ye et al., 2003)). Moreover, multipath diversity in multiple input multiple output (MIMO) systems can be exploited by asserting a biased random walk (Salmi et al., 2009).

The weakly scattered amplitude Ψ_t is conveniently described as the strongly scattered amplitude ψ_t lying in superposition with a coherent offset amplitude e_t

$$\Psi_t = \psi_t + e_t. \tag{3.30}$$

This situation is known as *weak scattering* since the magnitude of the scattering term (i.e., ψ_t) is assumed to be small in comparison with e_t, which can be seen as the signal of interest.

To account for a broader range of experimental situation, we only specify that this latter term is a function of the state x_t. By virtue of Ito's formula, its stochastic differential is given by

$$\mathrm{d}e_t = e'_t \mathrm{d}x_t + \frac{1}{2} e''_t \mathrm{d}x_t^2 \tag{3.31}$$

where $e'(x_t) = \partial e(x_t)/\partial x_t$ and $e''(x_t) = \partial^2 e(x_t)/\partial x_t^2$.

Equation (3.30) essentially encompasses three different models for the scattered amplitude, all of which may be understood by imposing a bias on each step $s^{(j)}$ of the associated random walk model:

$$\varrho_t^{(N)} = \sum_{j=1}^{N} \left(\overbrace{a + \exp[i\varphi_t^{(j)}]}^{s^{(j)}} \right), \tag{3.32}$$

The Rice model is obtained for a time invariant number of scatterers. The constant offset contribution, after an appropriate scaling by the reciprocal mean and root population for the respective terms under the summation, yields a resultant amplitude

$$\Psi_t^R = a + \gamma_t. \tag{3.33}$$

The Rice distribution (cf. Jeffreys and Jeffreys, 1956), which posits a constant RCS ($\mathcal{A} = 0$ in (3.12)), has played a fundamental role in early radar signals (target model, (Minkoff, 2002)).

The Homodyned K–scattering model (HK) originates from a constant offset $e_t = a$ in the random walk that does not fluctuate with N_t, in the case of the number of scatterers fluctuates with time. In the continuum limit, this amounts to adding a constant to the K–amplitude

$$\Psi_t^{HK} = a + \psi_t. \tag{3.34}$$

This model was also proposed to emulate scattering from turbulent media. This model combines the homodyning feature of the Rice distribution with the scatterers' characterization of the K–distributed amplitude. Recent work in medical imaging has been using this distribution (Ditt and Greenleaf, 1994).

The Generalized K–scattering model (GK) occurs when the scattering population has fluctuations and the coherent offset fluctuates in proportion to this population (by virtue of the number of terms summed in (3.32)). Scaling by the reciprocal mean and root mean population yields

$$\Psi_t^{GK} = ax_t + \psi_t \tag{3.35}$$

when $N_t \to \infty$. The main difference with the HK model lies in the fact that the random walk itself is biased. Among other applications, this model was successfully applied to polarimetric and interferometric SAR (Tough et al., 1995; Blacknell and Tough, 1995).

3.3.2 Scattering dynamics

The dynamics of the strongly scattered amplitude (3.15) and the definition of a weakly scattered amplitude (3.30) enable the derivation, separately, of the dynamics pertaining to a Rice, HK or GK amplitude (Field and Tough, 2005). For the sake of generality, it is more instructive to consider the dynamics of the weakly scattered amplitude independently of the coherent offset's details. The Ito differential of Ψ_t is given by

$$\mathrm{d}\Psi_t = \mathrm{d}\psi_t + \mathrm{d}e_t \tag{3.36}$$

that is

$$\mathrm{d}\Psi_t = e_t'\mathrm{d}x_t + \tfrac{1}{2}e_t''\mathrm{d}t + x_t^{1/2}\mathrm{d}\gamma_t + \tfrac{\gamma_t}{2x_t^{1/2}}\mathrm{d}x_t - \tfrac{\gamma_t}{8x_t^{3/2}}\mathrm{d}x_t^2. \tag{3.37}$$

Substituting the dynamics of the speckle (3.7) and cross-section (3.12) yields the following result.

Proposition 3.1. *The dynamics of a weakly scattered amplitude with an arbitrary offset e_t, $\Psi_t = e_t + \psi_t$, are given by*

$$\begin{aligned}\mathrm{d}\Psi_t = &\left(\psi_t\left[\mathcal{A}\left(\frac{b_t}{2x_t} - \frac{\sigma_t}{4x_t^2}\right) - \frac{1}{2}\mathcal{B}\right] + \mathcal{A}e_t'b_t + \mathcal{A}\sigma_t e_t''\right)\mathrm{d}t\\ &\left[\gamma_t\left(\frac{\mathcal{A}\sigma_t}{2x_t}\right)^{\frac{1}{2}} + e_t'\left(2\mathcal{A}\sigma_t\right)\right]\mathrm{d}W_t^{(x)} + \left(\mathcal{B}x_t\right)\mathrm{d}\xi_t.\end{aligned} \tag{3.38}$$

By virtue of the weakly scattered intensity definition, $Z_t = |\Psi_t|^2$, its Ito stochastic differential reads

$$\mathrm{d}Z_t = \Psi_t^*\mathrm{d}\Psi_t + \Psi_t\mathrm{d}\Psi_t^* + |\mathrm{d}\Psi_t|^2. \tag{3.39}$$

From the representation of Ψ_t in polar form, the phase Ito differential satisfies (cf. strong scattering (3.23)

$$\mathrm{d}\Theta_i = \frac{1}{2i}\left[\left(\frac{\mathrm{d}\Psi_t}{\Psi_t} - \frac{1}{2}\left(\frac{\mathrm{d}\Psi_t}{\Psi_t}\right)^2\right) - \left(\frac{\mathrm{d}\Psi_t^*}{\Psi_t^*} - \frac{1}{2}\left(\frac{\mathrm{d}\Psi_t^*}{\Psi_t^*}\right)^2\right)\right] \tag{3.40}$$

and their products

$$\begin{aligned}
\Sigma_t^{(Z)} &= \Psi_t^2 \Sigma_t^{(\Psi^*)} + \Psi_t^{*2} \Sigma_t^{(\Psi)} + 2 Z_t \Sigma_t^{(\Psi,\Psi^*)}, \\
\Sigma_t^{(Z,\Theta)} &= \Im \left[\left(\frac{\Psi_t^*}{\Psi_t} \right) \Sigma_t^{(\Psi)} \right], \\
\Sigma_t^{\Theta} &= \frac{1}{4} \left[\frac{2\Sigma_t^{(\Psi,\Psi^*)}}{Z_t} - \frac{\Sigma_t^{(\Psi)}}{\Psi_t^2} - \frac{\Sigma_t^{(\Psi^*)}}{\Psi_t^{*2}} \right].
\end{aligned} \tag{3.41}$$

3.4 Spectral properties of the K–distributed noise

3.4.1 Autocorrelation function

An important advantage of the dynamical description of the scattered amplitude described above, in contrast to the usual statistical description, is the possibility to derive a generic form for the autocorrelation function (ACF) (and any higher dynamics) since the amplitude temporal evolution is accessible [7]. Echoing the multiplicative representation of the scattered amplitude in terms of two (statistically independent) processes, it is necessary to derive separately the autocorrelation functions of the (square root of the) cross-section and of the speckle- as described in Field and Tough (2003b).

Proposition 3.2. *The ACF of the scattered amplitude, symmetric w.r.t. time, is given by*

$$\langle \psi_t \psi_0^* \rangle = \exp\left(-\mathcal{B}t/2\right) \frac{\Gamma(\alpha + \frac{1}{2})^2}{\Gamma(\alpha)^2} {}_2F_1(-\frac{1}{2}, -\frac{1}{2}, \alpha, \exp(-\mathcal{A}t)) \tag{3.42}$$

for $t > 0$, and where ${}_2F_1$ denotes the hypergeometric function [8].

[7] as pointed out in Field (2009), a remark from Jakeman and Tough (1988) reads "A full analysis of the temporal correlation properties of the variables x and z implicit in (5.24) would require knowledge of its fundamental solution or propagator, which is as yet, unknown..."

[8] cf. useful mathematical formulae in Appendix C

Proof. The propagator (i.e., Green's function for the corresponding FPE (Risken, 1989)) for (3.13) is given by

$$\begin{aligned}\mathbb{P}(x,t|x_0) &= \frac{1}{1-\exp(-\mathcal{A}t)}\left(\frac{x\exp(\mathcal{A}t)}{x_0}\right)^{(\alpha-1)/2} \\ &\qquad \exp\left(-\frac{x+x_0\exp(-\mathcal{A}t)}{1-\exp(-\mathcal{A}t)}\right)\times I_{\alpha-1}\left(\frac{2\exp(-\mathcal{A}t/2)\sqrt{xx_0}}{1-\exp(-\mathcal{A}t)}\right) \quad (3.43)\end{aligned}$$

where I_α denotes the modified Bessel function . This can be re-expressed as a series expansion

$$\mathbb{P}(x,t|x_0) = x^{\alpha-1}\exp(-x)\sum_{n=0}^{\infty}\frac{n!}{\Gamma(n+\alpha)}\exp(-\mathcal{A}nt)L_n^{\alpha-1}(x)L_n^{\alpha-1}(x_0) \quad (3.44)$$

where the Laguerre polynomials L_n^α are defined by

$$L_n^\alpha(x) = \frac{x^{-\alpha}\exp(x)}{n!}\left(\frac{\mathrm{d}}{\mathrm{d}x}\right)^n\left(x^{\alpha+n}\exp(-x)\right) \quad (3.45)$$

(c.f. Wong, 1963) for corresponding derivations.

The SDE (3.15) does not exhibit explicit time dependence, and since there exists an asymptotic distribution (which the initial values are drawn from), the amplitude process ψ_t is stationary. Therefore, we can apply the Wiener–Khintchine theorem which asserts that the power spectral density (PSD) $S(\omega)$ is equal to the Fourier transform (denoted by a tilde) of the ACF, i.e., $\langle\widetilde{\psi}(\omega)\widetilde{\psi}(\omega')\rangle = \pi\delta(\omega-\omega')S(\omega)$ where $S(\omega) = \widetilde{\langle\psi_t\psi_0^*\rangle}$. The amplitude ACF satisfies

$$\langle\psi_t\psi_0^*\rangle = \langle\sqrt{x_tx_0}\rangle\langle\gamma_t\gamma_0^*\rangle = \langle\sqrt{x_tx_0}\rangle\exp\left(-\mathcal{B}|t|/2\right) \quad (3.46)$$

where the evaluation of the factor $\sqrt{x_t x_0}$ proceeds according to the propagator expansion (3.44),

$$\begin{aligned}\langle\sqrt{x_t x_0}\rangle &= \int_0^\infty\int_0^\infty \mathrm{d}x_0\mathrm{d}x\mathbb{P}(x)\mathbb{P}(x,t|x_0)\sqrt{xx_0}\\ &= \frac{1}{\Gamma(\alpha)}\sum_{n=0}^\infty \frac{n!}{\Gamma(n+\alpha)}\exp\left(-\mathcal{A}nt\right)\\ &\quad\times\left(\int_0^\infty x^{\alpha-1/2}e^{-x}L_n^{\alpha-1}(x)\mathrm{d}x\right)^2\\ &= \frac{1}{\Gamma(\alpha)}\sum_{n=0}^\infty \frac{n!}{\Gamma(n+\alpha)}\exp\left(-\mathcal{A}nt\right)\\ &\quad\times\left(\frac{\Gamma(\alpha+\frac{1}{2})\Gamma(n-\frac{1}{2})}{n!2\sqrt{\pi}}\right)^2\\ &= \frac{\Gamma(\alpha+\frac{1}{2})^2}{\Gamma(\alpha)^2}{}_2F_1(-\frac{1}{2},-\frac{1}{2},\alpha,\exp(-\mathcal{A}t))\end{aligned}\tag{3.47}$$

where we have used formula (C.30). □

3.4.2 Spectral properties of the scattered intensity

Owing to the linear drift in (2.46), the Pearson diffusions share the feature that their normalized covariance function is an exponentially decaying function of time,

$$\mathbb{E}\left[\left(\frac{x_t-m}{v}\right)\left(\frac{x_0-m}{v}\right)\right] = \exp\left(-\mathcal{A}t\right).\tag{3.48}$$

(The mean m and the variance v^2 in the above expression can be deduced from (2.54). Also, x_0 denotes the initial value drawn from the asymptotic distribution, thus ensuring stationarity of the process.) Meanwhile, from the compound expression (3.11), the scattered intensity z_t has a multiplicative representation in terms of two independent processes and its ACF is given by

$$\langle z_t z_0\rangle = \langle u_t u_0\rangle\langle x_t x_0\rangle.\tag{3.49}$$

The dynamics of the process $u_t = |\gamma_t|^2$ proceed from (3.7)

$$\mathrm{d}u_t = \mathcal{B}(1-u_t)\mathrm{d}t + \sqrt{2\mathcal{B}u_t}\mathrm{d}W_t^{(u)} \tag{3.50}$$

where $\gamma_t \mathrm{d}\xi_t^* + \gamma_t^* \mathrm{d}\xi_t = \sqrt{2\mathcal{B}u_t}\mathrm{d}W_t^{(u)}$. As a consequence, u_t also belongs to the class of Pearson diffusions and conforms to (3.48). Therefore, for a texture distribution conforming to the Pearson equation (2.46), the autocorrelation of the resultant intensity reads

$$\langle z_t z_0 \rangle = \left(m^2 + v^2 \exp(-\mathcal{A}t)\right)\left(1 + \exp(-\mathcal{B}t)\right). \tag{3.51}$$

The normalized covariance of the intensity z_t is the product of two exponentially decaying terms with timescales $\mathcal{A}^{-1}$ and $\mathcal{B}^{-1}$ characteristic of, respectively, x_t and u_t (in radar applications, $\mathcal{A}^{-1}$ is typically of the order of many seconds whereas $\mathcal{B}^{-1}$ is of the order of ten milliseconds (Ward et al., 2006)). We also readily observe that the intensity power spectral density is given by

$$\begin{aligned} S_z(\omega) &= m^2\delta(\omega) + v^2\frac{\mathcal{A}}{2\pi(\mathcal{A}^2+\omega^2)} + m^2\frac{\mathcal{B}}{2\pi(\mathcal{B}^2+\omega^2)} \\ &\quad + m^2v^2\frac{(\mathcal{A}+\mathcal{B})}{2\pi((\mathcal{A}+\mathcal{B})^2+\omega^2)}. \end{aligned} \tag{3.52}$$

Equation (3.51) generalizes the expression obtained in Field and Tough (2003b) for a K-distributed amplitude. We have thus encompassed the intensity distributions derived in Delignon and Pieczynski (2002); Balleri et al. (2007) for which we have derived their ACF and spectral properties.

3.5 Numerical methods

3.5.1 Rationale

The SDEs pertaining to the RCS dynamics (3.12) and amplitude dynamics (3.15) may be solved numerically through an Euler–Mayamura method (Tough, 1987; Higham, 2001). For this purpose, let us consider the differential form of an Ito process

$$\mathrm{d}X_t = b(t, X_t)\mathrm{d}t + \Sigma(t, X_t)\mathrm{d}W_t \tag{3.53}$$

with $X(0) = X_0$ and for $0 \leq t \leq T$. The difficulty here is to integrate the Brownian term $\mathrm{d}W_t$ (cf. Appendix B for a brief exposition of the Wiener process). For some positive integer n, let $\delta t = T/n$ be the integration step and $t_j = j\delta_t$. The numerical approximation of the Ito process at time t_j is denoted as $X_j = X(t_j)$. The Euler–Mayamura method takes the form

$$X_j \;=\; X_{j-1} + b_{j-1}\delta t + \Sigma_{j-1}(W_j - W_{j-1}) \quad \text{for } j = 1, .., n \tag{3.54}$$

where W_j denotes a realization of the Wiener process W_t at t_j. For a deterministic process where the volatility term in the r.h.s. of the above equation vanishes, this method reduces to the usual Euler finite difference scheme. The Euler–Mayamura converges slowly (in the order of $\delta t^{1/2}$). More precise outputs may be obtained by considering higher-order integration terms (see Field, 2009, Chap. 11) or (Higham, 2001).

A realization of the Brownian motion at the time $\tau_i = i\delta' t$, where $\delta' t = T/n'$ is the integration step[9], is obtained through

$$W_i = W_{i-1} + \mathrm{d}W_i, i = 1, .., n' \tag{3.55}$$

initialized with $W_0 = 0$ and where each $\mathrm{d}W_i$ is an independent random variable of the form $\sqrt{\delta' t}\mathcal{N}(0, 1)$ (thus satisfying the properties of a Wiener process, cf. Appendix B Section B.1.2). For the sake of simplicity, we may consider $n = n'$, in which case (3.54) reduces to

$$X_j \;=\; X_{j-1} + b_{j-1}\delta t + \Sigma_{j-1} w_i \tag{3.56}$$

where $w_i \sim \mathcal{N}(0, 1)$.

[9] which should satisfy$\delta' t \leq \delta t$ to ensure that the set of points $\{\tau_i\}$ over which the Wiener process is generated contains the points $\{t_j\}$ where the Euler–Mayamura solution is computed

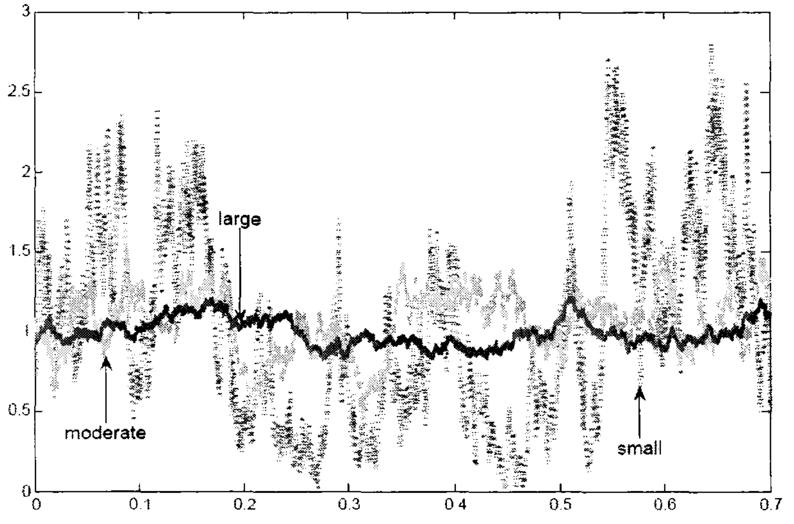

FIGURE 3.1: Dynamics of the Gamma distributed normalized RCS $x_t/\langle x_t \rangle$ for low/moderate/high values of the shape parameter. (For parameters values $\mathcal{A} = 2.5 * 10^{-3}$,$\delta_t = 0.4$, $\alpha = 2, 20, 200$).

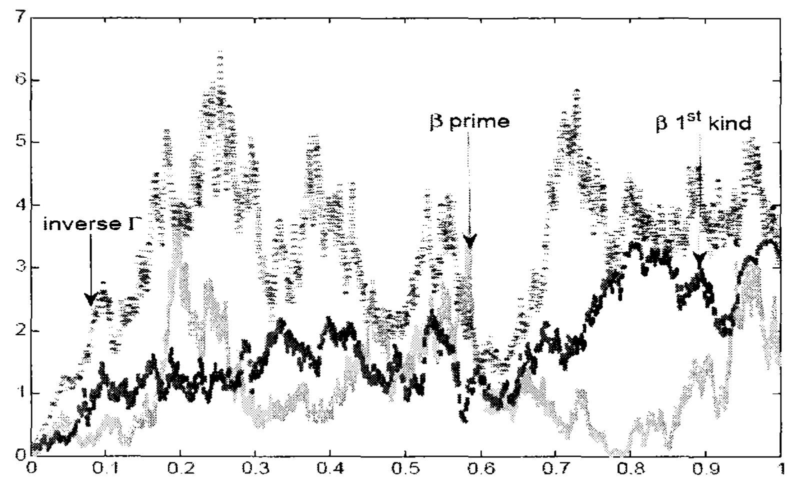

FIGURE 3.2: Dynamics of the RCS for inverse Gamma ($\alpha = 4$), Beta of the first kind ($\beta = 3.5, p = 1.5, q = 1.9$) and Beta prime ($\beta = 2.5, p = 1.2, q = 1.5$) textures. For parameters values $\mathcal{A} = 10^{-3}$ and $\delta_t = 0.05$.

3.5.2 Cross-section

Let us first illustrate this technique by generating samples for the RCS of a $K-$distributed amplitude (3.13). Substituting the drift $b = \alpha - x$ and volatility σ in (3.56) generates a sample path of a RCS whose asymptotic distribution is Gamma. Fig. 3.1 compares three RCS with different parameter values for α, a measure of the sea-state. In effect, the relative variance $R = Var[x_t]/\langle x_t\rangle^2 = 1/\alpha$ is related to the sea-state. A large and small R represent, respectively, a high and calm sea-sate. Other diffusion models may be numerically solved by a similar token. Fig. 3.2 shows the time-evolution of the Pearson diffusions discussed in Section 2.3.2.

3.5.3 Strong scattering

The first step to generate a random sample of the scattered amplitude is to solve numerically the COU process (3.7) (where α is chosen to be large to avoid computational difficulties). The real and imaginary parts of the speckle are plotted in Fig. 3.3. Thereafter, the scattered amplitude is obtained from (3.15) which is more conveniently achieved via the compound representation (3.11) from the (independent) integration of the Rayleigh amplitude (3.7) and of the texture (3.13). The real and imaginary parts of the resultant amplitude are given in Fig. 3.4.

3.5.4 Weak scattering

Finally, the numerical integration of a weakly scattered amplitude (3.30) is closely connected to the strong scattering case - except for the additional coherent offset that is directly adjoined to the simulated strongly scattered amplitude $\Psi_t = \psi_t + e_t$. Fig. 3.5 shows a Rice scattered amplitude which is nothing but a Rayleigh speckle (cf. Fig. 3.3) to which was adjoined a constant offset. Fig. 3.6 gives a realization a HK amplitude which is a shifted version of the K-distributed amplitude shown in Fig .3.4. Finally, a GK amplitude is obtained when the coherent offset is proportional to the RCS Fig. 3.7.

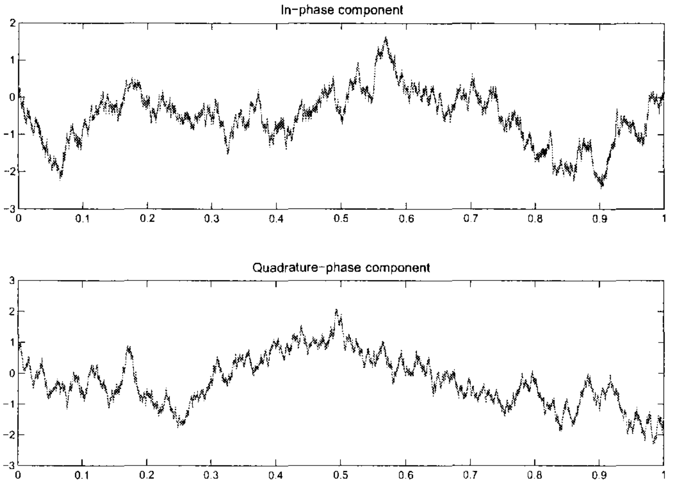

FIGURE 3.3: Dynamics of the Rayleigh speckle γ_t (quadrature- and in-phase components)

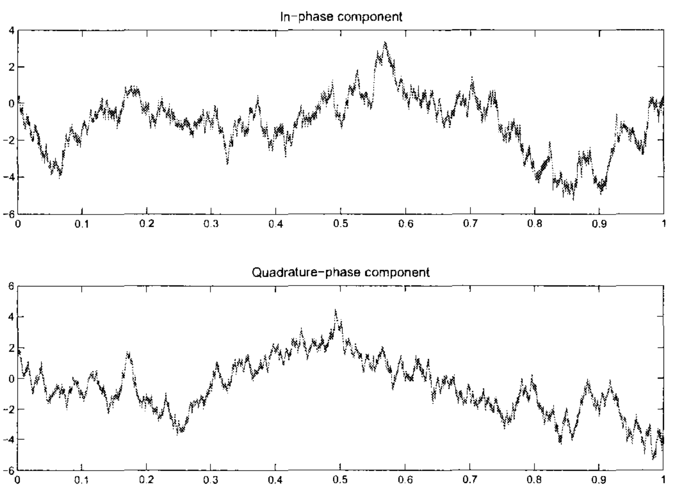

FIGURE 3.4: Dynamics of the K–scattered amplitude ψ_t (quadrature- and in-phase components)

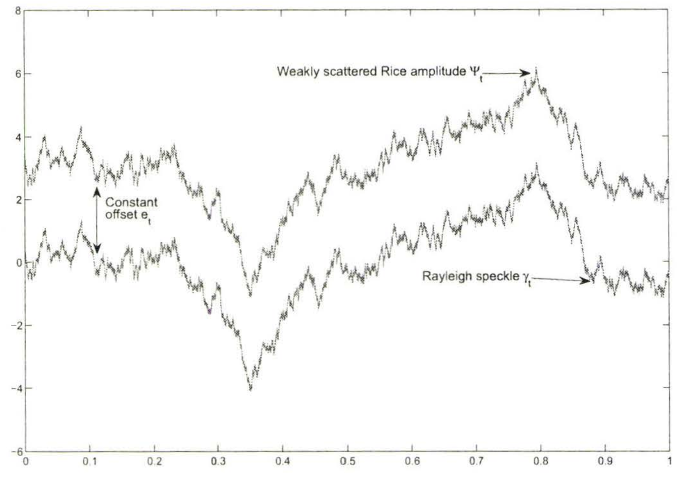

FIGURE 3.5: In-phase component of a Rice distributed amplitude as compared with the Rayleigh speckle.(For parameter values $\mathcal{A} = 10^{-3}$,$\mathcal{B} = 10^{-2}$,$\delta_t = 0.05$,$\alpha = 4$.)

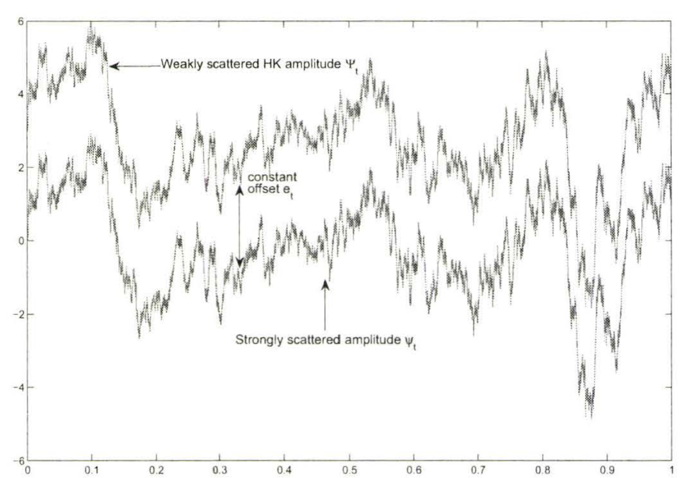

FIGURE 3.6: In-phase component of a HK amplitude for a coherent offset $e_t = 3$. (For parameter values $\mathcal{A} = 10^{-3}$,$\mathcal{B} = 10^{-2}$,$\delta_t = 0.05$,$\alpha = 4$.)

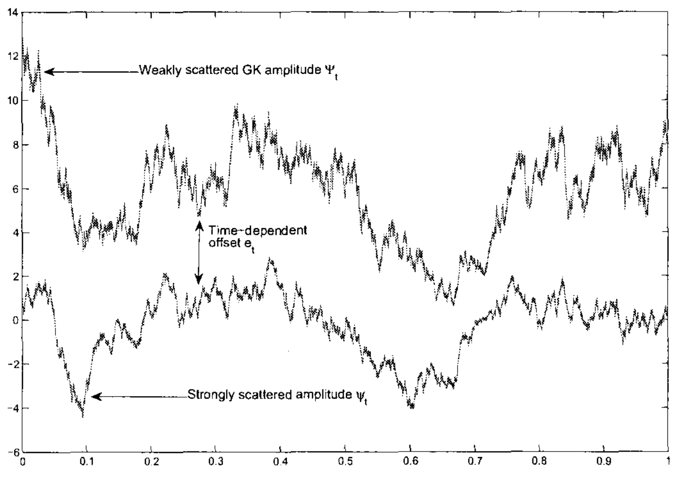

FIGURE 3.7: In-phase component of a GK amplitude for a coherent offset $e_t = 3{*}x_t$. (For parameter values $\mathcal{A} = 10^{-3}$,$\mathcal{B} = 10^{-2}$,$\delta_t = 0.05$,$\alpha = 4$.)

Chapter 4

Observability of the RCS for strong scattering

4.1 Intensity-weighted fluctuations of the phase

4.1.1 Objective

The multiplicative nature of the scattered amplitude (3.11) was derived from the random walk model (2.1) and involves two components that have quite distinct experimental significations: the speckle, the amplitude scattered for a large but constant number of scatterers, and the texture, which is connected to the time-evolution of the scatterers' population. Moreover, the former is of electromagnetic essence, as a measure of the scattering pattern from a particular scatterer whereas the latter is related to the sea level whose time evolution will influence the number of scatterers seen by the radar. Then, if a target happens to be present within the illumination range of the radar, it will influence the texture but not the speckle. Thus, extracting x_t from the received amplitude facilitates methods for anomaly detection.

Many radar detection algorithms are based on frequency agility (see Ward et al., 2006, Chap. 8) or Watts (1985); Shnidman (1995) in order to de-correlate the speckle. If the radar frequency changes, the speckle will be correspondingly modified (but the texture won't). Two different frequencies are said to be de-correlated if their difference causes a change of phase of a least 2π for the clutter patch. Consequently, for a frequency step equal to the radar bandwidth, successive pulses will be de-correlated. Detection is enabled by setting a threshold level for the received amplitude convoluted over the pulses.

Instead of this classical procedure, a novel approach to detect targets is embedded with the stochastic model described in Chapter 3. The exact dynamics of the scattered amplitude it provides permits the design of an inference algorithm for the texture, in local time, from the received scattering pattern. This chapter builds upon this approach, pioneered by Field for a strongly scattered amplitude (cf. Field and Tough, 2003a,b, for, respectively, experimental evidence and theoretical description).

4.1.2 Inference

If we consider the square of (3.26), we obtain the following result (*orig.* Field, 2005).

Proposition 4.1. The instantaneous values of the scattering cross-section are observable through the intensity-weighted squared phase fluctuations according to

$$x_t = \frac{2}{\mathcal{B}} z_t \mathrm{d}\theta_t^2 / \mathrm{d}t \tag{4.1}$$

if x_t is an Ito process, not necessarily a diffusion, and throughout space and time.

This result emerges as a geometrical feature of the random walk representation of the scattered amplitude and can be traced to the independence between the radial and angular fluctuations of the scattering amplitude. It is neither affected by the scatterers' dynamics x_t nor by the phasors' magnitude ($\{a_j\}$ in (2.1)) as long as they are drawn independently from an arbitrary distribution. In (4.1), the inferred RCS scales with $\mathcal{B}$. For anomaly detection, knowing the RCS up to proportionality is sufficient.

A slight complication is posed in the computation of $\mathrm{d}\theta_t^2$ from experimental data, owing to the discontinuous-valued behaviour of θ_t at coordinate intervals of

2π (Field, 2005). This is resolved by instead using the (continuous-valued) phase-wrapped process $w_t = \exp(i\theta_t)$, whose stochastic differential is $\mathrm{d}w_t = \exp(i\theta_t)\left[i\mathrm{d}\theta_t - \frac{1}{2}\mathrm{d}\theta_t^2\right]$, which enables the squared phase fluctuations to be computed from the single-valued process w_t via $|\mathrm{d}w_t|^2 = \mathrm{d}\theta_t^2$. In respect of discrete-time implementation, we remark that if W_t is a Wiener process, then $\delta W_t = W_{t+h} - W_t$ is normally distributed as $\mathcal{N}(0, h)$, so that its square is a chi-squared $\chi^2(1)$ variable. The sum of n such variables is therefore distributed as $\chi^2(n)$, from which an estimate of $\mathrm{d}q_t^2$ from δq_t can be obtained (via the weak law of large numbers) by considering the interval from t to $t + \delta t$ divided into n pulse intervals each of length h and letting $n \to \infty$ before taking the limit $\delta_t \to \mathrm{d}t$.

The structure of the SDEs pertaining to the population and to the intensity dynamics (recalled below from (3.12) and (3.19)) provides some insight into (4.1).

$$\mathrm{d}x_t = \mathcal{A}b_t\mathrm{d}t + (2\mathcal{A}\sigma_t)^{\frac{1}{2}}\,\mathrm{d}W_t^{(x)} \tag{4.2}$$

$$\begin{aligned}\mathrm{d}z_t &= \left[\mathcal{A}\left(\frac{b_t z_t}{x_t}\right) + \mathcal{B}(x_t - z_t)\right]\mathrm{d}t \\ &\quad +(2\mathcal{A}\sigma_t)^{\frac{1}{2}}\left(\frac{z_t}{x_t}\right)\mathrm{d}W_t^{(x)} + (2\mathcal{B}x_t z_t)^{\frac{1}{2}}\,\mathrm{d}W_t^{(r)}.\end{aligned} \tag{4.3}$$

This coupled system of SDEs could be interpreted as an instance of the generalized Kalman filter (see Øksendal, 1988, Chap. 6) in which the unknown state x_t is to be estimated from observations of z_t. It is instructive that in this situation the dynamics of the filter stem from first principles and that the resulting statistics are non-Gaussian (notwithstanding the Gaussian nature of the Wiener process). The noise originates through two components, namely the intrinsic system noise $W_t^{(x)}$ which derives from fluctuations in the (endogenously specified) population model, and the measurement noise ξ_t arising from the particulars of the wavelike interference effects. The latter should be viewed as an exogenous device whose purpose is to probe the true underlying state of the system that is of primary interest, in the case of the signal x_t. This statement is reminiscent of earlier results for the error on a frequency modulation determination based on measurements of the intensity-weighted phase (Jakeman and Watson, 2001; Watson et al., 2006). As contrasted to this earlier work which assumes a differentiable phase, herein we consider the quadratic variation of the phase $d\theta_t^2$ and θ_t is taken as a non-differentiable process.

4.1.3 Experimental implications

Although valid for values drawn from experiments, the efficiency of (4.1) is more conveniently verified through synthetically generated data. In effect, the inferred state that is to be estimated from the observed state (the intensity) could in that case be compared with the hidden state (known from the simulation), enabling us to quantify the accuracy of the inference. In particular, this permits the computation of the discrepancy between the hidden and the estimated cross-sections, an experimental measure to be compared with its theoretical counterpart.

We generate a distributed scattered amplitude ψ_t, which is more conveniently achieved by the (independent) integration of the texture and the speckle (cf. Euler–Mayamura scheme in Section 3.5). Since the intensity and phase fluctuations time-series are known, an estimate for the RCS may be obtained through Proposition 4.1 which implies, for discretely sampled data,

$$z_i \delta\theta_i^2 \;\propto\; x_i n_i^2 \tag{4.4}$$

where i is a discrete time index and $\{n_i\}$ are an independent collection of $\mathcal{N}(0,1)$ distributed random variables (i.e., x_i denotes the value of the process x_t for the discrete value $t = i\delta_t$, where δ_t is the sampling interval). Applying a smoothing average $\langle . \rangle_{\boldsymbol{\Delta}}$ to the left-hand side (the observations) of (4.4) with window $\boldsymbol{\Delta} = [t_0 - \Delta\delta_t, t_0 + \Delta\delta_t]$ yields an approximation to x_{t_0}, with an error that tends to zero as the number of pulses inside $\boldsymbol{\Delta}$ tends to infinity and $\boldsymbol{\Delta} \to 0$ (see discussion of χ^2 statistics following Proposition 4.1). Further on, we shall consider a variety of texture models for which the estimated RCS obtained through (4.4) is plotted against the exact RCS known from the simulation.

4.1.4 Examples

4.1.4.1 Gamma distributed texture

To illustrate Proposition 4.1, let us first consider a Gamma distributed cross-section (2.40) -the usual texture for a K-distribution. The drift and volatility coefficients in (3.12) are given, respectively, by $b = \alpha - x$ and $\sigma = x$. Fig. 4.1 compares the exact cross-section from the cross-section inferred through the intensity-weighted fluctuations of a the phase, averaged over a smoothing window of Δ samples, according to the token described by (4.4). They exhibit a correlation coefficient of 0.9959.

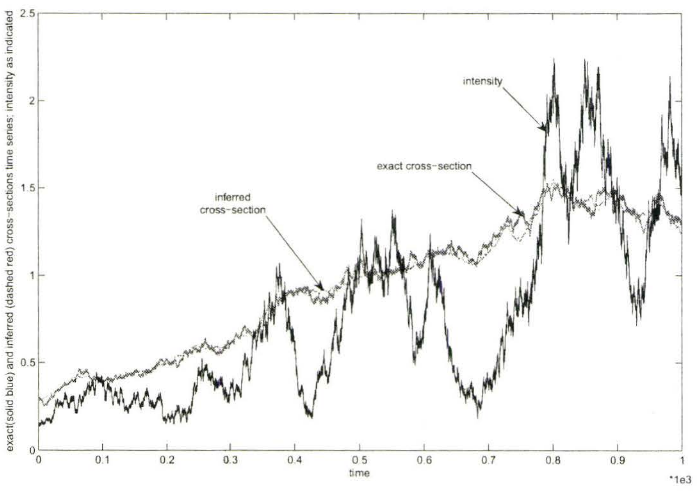

FIGURE 4.1: Estimation of the RCS/population through the effect of phase decoherence for a Gamma distributed texture. (For parameter values $\alpha = 10$, $\mathcal{A} = 10^{-3}$, $\mathcal{B} = 10^{-2}$.)

4.1.4.2 Other Pearson distributions

The class of Pearson diffusions yields candidate probability distributions to model the scattered amplitude's texture (refer to Section 2.3.2 for their derivation on the basis of a discrete population model). The simulation described in 4.1.4.1 is repeated for the three other Pearson distributions discussed therein. The simulation for an inverse

Gamma distribution, i.e., $b = \alpha - x$ and $\sigma = x^2$, was published in Fayard and Field (2009) . Finally, we consider the Beta distribution with parameters $b = \beta p/(p+q) - x$, $\sigma = (\beta x - x^2)/(p+q)$ and the Beta prime distribution $b = \beta p/(q-1) - x_t$ and $\sigma = (\beta x_t + x_t^2)/(q-1)$ that were both investigated in Fayard and Field (2010a). Figs. 4.2(a),4.2(b) and 4.2(c) illustrates how the cross-section can be recovered from the intensity fluctuations thanks to Proposition 4.1.

We have hereby verified the accuracy of Proposition 4.1 for several texture models. Whichever the drift and volatility parameters considered, the inferred RCS was a good estimate of the exact cross-section.

4.1.5 Anomaly detection: toy example

To illustrate the interest of this technique, let us recall a simulation from Fayard and Field (2010b). We shall remind the reader that a target within the radar illumination range will yield a discontinuity in the texture temporal evolution. In the following figure, a constant offset was arbitrarily added to the normal RCS time-evolution to emulate a target. The blue and red curves give the inferred RCS (according to the token given in Proposition 4.1) obtained from the scattering amplitude, respectively, in the presence of this target (discrete jump) or without the target. The blue curve exhibits a clear discontinuity which, translated into the texture temporal evolution, is synonymous to an anomaly detection. On the other hand, the intensity time-series, which is also impacted by the jump through (3.11), does not have any visible discontinuity since the RCS jump is concealed by the rapid fluctuations of the speckle. This example illustrates why the inference of the RCS facilitates means for anomaly detection. In particular, we observe that this technique works for a non-stationary process (which is highly desirable for anomaly detection).

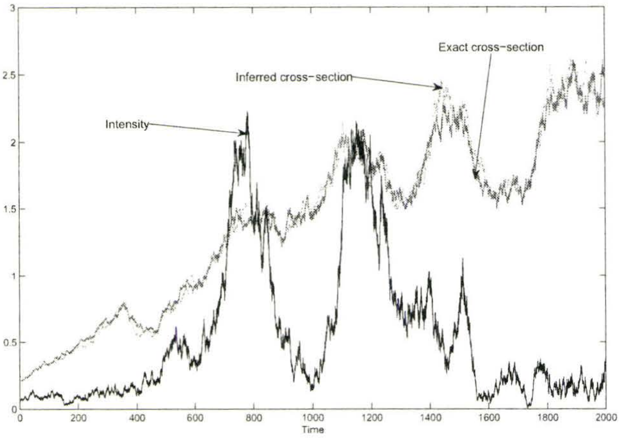

(a) inverse Gamma ($\alpha = 4$)

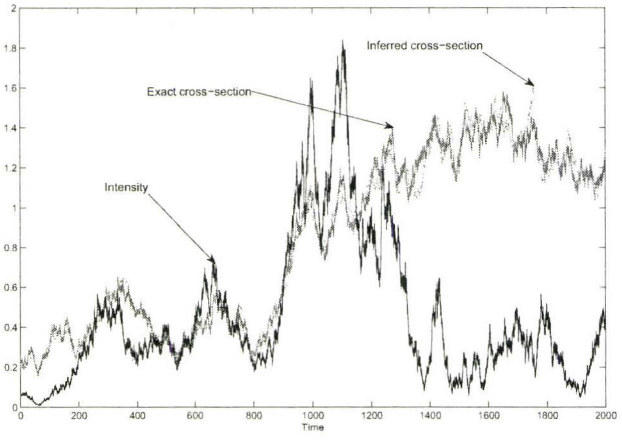

(b) Beta of the first kind ($q = 1.9$, $p = 1.5$, $\beta = 3.5$)

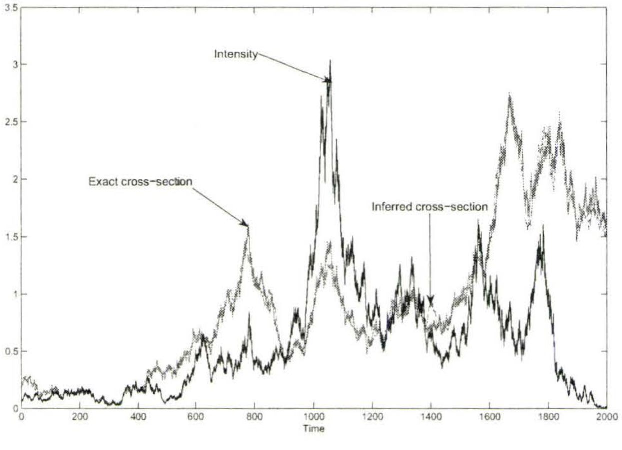

(c) Beta prime ($p = 1.2$, $q = 1.5$, $\beta = 2.5$)

FIGURE 4.2: Inference of the RCS for an three Pearson diffusions. (For parameter values $\mathcal{A} = 10^{-4}$, $\mathcal{B} = 10^{-3}$, $\delta_t = 0.05$).

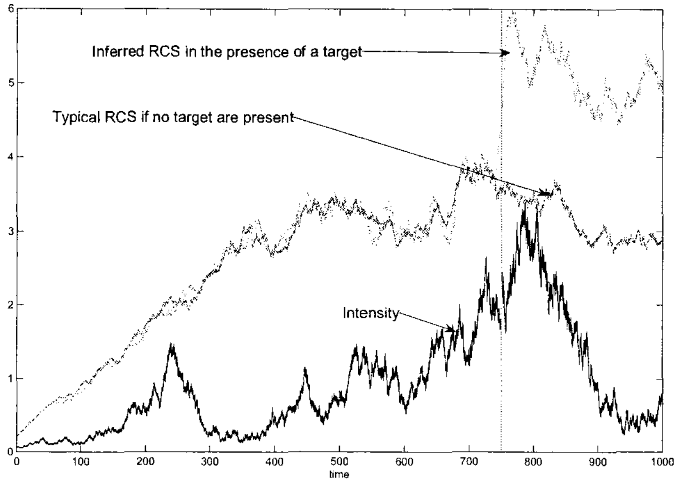

FIGURE 4.3: Inference of the RCS when a target is present and resulting anomaly. (For parameter values $\mathcal{A} = 10^{-4}$, $\mathcal{A} = 10^{-3}$, $\delta = 0.1$, $\alpha = 4$)

4.2 Optimization

4.2.1 Propositions

The inference procedure (as illustrated in 4.1,4.2(a),4.2(b),4.2(c)) offers an accurate estimate of the unknown RCS - as evidenced by the strong correlation coefficient between the exact and inferred RCSs. Nevertheless, a discrepancy emerges while smoothing the intensity weighted phase fluctuations. In effect, for a numerical simulation where the pulse rate must be finite, the estimated state will differ from the true hidden state; the convergence being obtained only in the (unfeasible) case where the pulse rate tends to infinity (as anticipated in Section 4.1.3). The resulting deviation, in the sense of the mean square error (MSE), for a given δ_t, will moreover depend on the window length Δ and can be measured by the error function

$$\epsilon_{\text{sm}}(\Delta) = \mathbb{E}\left[\sum_{i=1}^{N}(x_i^{\text{sm}} - x_i)^2\right] \tag{4.5}$$

where x_i^{sm} denotes the average of $z_i\delta\theta_i^2$ over a window $\boldsymbol{\Delta}$ and x_i the exact cross-section.

A follow-up question is how to determine Δ, the length of the smoothing window over which the phase fluctuations are averaged- the window must neither be so large that the structure of the temporal variation is lost, nor too small that an average over the normal random seeds is no longer affected. This issue was addressed in Fayard and Field (2008) for the K–distributed case for which the following results hold.

Proposition 4.2. *The discrepancy between the cross-section inferred from the intensity-weighted phase fluctuations of a K–distributed amplitude and the underlying cross-section is given by*

$$\epsilon_{\rm sm} = \mathbb{E}\left[\sum_{i=1}^{N} x_i^2\right]\frac{2}{\Delta} + \mathbb{E}\left[\sum_{i=1}^{N} x_i\right]\frac{\mathcal{A}\delta_t}{6}\Delta. \tag{4.6}$$

where Δ denotes the number of samples over which the phase fluctuations are averaged.

which has the following corollary

Proposition 4.3. *The cross-section is optimally recovered when the intensity-weighted squared fluctuations of the phase are averaged over a window of length*

$$\Delta^{\rm opt} = \left(\frac{12}{\mathcal{A}\delta_t}\frac{\mathbb{E}\left[\sum_{i=1}^{N} x_i^2\right]}{\mathbb{E}\left[\sum_{i=1}^{N} x_i\right]}\right)^{1/2}. \tag{4.7}$$

We readily check that $\partial^2\epsilon_{\rm sm}/\partial\Delta^2 > 0$, so $\Delta^{\rm opt}$ is indeed a minimum. Calculus properties ensure that for the optimal window length, $\epsilon_{\rm x_i}$ and $\epsilon_{\rm n_i}$ exactly compensate. Moreover, for this particular window length, the MSE error is

$$\epsilon_{\rm sm}(\Delta^{\rm opt}) = \sqrt{\frac{4}{3}\mathcal{A}\delta_t\sum_{i=1}^{N}\mathbb{E}\left[x_i^2 + x_i\right]}. \tag{4.8}$$

We observe that the expression for $\Delta^{\rm opt}$ depends only on the population characteristics. In particular, the dynamics of the scattered amplitude (phase or intensity) do not intervene, e.g. the time constant $\mathcal{B}^{-1}$ does not appear. It is likewise noteworthy that the values of the phase de-coherence (which the cross-section is extracted from) are irrelevant to the discussion of their smoothing. Also, even though x_i appears in the numerator as well as in the denominator, we must stress that in the latter it represents the volatility term σ_t whereas the former is not directly related to the SDE (i.e., valid for an arbitrary population). It is worth investigating the case of an infinite sampling rate (i.e., $\delta_t \to 0$), which has been anticipated in the discussion following the cross-section inference. We remark that the (normalized) window length Δ^{opt} tends to infinity, whereas the (actual) window length $\Delta^{\text{opt}} * \delta_t$ tends to zero. Accordingly, the corresponding error (4.8) vanishes in this limit.

4.2.2 Proof

4.2.2.1 Rationale

We first notice that $\mathrm{d}W_t^{(\theta)}$ is independent from x_t owing to the independence between γ_t and x_t (as can be seen from (3.11) and (3.27)). Since n_t was introduced from $\mathrm{d}W_t^{(\theta)} = n_t(\mathrm{d}t)^{1/2}$, it is also independent of x_t and (4.4) becomes

$$\langle x_i \rangle_{\boldsymbol{\Delta}} \quad \propto \quad \frac{\langle z_i \mathrm{d}\theta_i^2 \rangle_{\boldsymbol{\Delta}}}{\langle n_i^2 \rangle_{\boldsymbol{\Delta}}} \tag{4.9}$$

if we assume that $\boldsymbol{\Delta}$ is small w.r.t. the characteristic time $\mathcal{A}^{-1}$ of the cross-section [1]. This condition is ensured since the Gamma-distributed component is constant over a beam dwell time (Ward et al.).

Equation (4.9) gives some insight into the understanding of the error due to the phase de-coherence smoothing. If Δ is small, the variance of the averaged $\langle n_i^2 \rangle_{\boldsymbol{\Delta}}$ is high and makes the inferred state diverge from the weighted phase fluctuations in (4.9). On the other hand, a large window length, although guaranteeing $\langle n_i^2 \rangle_{\boldsymbol{\Delta}} = 1$, will cause the averaged phase fluctuations $\langle z_i \mathrm{d}\theta_i^2 \rangle_{\boldsymbol{\Delta}}$ not to capture well enough the instantaneous variations of the phase de-coherence. Then, the smoothing process is

[1] for practical experiments, the characteristic time $\mathcal{A}^{-1}$ is of the order many seconds (if not minutes). The sampling time is in the range of milliseconds (cf. Ward et al., 2006)

a trade-off between the lost of information (i.e., $\langle z_i \mathrm{d}\theta_i^2\rangle_{\boldsymbol{\Delta}}$ is not accurate enough), and a sensitivity to the sampling process (i.e., $\langle n_i^2\rangle_{\boldsymbol{\Delta}}$ is volatile w.r.t. to its mean 1). Since those two sources of error, respectively labeled $\epsilon_{\mathrm{x_i}}$ and $\epsilon_{\mathrm{n_i}}$, vanish when Δ is small and large respectively, they represent the asymptotic behaviour of the total error (4.5) for the extreme values of Δ.

Under the hypothesis that the total error ϵ_{sm} can be approximated by these two asymptotes, we can guess that the MSE discrepancy between the inferred cross-section and the hidden one will posses (w.r.t. the window length Δ) a shape that exhibits a minimum Δ^{opt} optimizing the smoothing process. We first confine our derivations to the Gamma distributed texture that yields the K–distribution for the scattered intensity.

4.2.2.2 Error due to the x_i's

When $\Delta \gg \Delta^{\mathrm{opt}}$ the prominent error arises from $\langle x_i\rangle_{\boldsymbol{\Delta}} \neq x_i$ whereas $\langle n_i^2\rangle_{\boldsymbol{\Delta}} \simeq 1$, and (4.5) may be written as

$$\epsilon_{\mathrm{x_i}} = \sum_{i=1}^{N} \mathbb{E}\left[(\langle x_i\rangle_{\boldsymbol{\Delta}} - x_i)^2\right] \tag{4.10}$$

where $\langle x_i\rangle_{\boldsymbol{\Delta}}$ denotes $\frac{1}{\Delta}\sum_{j=-\frac{\Delta}{2}}^{\frac{\Delta}{2}} x_{i+j}$.

To proceed further, let us consider the discrete SDE for the population dynamics (3.13), given the sampling interval δ_t,

$$x_{i+1} = (1-\mathcal{A}\delta_t)x_i + \alpha\mathcal{A}\delta_t + (2\mathcal{A}\delta_t x_i)^{\frac{1}{2}}\, w_i \tag{4.11}$$

where $w_i \sim \mathcal{N}(0,1)$, or

$$x_{i+1} \simeq x_i + \alpha\mathcal{A}\delta_t + (2\mathcal{A}\delta_t x_i)^{\frac{1}{2}}\, w_i \tag{4.12}$$

where it is taken for granted that the dimensionless constant $\mathcal{A}\delta_t$ verify $\mathcal{A}\delta_t \ll 1$; this condition is contained within a previous assumption used to write (4.9), namely $\mathcal{A}\Delta \ll 1$, since $\boldsymbol{\Delta}$ is normalized by δ_t. It has to be understood as the sampling time δ_t being small w.r.t. the correlation time of the cross-section $\mathcal{A}^{-1}$ or, in other words, the fluctuations of the population level being negligible within a sampling window.

If we now iterate (4.12), we can write

$$x_{i+j} = x_i + j\alpha\mathcal{A}\delta_t + \mathrm{sgn}(j)\sum_{k=1}^{|j|}(2\mathcal{A}\delta_t x_{i+l})^{\frac{1}{2}}\, w_{i+l} \tag{4.13}$$

where sgn(j) denotes the sign of j (its instance in front of the sum may be removed due to the symmetry of w_{i+l}). We have defined $l \equiv i + k - 1$ for positive j's and $l \equiv i - k$ for negative ones. If we examine carefully this expression, we notice that it tells us that any sample x_{i+j} is weighted with a deviation from the median value over the window $\langle x_i \rangle_{\boldsymbol{\Delta}}$, that deviation being partly stochastic in nature. If we substitute (4.13) in (4.10),

$$\begin{aligned}\epsilon_{\mathrm{x_i}} &= \frac{1}{\Delta^2}\sum_{i=1}^{N}\mathbb{E}\Bigg[\Bigg(\sum_{j=-\frac{\Delta}{2}}^{\frac{\Delta}{2}}\Big[j\alpha\mathcal{A}\delta_t \\ &\qquad +\mathrm{sgn}(j)\sum_{k=1}^{|j|}(2\mathcal{A}\delta_t x_l)^{\frac{1}{2}}w_l\Big]\Bigg)^2\Bigg].\end{aligned} \tag{4.14}$$

We notice that the first term in the inner sum, $j\alpha\mathcal{A}\delta_t$, is odd, and therefore its summation over an even interval is zero. Then, we expand the square product and use the independence between n_t and x_t (w_t being a function of n_t),

$$\epsilon_{\mathrm{x_i}} = \frac{1}{\Delta^2}\sum_{i=1}^{N}\left[2\mathcal{A}\delta_t \sum_{j=-\frac{\Delta}{2}}^{\frac{\Delta}{2}}\sum_{j'=-\frac{\Delta}{2}}^{\frac{\Delta}{2}} \mathrm{sgn}(j)\mathrm{sgn}(j')\sum_{k=1}^{|j|}\sum_{k'=1}^{|j'|}\left(\mathbb{E}[x_l^{\frac{1}{2}}x_{l'}^{\frac{1}{2}}]\right)\left(\mathbb{E}[w_l w_{l'}]\right)\right]. \quad (4.15)$$

The summation above is firstly simplified by noticing that the right hand expectation is non-zero if and only if j, j' are of the same sign, a condition fulfilled by introducing a factor 1/2. Moreover from $\sum\sum\mathbb{E}[w_l w_{l'}] = \min(|j|,|j'|)$, the formula reduces to (under the assumption that $\sum x_{i+k}w_{i+k} \simeq \sum x_i w_{i+k}$)

$$\epsilon_{\mathrm{x_i}} = \frac{1}{\Delta^2}\sum_{i=1}^{N}\left[\mathcal{A}\delta_t\mathbb{E}[x_i]\sum_{j=-\frac{\Delta}{2}}^{\frac{\Delta}{2}}\sum_{j'=-\frac{\Delta}{2}}^{\frac{\Delta}{2}}\min(|j|,|j'|)\right] \quad (4.16)$$

$$\epsilon_{\mathrm{x_i}} = \frac{\mathcal{A}\delta_t}{\Delta^2}\left(\mathbb{E}\sum_{i=1}^{N}x_i\right)\left(4\sum_{j=0}^{\frac{\Delta}{2}}j^2\right). \quad (4.17)$$

The step from (4.16) to (4.17) is purely geometrical. Finally, we recall the well-known expression $\sum_{i=0}^{n} i^2 = n(n+1)(2n+1)/6$ according to which (for a large Δ),

$$\epsilon_{\mathrm{x_i}} = \left(\frac{\mathcal{A}\delta_t\mathbb{E}\left[\sum_{i=1}^{N}x_i\right]}{6}\right)\Delta. \quad (4.18)$$

The error increases linearly with the smoothing window length. The above formula incorporates the volatility of the population ($\sigma(x) = x$ for K–scattering). It therefore results as a property of the cross-section SDE, which produces changes over a timescale of order $\mathcal{A}^{-1}$.

4.2.2.3 Error due to the n_i's

Armed with the idea that the dominant term in the error when $\Delta \ll \Delta^{\mathrm{opt}}$ arises from the variance of the samples n_i, i.e. $\langle n_i^2 \rangle_\Delta \neq 1$, whereas $\langle x_i \rangle_\Delta \simeq x_i$ since the window length is small, we can approximate (4.5) by

$$\begin{aligned}
\epsilon_{\mathrm{n_i}} &= \sum_{i=1}^{N} \mathbb{E}\left[\left(\langle n_i^2 \rangle_\Delta \, x_i - x_i \right)^2 \right] && (4.19)\\
&= \sum_{i=1}^{N} \mathbb{E}\left[x_i^2 \right] \mathbb{E}\left[(\langle n_i^2 \rangle_\Delta - 1)^2 \right] && (4.20)\\
&= \frac{2}{\Delta} \left(\sum_{i=1}^{N} \mathbb{E}\left[x_i^2 \right] \right). && (4.21)
\end{aligned}$$

We used above the property that the variance of the mean of N i.i.d. random variables is the variance of one divided by N and, as previously mentioned, the independence between n_t and x_t. Furthermore, since $n_t \sim \mathcal{N}(0,1)$, $n_t^2 \sim \chi^2(1)$ and $\mathrm{Var}[n_i^2] = 2$.

As expected, that error decreases with the smoothing window length. It is noteworthy that this formula does not take explicit account of the population SDE, it is valid for arbitrary dynamics. As justified in Section 4.2.1, writing the smoothing error as the summation of its two asymptotic expressions (4.18) and (4.21) yields Props. 4.2 and 4.3.

4.2.3 Evaluation of Δ^{opt}

If the cross-section reaches its statistical equilibrium density, it observes a Gamma distribution, where $\langle x \rangle = \mathrm{Var}[x] = \alpha$. Then, (4.7) reduces to

$$\Delta^{\mathrm{opt}} = \left(\frac{12(\alpha+1)}{\mathcal{A}\delta_t} \right)^{1/2} \tag{4.22}$$

and can be numerically evaluated.

A contrario, to obtain a numerical value when the equilibrium density has not been achieved, we need to approximate the ratio of the sums in (4.7) as

$$\frac{\mathbb{E}\left[\sum_{i=1}^{N} x_i^2\right]}{\mathbb{E}\left[\sum_{i=1}^{N} x_i\right]} \simeq \frac{\int_0^t x_s^{\mathrm{drift}\,2}\, ds}{\int_0^t x_s^{\mathrm{drift}}\, ds} \tag{4.23}$$

where x_s^{drift} is the drift only solution of (3.13) satisfying

$$x_s^{\mathrm{drift}} = \alpha + (x_0 - \alpha)\exp(-\mathcal{A}s). \tag{4.24}$$

Even though such a process does not capture the volatility of the cross-section, it accounts for the average spread (stochastic velocity). Following the hypothesis of (4.23) leads to an approximation of Δ^{opt} for a non-equilibrium population, at time t,

$$\Delta^{\mathrm{opt}} = \left(\frac{12}{\mathcal{A}\delta_t}\frac{\mathcal{A}\alpha^2 t + 2\alpha(x_0-\alpha)(1-\exp(-\mathcal{A}t)) + \frac{1}{2}(x_0-\alpha)^2(1-\exp(-2\mathcal{A}t))}{\mathcal{A}\alpha t + (x_0-\alpha)(1-\exp(-\mathcal{A}t))}\right)^{1/2}. \tag{4.25}$$

The equilibrium cross-section distribution is attained for large time, $t \to \infty$. However, the corresponding limit of (4.25) does not reduce to the statistical equilibrium solution (4.22), because the volatility was not taken into account for the former expression.

4.2.4 Experiment

In the case of K-scattering, the validity of (4.6) is established by computing the MSE deviation between the inferred (cf. Proposition 4.1 and following discussion) and the exact cross-sections over a range of window length Δ (normalized in terms of the sampling interval δ_t). Fig. 4.4 shows that the analytical error from (4.6) (solid line) captures accurately the experimental error (circles), both of them averaged over 50 repetitive runs. As expected, there exists an optimum Δ^{opt} that optimizes the filtering error. For practical experiments (unknown exact cross-section), (4.7) guarantees the best achievable estimate of the underlying cross-section (more precisely, its expectation) whatever the phase fluctuations should be. The (dimensionless) condition $\mathcal{A}\boldsymbol{\Delta} \ll 1$ is also verified to be reasonable within the experimental parameters. The procedure to detect anomalies in the RCS (cf. Proposition 4.1), as described in Field (2005), is enhanced by selecting this particular smoothing window.

The demonstration above was based on the MMSE criterion to compare the exact and the inferred cross-sections. In spite of scale invariance of (4.1), the MMSE criterion is not appropriate if $\alpha \to \infty$ (since then $\langle x \rangle \to \infty$). Another criterion should then be used, the (invariant under scaling) correlation coefficient. It can be quantitatively verified (cf. Fig. 4.5) that the correlation coefficient is also maximized for the window length given in (4.7).

For a given instance of the cross-section inference, Δ^{opt} is only the expectation of the optimal window length, rather than being the optimal value for this very realization. But since the error surface is nearly flat around its extremum, we can expect that probabilistic value to fit most practical instances.

4.2.5 Sensitivity to parameters

The expression for the optimal window length (4.7) depends on cross-section parameters, namely its characteristic time $\mathcal{A}^{-1}$ and its equilibrium value α. A measure of the robustness for our analytical expression is provided in Tab. 4.1 which shows the deviation (in percentage) between the theoretical Δ^{opt} and its corresponding experimental value (known from the simulation). Over these varying ranges for α and $\mathcal{A}$, one may verify the exactness of the proposed formula. For radar applications, $\mathcal{A}^{-1}$ represents the modulation timescale of the radar cross-section. The relative variance, defined as $R = \mathrm{Var}[x]/\langle x \rangle = 1/\alpha$, is related to the sea behaviour. A large and small R represent, respectively, a high and calm sea state. The parameter α therefore depicts the sea state.

For practical instances, the parameters α and $\mathcal{A}$ may be unknown, requiring their separate deduction from the data. In the context of K–scattering, the shape

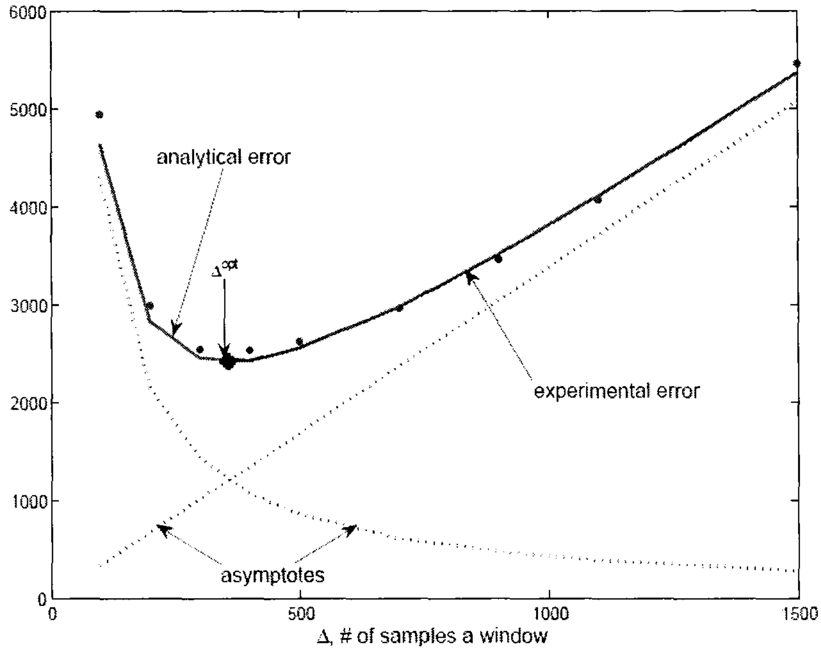

FIGURE 4.4: Comparison of the analytical and experimental MSE deviation between the inferred and the exact cross-sections/populations for different smoothing window lengths. The optimal window length is clearly apparent and experimentally verified. Also shown are the asymptotic expressions of the error. (For parameter values $\alpha = 10$, $\mathcal{A} = 10^{-3}$, $\mathcal{B} = 10^{-2}$.)

parameter of the compound K–distribution ν is connected to the parameter α of the stationary cross-section distribution (2.40) as $\nu = \alpha - 1$ (cf. Field and Tough, 2003a), allowing the latter to be deduced from raw data of the K–distributed intensity.

As a consequence of the compound representation (3.11), the scattered amplitude spectrum is the convolution of the cross-section square root $r_t = x_t^{1/2}$ with the Rayleigh amplitude γ_t: $S_\psi = S_r * S_\gamma$. Their respective correlation time characteristics $\mathcal{A}^{-1}$ and $\mathcal{B}^{-1}$ will therefore occur in the scattered amplitude spectrum. In the time domain, the amplitude ACF recalled from (3.42) reads

$$\langle \psi_t \psi_0^* \rangle \;=\; {}_2F_1\Big(-\frac{1}{2}, -\frac{1}{2}, \alpha, \exp(-\mathcal{A}t)\Big) \exp\left(-\mathcal{B}t/2\right) \tag{4.26}$$

for $t \geq 0$ and where $\langle \psi_t \psi_0^* \rangle$ is a symmetric function of time.

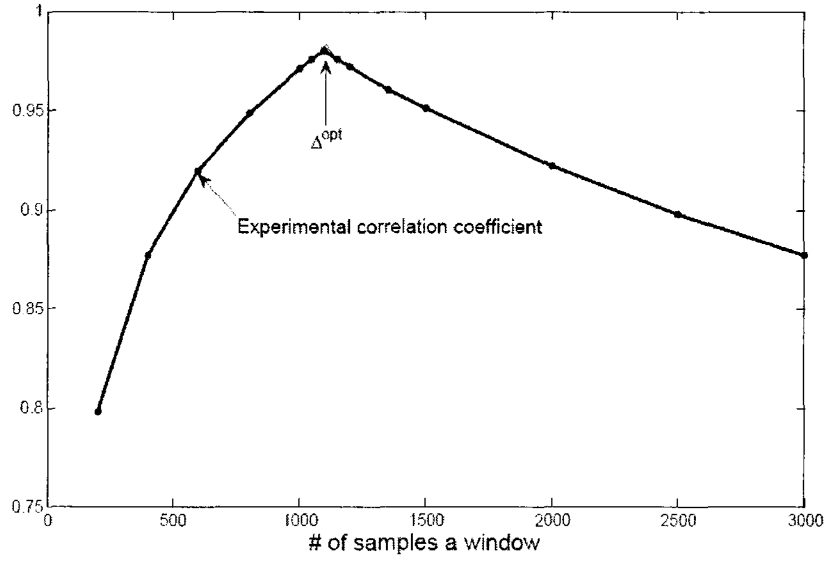

FIGURE 4.5: Correlation coefficient c between the exact RCS and the inferred RCS for different smoothing window lengths. For the sake of visualization, the correlation function shown is $M - (M - c)^{1/2}$ where $M = sup(c)$. (For parameter values $\alpha = 10$, $\mathcal{A} = 10^{-3}$, $\mathcal{B} = 10^{-2}$.)

The time characteristics $\mathcal{A}$ and $\mathcal{B}$, which satisfy $\mathcal{A} \ll \mathcal{B}$, may be found from the experimental autocorrelation by fitting its parameters as compared to its theoretical expression (4.26). From the series expansion of the hypergeometric function, the RCS component of the resultant amplitude autocorrelation (4.26) may be written as a sum of terms proportional to $\exp(-n\mathcal{A}t)$, whose spectra are therefore Cauchy or 'Lorentzian', while the Rayleigh spectral component is also Cauchy.[2] Since the Cauchy distribution is stable (Nolan, 2005), via the Fourier convolution $S_\psi = S_r * S_\gamma$, and taking the leading ($n = 1$) term in the hypergeometric expansion, it follows that the spectrum of the resultant amplitude ψ is also (approximately) Cauchy, with FWHM equal to $2\mathcal{A} + \mathcal{B}$. (The DC part of the RCS spectrum, equal to $\alpha\delta(\omega)$ and reflecting merely the fact that the RCS has a constant non-zero mean value of α, has been removed.) A more precise alternative the inference of $\mathcal{A}$ is offered by Equation

[2]an ACF $R(\tau) = \exp(-\frac{1}{2}k|t|)$ has associated power spectrum $S(\omega) = 2k/\pi(k^2 + 4\omega^2)$ with full width at half maximum (FWHM) equal to k.

(2.35) in Field and Tough (2003b),

$$\frac{\mathrm{d}r_t^2}{\mathrm{d}t} = \frac{1}{2}\mathcal{A} \tag{4.27}$$

as the volatility of the population level square-root r_t. Since it requires an estimate of x_t, in practical situations, the wisest approach would be to combine both solutions through an iterative scheme.

TABLE 4.1: Discrepancy (in percentage) between the experimental and the theoretical Δ^{opt} over a range of parameters α and $\mathcal{A}$.

	$\alpha = 4$	$\alpha = 10$	$\alpha = 20$
$\mathcal{A} = 10^{-4}$	4.33 %	1.16 %	3.09 %
$\mathcal{A} = 10^{-3}$	1.83 %	1.79 %	2.94 %
$\mathcal{A} = 10^{-2}$	1.48 %	1.51 %	0.14 %

4.2.6 Extension for a generalized population

The results given in Section 4.2.1 for a K–scattered amplitude may be extended to a generalized population (i.e., instead of restricting the population model to (3.13), any process conforming to (3.12) may be accommodated). The actual derivation steps for a Gamma texture can readily incorporate a broader range of diffusion processes, as thoroughly described in Fayard and Field (2010a). Motivated by their importance for practical applications, we shall especially consider the class of Pearson diffusions described in Section 2.3.2. In effect, for a Pearson diffusion obeying (2.46), (4.12) becomes

$$\begin{aligned} x_{i+1} = (1 - \alpha\mathcal{A}\delta_t)\, x_i + \alpha\mathcal{A}\delta_t \\ + \left(2\mathcal{A}\delta_t\sigma_i\right)^{1/2} w_i \end{aligned} \tag{4.28}$$

where $w_i \sim \mathcal{N}(0,1)$. We know that the fluctuations of the RCS are negligible within the sampling window, that is, the dimensionless constant $\mathcal{A}\delta_t$ verifies $\mathcal{A}\delta_t \ll 1$. Therefore, it is reasonable to assume that $1-\mathcal{A}\delta_t \approx 1$; yielding a revised expression of (4.13)

$$\begin{aligned} x_{i+j} &= x_i + j\alpha\mathcal{A}\delta_t \\ &+\mathrm{sgn}(j)\sum_{k=1}^{|j|}(2\mathcal{A}\delta_t\sigma_{\mathrm{i+sg(j)k}})^{1/2}w_{\mathrm{i+sg(j)k}}. \end{aligned} \tag{4.29}$$

Apart from this difference, the derivation of ϵ_{sm} proceeds exactly like for the K–scattering case, yielding the following results

$$\epsilon_{\mathrm{sm}} = \frac{\mathcal{A}\delta_t\Delta}{6}\sum_{i=1}^{N}\mathbf{E}\left[\sigma_i\right] + \frac{2}{\Delta}\sum_{i=1}^{N}\mathbf{E}\left[x_i^2\right] \tag{4.30}$$

and

$$\Delta^{\mathrm{opt}} = \left(\frac{12\sum_{i=1}^{N}\mathbf{E}\left[x_i^2\right]}{\mathcal{A}\delta_t\sum_{i=1}^{N}\mathbf{E}\left[\sigma_i\right]}\right)^{1/2}. \tag{4.31}$$

Figs. 4.6(a),4.6(b),4.6(c), obtained from the same token as for a Gamma distributed texture, demonstrate the agreement between our analytical findings above and actual experimental results.

4.3 Scattered amplitude in additive noise

4.3.1 Additional thermal noise

Radar experimentalists have observed that radar clutters are in some cases better described as a K–scattered amplitude lying in an additional thermal noise (e.g., measurement noise) (Watts, 1981). A situation that might be described consistently with the stochastic framework given in Chapter 3 as follows. In the presence of an additional thermal noise, the observed scattered amplitude may be written (Fayard and

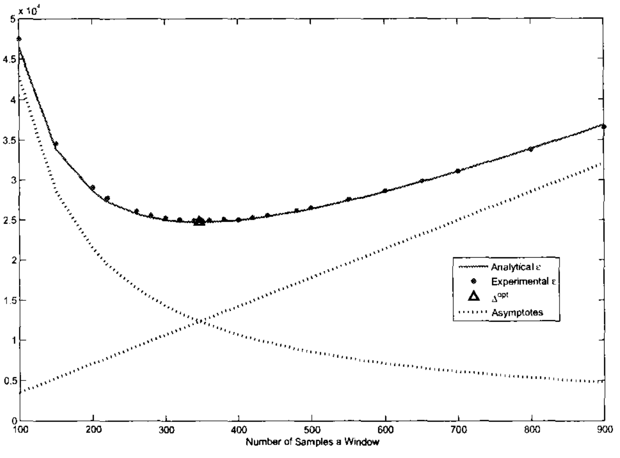

(a) inverse Gamma ($\alpha = 4$)

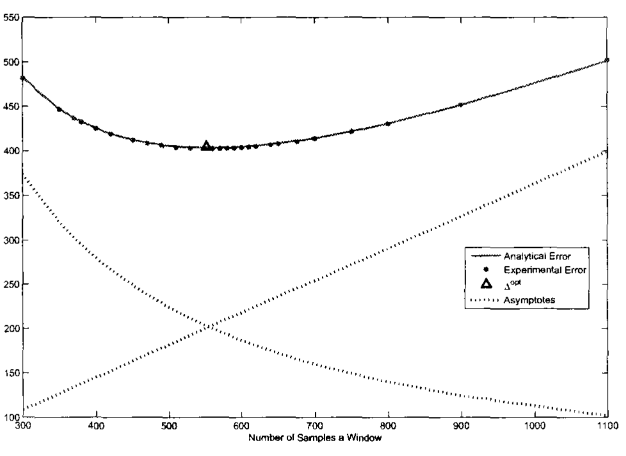

(b) Beta of the first kind ($q = 1.9$, $p = 1.5$, $\beta = 3.5$)

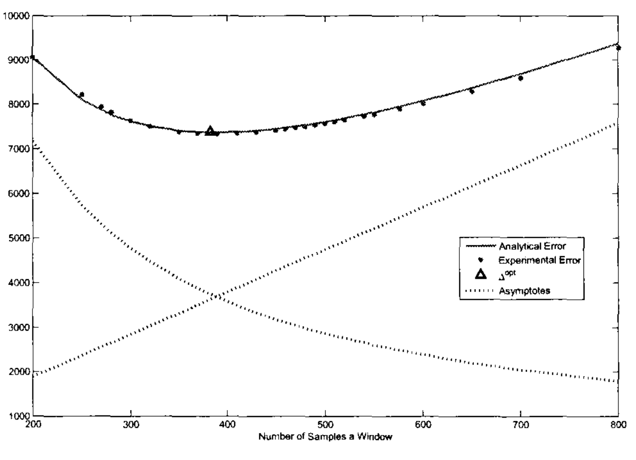

(c) Beta prime ($p = 1.2$, $q = 1.5$, $\beta = 2.5$)

FIGURE 4.6: Comparison of the analytical and experimental MSE deviation between the inferred and the exact cross-sections for three Pearson diffusions. (For

Field, 2010b)

$$\widetilde{\psi}_t = \psi_t + \Gamma_t \tag{4.32}$$

where $\widetilde{\psi}_t$ denotes the raw scattered amplitude and Γ_t the thermal noise, which is assumed to be independent of the (hidden) amplitude ψ_t. The relative power of the noise is characterized by a signal-to-noise ratio (SNR): SNR $= 10 \ \log_{10}(\langle\psi_t^2\rangle/\langle\Gamma_t^2\rangle)$. Equation (4.32) proposes a dynamical representation of the aforementioned model for a K–distributed sea clutter and thermal noise (cf. Watts (1981) or Ward et al. (2006)), which states that the probability density function for the intensity $\widetilde{z}_t = |\widetilde{\psi}_t|^2$ of the combined signal obeys[3]

$$P(\widetilde{z}|x) = \frac{1}{p_{\mathrm{n}} + x} \exp\left(-\frac{\widetilde{z}}{p_{\mathrm{n}} + x}\right) \tag{4.33}$$

where p_{n} denotes the thermal noise power. We readily observe that

$$\mathbb{E}[\widetilde{z}|x] = x + p_{\mathrm{n}}. \tag{4.34}$$

Alternatively, we may derive from (4.32) the following expression for the raw intensity mean

$$\mathbb{E}[\widetilde{z}|x] = \mathbb{E}[|\psi|^2|x] + \mathbb{E}[\psi^*\Gamma|x] + \mathbb{E}[\psi\Gamma^*|x] + \mathbb{E}[|\Gamma|^2|x] \tag{4.35}$$

where the cross-terms vanish since the (zero-mean) component Γ_t is independent of ψ_t. As a consequence of the compound representation (3.11), the first term reads $\mathbb{E}[|\psi|^2|x] = x$ (since γ has unit power) and (4.34) is recovered (for $\mathbb{E}[|\Gamma|^2|x] = p_{\mathrm{n}}$ is the thermal noise power). In other words, (4.32) asserts that the average power of the scattered intensity (which is nothing but the RCS) is effectively increased by the thermal noise power; a property characteristic of the clutter and noise model (4.33).

This supplementary thermal noise prohibits the direct use of Proposition 4.1. In order to exploit the information about the target contained in the sea clutter, it is necessary to remove this noisy component. Here comes one of the advantages of

[3] to be compared with (2.8) where the intensity has a negative exponential distribution

the stochastic description of the scattered amplitude. Since the spectral properties of the various processes are known (cf. Section 3.4), one can adopt the Wiener filter (Kamen and Su, 1984, Chap. 4) in its finite impulse response (FIR) form to retrieve the sea clutter. The use of a Wiener (as opposed to matched) filter is furthermore appropriate since the scattered intensity is inherently stochastic. The filter requires the processes involved to be jointly wide sense stationarity, a condition fulfilled by $\widetilde{\psi}_t$, as evidenced by (4.32).

4.3.2 Filtering out the thermal noise

4.3.2.1 Filter derivation

A FIR Wiener filter, of order N, posits an estimate of the form:

$$\widehat{\psi}(n) = \sum_{i=0}^{N-1} h(i)\widetilde{\psi}(n-i) \tag{4.36}$$

that means as the convolution between a filter function h and the noisy data history. The filter function h is chosen to minimize, in the sense of the MMSE criterion, the discrepancy between the underlying ψ_t and the estimated $\widehat{\psi}_t$ amplitudes. The lower bound of the MMSE is actually reached through the orthogonality principle (cf. Chap. 12 in Papoulis (1984)), written as

$$\mathbb{E}\left[\left(\psi(n) - \sum_{i=0}^{N-1} h(i)\widetilde{\psi}(n-i)\right)\widetilde{\psi}(n-j)\right] = 0, \quad \forall j \in \{0,\ldots,N-1\}. \tag{4.37}$$

Some forward derivations (cf. Kamen and Su, 1984) yield (for zero-mean processes) the following optimum linear time-invariant estimator,

$$\begin{pmatrix} h(0) \\ h(1) \\ \dots \\ h(N-1) \end{pmatrix} = \begin{pmatrix} R_{\widetilde{\psi}}(0) & \dots & R_{\widetilde{\psi}}(N-1) \\ R_{\widetilde{\psi}}(1) & \dots & R_{\widetilde{\psi}}(N-2) \\ \dots & \dots & \dots \\ R_{\widetilde{\psi}}(N-1) & \dots & R_{\widetilde{\psi}}(0) \end{pmatrix}^{-1} \times \begin{pmatrix} R_{\psi\widetilde{\psi}}(0) \\ R_{\psi\widetilde{\psi}}(1) \\ \dots \\ R_{\psi\widetilde{\psi}}(N-1) \end{pmatrix} \tag{4.38}$$

where $R_{\widetilde{\psi}}$ and $R_{\psi\widetilde{\psi}}$ represent, respectively, the autocorrelation of the noisy amplitude $\widetilde{\psi}_t$ and the correlation between $\widetilde{\psi}_t$ and the de-noised amplitude ψ_t . The filter weights are deduced from this system of N equations (Wiener–Hopf equations). For a white noise disturbance (i.e. $R_\Gamma(i) = N_0/2\ \delta(i)$), the system of equations (4.38) further simplifies since $R_{\widetilde{\psi}} = R_\psi + R_\Gamma$ and $R_{\widetilde{\psi}\psi} = R_\psi$, where R_ψ is given by (4.26). The same system of equations would apply if all we knew were the autocorrelation functions but not the full dynamics.

4.3.2.2 Non-causal solution

In the degenerate case where the population remains constant $x_t = \alpha$ (i.e., the frequency constant $\mathcal{A}$ tends to 0), due to Gauss identity

$$_2F_1(a, b, c, 1) = \frac{\Gamma(c)\Gamma(c-a-b)}{\Gamma(c-a)\Gamma(c-b)} \tag{4.39}$$

the amplitude ACF (3.42) reduces to

$$\langle \psi_t \psi_0^* \rangle = \alpha \exp\left(-\mathcal{B}|t|/2\right) \tag{4.40}$$

allowing us to derive an analytical expression of the impulse response. In effect, the continuous version of the Wiener filter (see Papoulis, 1984, Chap. 14) states that the non-causal transfer function satisfies (in frequency-domain) $H(f) = S_{\psi\tilde{\psi}}(f)/S_{\tilde{\psi}}(f)$, where $S(f)$ denotes the PSD. Then, the (computationally intensive) Wiener–Hopf system of equations becomes superfluous; $h(t)$ can be found directly as the inverse Fourier transform of $H(f)$,

$$h(t) = \frac{\alpha\mathcal{B}}{N_0\sqrt{2\alpha\mathcal{B}/N_0 + (\mathcal{B}/2)^2}} \exp\left(- \sqrt{2\alpha\mathcal{B}/N_0 + (\mathcal{B}/2)^2}\, |t|\right) \tag{4.41}$$

where $N_0/2$ was previously introduced for the white noise PSD. The impulse response (4.41) is non-causal, but for applications where there exists historical data, a non-causal Wiener filter is preferable. If we think of $\tau = (2\alpha\mathcal{B}/N_0 + (\mathcal{B}/2)^2)^{-1/2}$ as the exponential timescale, its dependence w.r.t. $\mathcal{B}$ determines the behaviour of the impulse response. If $\mathcal{B}$ is small, the transfer function observes a flat shape: the filtering process uses a wide history. On the other hand, for a large $\mathcal{B}$, $h(t)$ becomes spiky: only neighboring samples are used for any estimate.

4.3.2.3 Filtering error

It is also of interest to know how the noise level has been reduced by the Wiener filter. In effect, quantifying the error $\widetilde{\psi}_t = \psi_t - \widehat{\psi}_t$ allows to have some insight into the filter quality. If h satisfies the orthogonality principle, one can derive an analytical expression of the MSE (Kamen and Su, 1984):

$$\varepsilon = R_\psi(0) - \sum_{j=0}^{N-1} h(j) R_{\psi\tilde{\psi}}(j), \tag{4.42}$$

or consider the MSE error reduction in decibels (i.e., compare the estimate with the case where $\widehat{\psi} = \widetilde{\psi}_t$),

$$\begin{aligned} \text{reduction in MSE} &= 10\log_{10}\left(\frac{\varepsilon_{\text{nofilter}}}{\varepsilon_{\text{filter}}}\right) \\ &= 10\log_{10}\left(\frac{R_\psi(0) + R_{\tilde{\psi}}(0) - 2R_{\psi\tilde{\psi}}(0)}{R_\psi(0) - \sum_{j=0}^{N-1} h(j) R_{\psi\tilde{\psi}}(j)}\right) \end{aligned} \tag{4.43}$$

The above expression only depends on the processes' auto- and cross-correlations. Since the autocorrelation functions of the (zero-mean) processes ψ_t and Γ_t are, respectively, known from (3.42) and derivable (given the SNR) from the average power of ψ_t ($\mathbb{E}[|\psi_t|^2] = R_\psi(0) = \alpha$) the noise reduction (4.43) can be evaluated independently of the experiment.

4.3.3 Simulation

4.3.3.1 Filtering

To assess the filtering step efficiency we reconsider the experiment from Section 4.2.4 with the supplementary ingredient of a thermal noise Γ_t characterized by a particular SNR (in decibels) and adjoined to the K–scattered amplitude. The analytical expression for the ACF of the process $\widetilde{\psi}_t = \Gamma_t + \psi_t$ was used to solve numerically the Wiener–Hopf system of equation in order to find the weights of the filter impulse response h, as described in Sect. 4.3.2.1. The (positive-valued) intensities z_t for the hidden, raw and estimated signals are shown in Fig. 4.7 (see Fayard and Field, 2010b, Fig. 1). The noisy scattered amplitude is filtered to recover the original signal. In contrast to its noisy version, the filtered signal exhibits the geometric structures characteristic of the sea clutter. It can therefore be used for inferring the RCS.

Remark: The knowledge of the parameters α, $\mathcal{A}$ and $\mathcal{B}$ is a requisite for an analytical construction of the Wiener filter. Otherwise, i.e. for practical applications, the collected data ACF is sufficient to populate the elements in the right-hand side of (4.38). Since the processes involved are independent and Γ_t is zero-mean, the autocorrelation of the raw amplitude $\widetilde{\psi}_t$ will be given by $R_{\widetilde{\psi}}(\tau) = N_0/2\ \delta(\tau) + R_\psi(\tau)$ where $R_\psi(\tau)$ is the pure K–amplitude autocorrelation. A scheme to extract $\mathcal{A}$ from the scattered amplitude was given in Fayard and Field (2008). Since α is related to the usual parameter shape of the K–distribution, comparing the observed scattered amplitude with the nearest-fit theoretical K–distribution permits to deduce α. The sole unknown parameter is therefore $\mathcal{B}$, whose extraction from the filtered amplitude is described below.

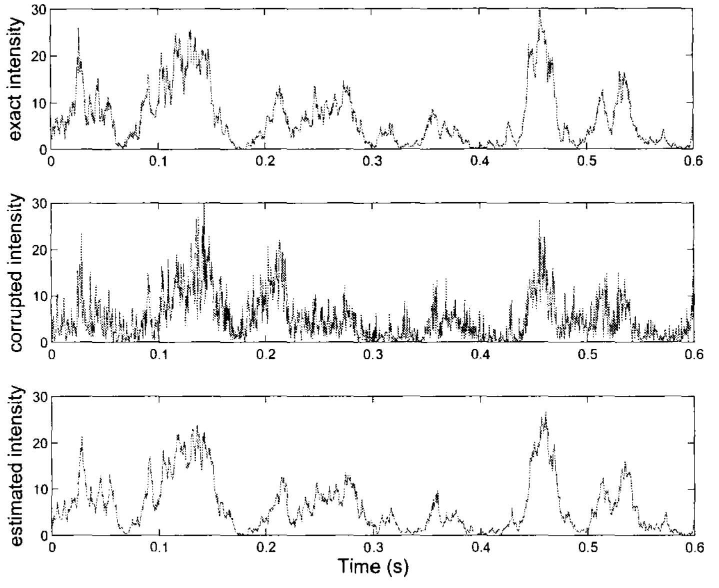

FIGURE 4.7: Shown, from top to bottom, are the scattered intensity z_t as the absolute value squared of the scattering amplitude for the exact ψ_t generated via the integration of (3.15), the raw $\widetilde{\psi}_t = \psi_t + \Gamma_t$ (i.e., a corrupted version of the underlying amplitude) and the filtered $\widehat{\psi}_t$ (obtained from the Wiener filter). (Parameter values $\alpha = 7, \mathcal{A} = 10^{-3}$, $\mathcal{B} = 10^{-2}$, $SNR = 10$ dB, $N = 50$.)

4.3.3.2 Parameter Estimation

In most practical situations, x_t will be constant over the fluctuations of γ_t since their time characteristics verify $\mathcal{B}^{-1} \ll \mathcal{A}^{-1}$. As discussed above, it is useful to estimate the parameter $\mathcal{B}$, characteristic of the speckle. Since γ_t is a mean reverting process with a $\exp(-\frac{1}{2}\mathcal{B}|t|)$ decay in the ACF, the intensity $z_t = |\gamma_t|^2 x_t$ will possess, for a cross-section roughly constant over the fluctuations of γ_t, a spacing of the order of $\mathcal{B}^{-1}$ between two consecutive peaks ($\mathcal{B}^{-1}$ being the characteristic correlation time). This is a direct consequence of the compound representation of the scattered amplitude, in terms of two processes that are statistically independent. As an interesting result of the filtering above, we can track the peaks of the (filtered) amplitude to deduce an estimate of $\mathcal{B}$. To do so, the Wiener filtering step is necessary since, otherwise, the amplitude peaks will be hidden within the surrounding noise Γ_t.

An algorithm for this task (requiring a rough value of $\mathcal{B}^{-1}$) will proceed as follows. We first localize the maximal peak of the intensity z_t over a window of length of order 10 $\mathcal{B}^{-1}$. We neutralize this peak and the neighboring samples located within a distance of about $\mathcal{B}^{-1}/10$. We now consider a secondary window (centered at the peak) of iterated length δ, starting with $\delta = \mathcal{B}^{-1}/10$, and extract its maximum value. At first, this maximum value will be positioned close to the former maximal peak, until it reaches (for a larger δ) the following amplitude peak (expected at an average distance of $\mathcal{B}^{-1}$). If we now plot the position of the δ-window's maximum w.r.t. the value of δ, the graph will exhibit a first discontinuity due to the passage from the original peak to the following one in the intensity pattern. The average size of this discontinuity is a reliable estimate of the time characteristic $\mathcal{B}^{-1}$.

We use the algorithm detailed above to estimate the parameter $\mathcal{B}$ from the filtered amplitude. Tab. 4.2 investigates the sensitivity of our algorithm to $\mathcal{A}$ and α, given the value of $\mathcal{B}$. The algorithm is only slightly altered by such changes. In the same vein, Tab. 4.3 verifies that the algorithm results are acceptable if the value of the parameter $\mathcal{B}$ or of the SNR change. These two tables therefore assert the robustness of our approach.

TABLE 4.2: Sensitivity of the parameter estimation algorithm to A and α. (For SNR = 20 dB and a true parameter value $B = 10^{-2}$.)

	$\mathcal{A} = 1e-5$	$\mathcal{A} = 5e-4$	$\mathcal{A} = 1e-4$	$\mathcal{A} = 5e-4$	$\mathcal{A} = 1e-3$
$\alpha = 2$	1.10e-2	1.04e-2	1.05e-2	1.03e-2	1.03e-2
$\alpha = 5$	1.08e-2	1.07e-2	1.02e-2	1.03e-2	1.00e-2
$\alpha = 10$	1.10e-2	1.06e-2	1.04e-2	1.01e-2	0.99e-2
$\alpha = 15$	1.06e-2	1.06e-2	1.06e-2	1.00e-2	1.00e-2
$\alpha = 20$	1.08e-2	1.08e-2	1.02e-2	1.02e-2	0.99e-2

TABLE 4.3: Sensitivity of the parameter estimation algorithm to $\mathcal{B}$ and to the SNR. (Parameters $\mathcal{A} = \mathcal{B}/10, \alpha = 10$.)

	$\mathcal{B} = 1e-2$	$\mathcal{B} = 5e-3$	$\mathcal{B} = 1e-3$	$\mathcal{B} = 5e-4$
SNR = 5 dB	1.04e-2	5.41e-3	1.08e-3	5.33e-4
SNR = 14 dB	1.03e-2	5.35e-3	1.12e-3	5.30e-4
SNR = 20 dB	1.05e-2	5.32e-3	1.11e-3	5.37e-4
SNR = 30 dB	1.08e-2	5.52e-3	1.09e-3	5.17e-4

4.3.3.3 Anomaly detection: additional white noise

The methodology described above is also of interest to observe the scattering cross-section through the phase de-coherence. A shortcoming of technique detailed in Section 4.1.3 is to assume that the *pure* K–distributed amplitude is available, which is not true for experimental data where an additional noise is present. Simulated data illustrate how this difficulty could be overcome. The synthetic population determined by (3.13) (on the bottom) is compared with the population extracted from the filtered amplitude $\widehat{\psi}_t$ (middle) and from the corrupted amplitude $\widetilde{\psi}_t$ (on the top), the latter two being obtained through the *modus operandi* detailed in Section 4.1.3. Fig. 4.8 shows the time series for the three different cross-sections, which have been re-scaled (the correlation coefficient being invariant for such an affine transformation). Consistently, we observe that the cross-section obtained through the filtered amplitude offers a faithful picture of the exact cross-section, whereas the cross-section obtained from the corrupted amplitude does not (as evidenced by their respective correlation coefficients with the exact RCS). An anomaly in the resulting time series for the RCS would indicate the presence of a target. Instead of, for example, de-correlating the speckle by frequency agility, applying successively the Wiener filter and the technique embodied by (4.1) enables a reasonably accurate extraction of the RCS from the raw amplitude $\widetilde{\psi}_t$.

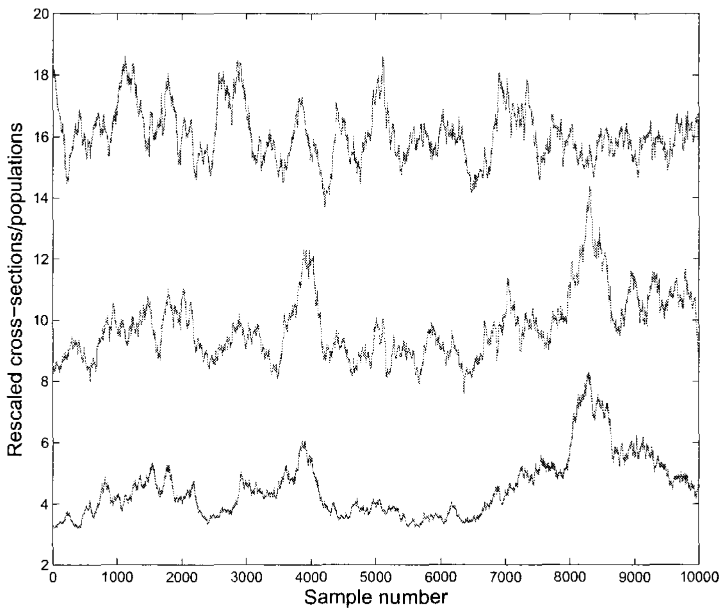

FIGURE 4.8: Comparison of the exact RCS (bottom) with the RCS inferred from the filtered amplitude (middle) and noisy amplitude (top). The latter two exhibit, respectively, a correlation coefficient of 0.83 and −0.08 with the exact RCS. (Parameter values $\alpha = 2$,$\mathcal{A} = 10^{-2}$, $\mathcal{B} = 10^{-1}$, $SNR = 15$.)

Chapter 5

Observability of the RCS for weak scattering

5.1 Volatility of a weakly scattered amplitude

5.1.1 Objective

We have described in Chapter 4 how the RCS was observable, for a strongly scattered amplitude, through the intensity-weighted squared fluctuations of the phase. This result motivates us to investigate whether a corresponding result holds for a weakly scattered amplitude. To answer this question, one should appreciate that the prominent difference between the two scattering patterns lies in the geometry of the scattered amplitude diffusion tensor. Whereas angular and radial fluctuations de-correlate for a strongly scattered amplitude, this is no longer the case for a weakly scattered amplitude, owing to the presence of a coherent offset in (3.30). Nevertheless, the structure of the weakly scattered amplitude cross-volatility conveys information about the RCS if we introduce an orthogonal dyad w.r.t. which the resultant amplitude fluctuations de-correlate.

5.1.2 Decomposition of the amplitude fluctuations

Motivated by the representation of the strongly scattered amplitude ψ_t in terms of two independent processes, the cross-section and the speckle, let us follow a similar token to decompose the weakly scattered amplitude fluctuations into terms originating in x_t and γ_t. As we are only concerned with the processes' volatility, we may combine drift terms in the Ito differentials for the phase Θ_t (3.39) and intensity Z_t (3.40) as $o(\mathrm{d}t^{1/2})$. Hence, we obtain the following expression for the (intensity-weighted) phase $2Z_t\mathrm{d}\Theta_t$ and intensity $\mathrm{d}Z_t$ differentials

$$2Z_t\mathrm{d}\Theta_t = 2\Im\left[\Psi_t^*\mathrm{d}\Psi_t\right] + o(\mathrm{d}t^{1/2}) \tag{5.1}$$

$$\mathrm{d}Z_t = 2\Re\left[\Psi_t^*\mathrm{d}\Psi_t\right] + o(\mathrm{d}t^{1/2}). \tag{5.2}$$

The parallelism between (5.1) and (5.2) shall facilitate subsequent derivations. The Ito differential of the weakly scattered amplitude may be expressed along the same lines as

$$\mathrm{d}\Psi_t = (\mathcal{B}x_t)^{1/2}\mathrm{d}\xi_t + \gamma_t\left(\frac{\mathcal{A}\sigma_t}{2x_t}\right)^{1/2}\mathrm{d}W_t^{(x)} + e_t'(2\mathcal{A}\sigma_t)^{1/2}\mathrm{d}W_t^{(x)} + o(\mathrm{d}t^{1/2}) \tag{5.3}$$

where we have combined the drift terms in (3.37) as $o(\mathrm{d}t^{1/2})$. If we substitute (5.3) in (5.1) and (5.2), we obtain the following decomposition for the phase and intensity differentials

$$2Z_t\mathrm{d}\Theta_t = 2\left(\mathcal{B}x_t\right)^{1/2}\Im\left[\Psi_t^*\mathrm{d}\xi_t\right] + (2\mathcal{A}\sigma_t)^{\frac{1}{2}}f_t^{(\Theta)}\mathrm{d}W_t^{(x)} + o(\mathrm{d}t^{1/2}) \tag{5.4}$$

$$\mathrm{d}Z_t = 2\left(\mathcal{B}x_t\right)^{1/2}\Re\left[\Psi_t^*\mathrm{d}\xi_t\right] + (2\mathcal{A}\sigma_t)^{\frac{1}{2}}f_t^{(Z)}\mathrm{d}W_t^{(x)} + o(\mathrm{d}t^{1/2}) \tag{5.5}$$

where we have introduced

$$f_t^{(\Theta)} = \Im\left[\Psi_t^*\left(\frac{\psi_t}{x_t} + 2e_t'\right)\right] \tag{5.6}$$

$$f_t^{(Z)} = \Re\left[\Psi_t^*\left(\frac{\psi_t}{x_t} + 2e_t'\right)\right]. \tag{5.7}$$

The coupled equations (5.4) and (5.5) have important characteristics. First, they tell us that the differentials of Θ_t and Z_t are, respectively, the imaginary and real parts of the same quantity- prompting parallel derivations. Next, they yield explicitly the two Brownian terms influencing the phase and the intensity fluctuations. In this respect, both the intensity and phase fluctuations contain terms arising from the speckle (proportional to $\mathrm{d}\xi_t$) and from the scattering cross-section (proportional to $\mathrm{d}W_t^{(x)}$), which have respective timescales $\mathcal{B}^{-1}$ and $\mathcal{A}^{-1}$. A last observation is that the cross-volatility is only induced by the fluctuations originating in the cross-section

$$\Sigma_t^{(Z,\Theta)} = \frac{\mathcal{A}\sigma f_t^{(Z)} f_t^{(\Theta)}}{Z_t}. \tag{5.8}$$

since $\mathrm{d}\xi_t$ is a complex valued Wiener process orthogonal to $\mathrm{d}W_t^{(x)}$ and satisfies $\mathrm{d}\xi_t^2 = 0$.

Equation (5.8) explains why the radial and angular fluctuations of a weakly scattered amplitude do not de-correlate. Upon considering the cross-product of (5.4) and (5.5), cross-terms vanish as $\mathrm{d}\xi_t$ and $\mathrm{d}W_t^{(x)}$ are independent, the terms originating in the speckle also vanish as $\mathrm{d}\xi_t$ is a complex Wiener process so that only the terms driven by $\mathrm{d}W_t^{(x)}$ are left. Thus, phase and intensity differentials are correlated through the product $f_t^{(Z)} f_t^{(\Theta)}$. On the other hand, in the strong scattering situation, the expression $\Psi_t^*(2e_t' + \psi_t/x_t)$ that features in the right-hand sides of (5.6) and (5.7) reduces to (the purely real) z_t/x_t, yielding $f_t^{(\Theta)} = 0$, that is, the angular and radial fluctuations de-correlate. Also, we observe from the squares of (5.4) and (5.5) that

$$4Z_t^2\mathrm{d}\Theta_t^2 = 2\mathcal{B}Z_t x_t \mathrm{d}t + (2\mathcal{A}\sigma_t)\, f_t^{(\Theta)2}\mathrm{d}t \tag{5.9}$$

$$\mathrm{d}Z_t^2 = 2\mathcal{B}Z_t x_t \mathrm{d}t + (2\mathcal{A}\sigma_t)\, f_t^{(Z)2}\mathrm{d}t. \tag{5.10}$$

If we consider the quantity

$$2\frac{(5.10)\times(5.9)}{(5.10)^2-(5.9)^2}, \tag{5.11}$$

we notice that the state processes $f_t^{(\Theta)}$ and $f_t^{(Z)}$ satisfy

$$\frac{4Z_t\Sigma_t^{(Z,\Theta)}}{\Sigma_t^{(Z)} - 4Z_t^2\Sigma_t^{(\Theta)}} = \frac{2f_t^{(\Theta)} f_t^{(Z)}}{f_t^{(Z)2} - f_t^{(\Theta)2}}. \tag{5.12}$$

5.1.3 Scattering vector

5.1.3.1 Proposition

A set of SDEs pertaining to the dynamics of the weakly scattered phase and intensity are readily derived from (3.39) and (3.40). They are conveniently represented with the dynamical characterization of the vector scattering process $S_t = (x_t, Z_t, \Theta_t)^{\mathrm{tr}}$ (see Chap. 3 in Field (2009), for a detailed exposition of the underlying stochastic differential geometry)

$$\mathrm{d}S_t^i = b_t^i \mathrm{d}t + \sigma_t^i \mathrm{d}W_t^i \tag{5.13}$$

(no summation over i) for a collection of Wiener processes $\{W_t^i | \forall i\}$ (not necessarily independent) with respective drift and diffusion coefficients b^i, Σ^{ij} determined by

$$\begin{aligned} b_t^i &= \frac{\langle \mathrm{d}S_t^i \rangle_t}{\mathrm{d}t}, \\ \mathrm{d}S_t^i \mathrm{d}S_t^j &= \Sigma_t^{ij} \mathrm{d}t \end{aligned} \tag{5.14}$$

where $\langle \cdot \rangle_t$ denotes the conditional expectation up to and including time t. For the Markov diffusions that arise here, $\langle \cdot \rangle_t$ can be considered as the expectation conditional on the state of the system at time t. Although it is easier to consider separately Rice, HK and GK amplitudes (as proposed in Field and Tough (2005)), it is more instructive to derive such expressions for an arbitrary offset e_t.

Proposition 5.1. *For an arbitrary weakly scattered amplitude $\Psi_t = e_t + \psi_t$, the drift and diffusion coefficients of the scattering vector are given by*

$$b^i = \begin{pmatrix} \mathcal{A}b \\ \\ \mathcal{A}\left[Z\left(\frac{b}{x} - \frac{\sigma}{2x}\right) - 2Z^{\frac{1}{2}}\cos\Theta\left(e\frac{b}{2x} - e\frac{\sigma}{4x^2} - e'b - e''\sigma\right)\right] \\ +\mathcal{B}\left[x - Z + eZ^{\frac{1}{2}}\cos\Theta\right] + \frac{1}{2}\mathcal{A}\sigma\left(f^{(Z)2} + f^{(\Theta)2}\right)/Z \\ \\ \sin\Theta\left[\mathcal{A}\left(\frac{b}{2x} - \frac{\sigma}{4x^2} - e'b - e''\sigma\right) - \frac{1}{2}\mathcal{B}e\right]/Z^{\frac{1}{2}} - f^{(Z)}f^{(\Theta)}/Z^2 \end{pmatrix} \tag{5.15}$$

and

$$\Sigma^{ij} = \begin{pmatrix} 2\mathcal{A}\sigma & 2\mathcal{A}\sigma f^{(Z)} & 2\mathcal{A}\sigma f^{(\Theta)} \\ \dots & 2\mathcal{B}xZ + 2\mathcal{A}\sigma f^{(Z)2} & \mathcal{A}\sigma f^{(Z)}f^{(\Theta)}/Z \\ \dots & \dots & \frac{1}{2}\left(\mathcal{A}\sigma f^{(\Theta)2} + \mathcal{B}xZ\right)/Z^2 \end{pmatrix}. \tag{5.16}$$

The expressions for the HK and GK cases given in Field and Tough (2005) for a Gamma texture (2.40) are recovered for $e_t = a$ and $e_t = ax_t$, respectively.

The tensors (5.15) and (5.16), originally derived in Fayard and Field (2011), have been abbreviated with the functions $f_t^{(\Theta)}$ and $f_t^{(Z)}$ whose definitions in (5.6) and (5.7) yield the formulae

$$f_t^{(\Theta)} = \frac{Z_t^{\frac{1}{2}}\sin\Theta_t\left(e_t - 2e_t'x\right)}{x} \tag{5.17}$$

$$f_t^{(Z)} = \frac{1}{x}\left[Z + Z^{\frac{1}{2}}\cos\Theta(2e_t'x_t - e_t)\right]. \tag{5.18}$$

5.1.3.2 Proof

Proof. the volatility tensor Σ^{ij} (5.16) is embodied in the coupled equations (5.4) and (5.5). The drift coefficients proceed as follows.

The phase differential $\mathrm{d}\Theta_t$ defined by (3.40) is recast as

$$
\begin{aligned}
\mathrm{d}\Theta_t &= \frac{1}{i2Z}\left[\Psi^*\mathrm{d}\Psi - \Psi\mathrm{d}\Psi^*\right] - \frac{1}{4Zi}\left[\Psi^{*2}\mathrm{d}\Psi^2 - \Psi^2\mathrm{d}\Psi^{*2}\right] + o(\mathrm{d}t^{1/2}) \\
\mathrm{d}\Theta_t &= \frac{1}{i2Z}\left[(\psi^* + e)(\mathrm{d}\psi + \mathrm{d}e) - (\psi + e)(\mathrm{d}\psi^* + \mathrm{d}e)\right] \\
&\quad -\frac{1}{4Zi}\Big[\Psi^{*2}(\mathrm{d}\psi^2 + 2\mathrm{d}\psi\mathrm{d}e + \mathrm{d}e^2) - \Psi^2(\mathrm{d}\psi^{*2} + 2\mathrm{d}\psi^*\mathrm{d}e + \mathrm{d}e^2)\Big] + o(\mathrm{d}t^{1/2})
\end{aligned}
$$

The first term in the right-hand side of the above equation only involves the drift terms of the amplitude differential $\mathrm{d}\Psi_t$ from (3.38). The second term is rewritten by making use of the following Ito products

$$
\mathrm{d}e^2 = \mathcal{A}\sigma e'\mathrm{d}t \qquad \mathrm{d}e\mathrm{d}\psi = \mathcal{A}e'\tfrac{\sigma}{x}\psi\mathrm{d}t \qquad \mathrm{d}\psi^2 = \mathcal{A}\frac{\sigma}{2x^2}\psi^2.
$$

Accordingly, we obtain

$$
\begin{aligned}
\mathrm{d}\Theta_t &= \frac{1}{i2Z}\Bigg[(\psi^* + e)\bigg(e'\mathcal{A}\sigma + e''\mathcal{A}\sigma + \psi\Big[\mathcal{A}\big(\frac{b}{2x} - \frac{\sigma}{4x^2} - \frac{1}{2}\mathcal{B}\big)\Big]\bigg) \\
&\quad -(\psi + e)\bigg(e'\mathcal{A}\sigma + e''\mathcal{A}\sigma + \psi^*\Big[\mathcal{A}\big(\frac{b}{2x} - \frac{\sigma}{4x^2} - \frac{1}{2}\mathcal{B}\big)\Big]\bigg)\Bigg]\mathrm{d}t \\
&\quad -\frac{1}{4Zi}\Big[\Psi^{*2}\big(\frac{\psi^2}{x^2} + \frac{4e'\psi}{x} + 4e'^2\big) - \Psi^2\big(\frac{\psi^{*2}}{x^2} + \frac{4e'\psi^*}{x} + 4e'^2\big)\Big]\mathrm{d}t + o(\mathrm{d}t^{1/2}) \\
\mathrm{d}\Theta_t &= \frac{\psi - \psi^*}{2iZ}\left[\mathcal{A}\left(e'b + e''\sigma\right) + \mathcal{A}\left(\frac{eb}{2x} - \frac{e\sigma}{4x^2}\right) - \frac{1}{2}e\mathcal{B}\right]\mathrm{d}t \\
&\quad -\frac{\mathcal{A}\sigma}{2Z^2}\left(\frac{\Psi^*\left(\frac{\psi}{x} + 2e'\right) - \Psi\left(\frac{\psi^*}{x} + 2e'\right)}{2i}\right)\left(\frac{\Psi^*\left(\frac{\psi}{x} + 2e'\right) - \Psi\left(\frac{\psi^*}{x} + 2e'\right)}{2i}\right)\mathrm{d}t + o(\mathrm{d}t^{1/2})
\end{aligned}
$$

from which the second row in (5.15) is recovered.

For the intensity differential, our starting point is (3.39) in which we substitute (3.38) for the weakly scattered amplitude differential $\mathrm{d}\Psi_t$

$$\begin{aligned} \mathrm{d}Z &= (e+\psi^*)\left(\mathcal{A}\left[e'b+e''\sigma\right]+\psi\left[\mathcal{A}\left(\frac{b}{2x}-\frac{\sigma}{4x^2}\right)\right]\right) \\ &\quad +(e+\psi)\left(\mathcal{A}\left[e'b+e''\sigma\right]+\psi^*\left[\mathcal{A}\left(\frac{b}{2x}-\frac{\sigma}{4x^2}\right)\right]\right) \\ &\quad +\left(\mathrm{d}\psi\mathrm{d}\psi^*+\mathrm{d}\psi\mathrm{d}e+\mathrm{d}\psi^*\mathrm{d}e+\mathrm{d}e^2\right)+o(\mathrm{d}t^{1/2}) \end{aligned}$$

$$\begin{aligned} \mathrm{d}Z &= \mathcal{A}\left(\Psi^*+\Psi\right)\left(e'b+e''\sigma\right)\mathrm{d}t+ \\ &\quad e(\psi^*+\psi)\left[\mathcal{A}\left(\frac{b}{2x}-\frac{\sigma}{4x^2}\right)-\frac{1}{2}\mathcal{B}\right]\mathrm{d}t+2z\left[\mathcal{A}\left(\frac{b}{2x}-\frac{\sigma}{4x^2}\right)-\frac{1}{2}\mathcal{B}\right]\mathrm{d}t \\ &\quad +\left[x\mathcal{B}+\mathcal{A}\sigma\left(\frac{\psi\psi^*}{2x^2}+e'\frac{\sigma}{x}(\psi+\psi^*)+2e'^2\right)\right]\mathrm{d}t+o(\mathrm{d}t^{1/2}) \end{aligned}$$

$$\begin{aligned} \mathrm{d}Z &= \left(2\mathcal{A}Z^{1/2}\cos\Theta\left(e'b+e''\sigma\right)+e2z^{1/2}\cos\theta\right)\left[\mathcal{A}\left(\frac{b}{2x}-\frac{\sigma}{4x^2}\right)-\frac{1}{2}\mathcal{B}\right]\mathrm{d}t \\ &\quad +2z\left[\mathcal{A}\left(\frac{b}{2x}-\frac{\sigma}{4x^2}\right)-\frac{1}{2}\mathcal{B}\right]\mathrm{d}t+\mathcal{B}x\mathrm{d}t+ \\ &\quad \mathcal{A}\sigma\frac{1}{2Z}\left[\Psi\left(\frac{\psi^*}{2}+2e'\right)\right]\left[\Psi^*\left(\frac{\psi}{2}+2e'\right)\right]\mathrm{d}t+o(\mathrm{d}t^{1/2}). \end{aligned}$$

This last expression is not satisfactory since $\mathrm{d}Z_t$ is expressed in terms of the strong scattering phase θ_t and amplitude ψ_t. In order to express the drift coefficient solely in terms of weak scattering quantities, we shall use the following formulae

$$Z^{1/2}\cos\Theta = z^{1/2}\cos\theta+e \qquad Z=z+2ez^{1/2}\cos\theta+e^2$$

whence the second row of (5.15) is recovered. □

5.1.4 Geometry of amplitude fluctuations

We have proposed in Section 5.1.3 a detailed description of the dynamics of a weak scattered amplitude Ψ_t which are fully characterized by its drift (5.15) and volatility

(5.16) tensors. Some insight into the correlation structure of the amplitude fluctuations may be gained as follows. Combining drift terms as $o(\mathrm{d}t)^{1/2}$, we write the amplitude stochastic differential as

$$\begin{aligned} \mathrm{d}\Psi_t &= iR_t \exp(i\Theta_t)\mathrm{d}\Theta_t + \exp(i\Theta_t)\mathrm{d}R_t + o(\mathrm{d}^{1/2}) && (5.19)\\ &= \alpha_t \exp[i(\Theta_t + \phi_t)] + i\beta_t \exp[i(\Theta_t + \phi_t)] + o(\mathrm{d}^{1/2}), && (5.20) \end{aligned}$$

where α_t, β_t are real-valued Ito differentials and ϕ_t is chosen so that their Ito product $\alpha_t\beta_t$ vanishes, i.e., the Wiener components of α_t, β_t are statistically independent (see, e.g., Karatzas and Shreve, 1988). The point of interest here is the correlation structure in the amplitude fluctuations. In the strong scattering case, the radial and angular fluctuations are statistically independent. For a weakly scattered amplitude the amplitude fluctuations de-correlate w.r.t. the orthogonal dyad rotated by angle ϕ_t from that defined by the instantaneous radial and angular directions, as shown in Fig. 5.1 (cf. Fig. 1 in Field and Tough (2005)). In the newly defined basis $\{\alpha_t, \beta_t\}$, the projected angular and radial fluctuations of the scattered amplitude read

$$\begin{aligned} \mathrm{d}R_t &= \alpha_t \cos\phi_t - \beta_t \sin\phi_t && (5.21)\\ R_t\mathrm{d}\Theta_t &= \alpha_t \sin\phi_t + \beta_t \cos\phi_t && (5.22) \end{aligned}$$

where drift terms of order $(\mathrm{d}t^{1/2})$ have been neglected. Even though it is not possible to derive an exact expression for α_t, β_t, one may verify that their volatility coefficients satisfy (cf. Field and Tough, 2005)

$$\begin{aligned} \Sigma_t^{(\alpha)} &= \frac{1}{2}\left[\Sigma_t^{(\Psi,\Psi^*)} \pm \sqrt{\Sigma_t^{(\Psi)}\Sigma_t^{(\Psi^*)}}\right] && (5.23)\\ \Sigma_t^{(\beta)} &= \frac{1}{2}\left[\Sigma_t^{(\Psi,\Psi^*)} \mp \sqrt{\Sigma_t^{(\Psi)}\Sigma_t^{(\Psi^*)}}\right] && (5.24) \end{aligned}$$

which posses the expected symmetry $\alpha_t \to \beta_t$. Another result from Field and Tough (2005) reads

Proposition 5.2. *The phase rotation ϕ_t that yields an orthogonal dyad (cf. 5.1) associated with independent Wiener increments in the resultant amplitude process Ψ_t*

satisfies the geometrical identity

$$\tan 2\phi_t = \frac{4Z_t\Sigma_t(Z,\Theta)}{\Sigma_t^{(Z)} - 4Z_t^2\Sigma_t^{(\Theta)}}. \tag{5.25}$$

Equivalently, in terms of the resultant amplitude process, we have the geometrical identity

$$\tan 2\phi_t = -\frac{\Im\left[\Psi_t^2 \mathrm{d}\Psi_t^{*2}\right]}{\Re\left[\Psi_t^2 \mathrm{d}\Psi_t^{*2}\right]}. \tag{5.26}$$

Thus, the right-hand side of (5.25) may be expressed in the natural basis rotated by ϕ_t (5.25) as well as the radial/angular basis as (5.12). A direct comparison between the two yields the following expression for $\tan\phi_t$

$$\tan\phi_t = \frac{f_t^{(\Theta)}}{f_t^{(Z)}}, \tag{5.27}$$

where we have made use of the trigonometric identity $\tan 2a = 2\tan a/(1-\tan^2 a)$. Interestingly, ϕ_t is observable from the scattered amplitude through (5.25) (as a function of volatilities) but not from (5.27) since the expressions for $f_t^{(\Theta)}$, $f_t^{(Z)}$ involve the hidden state x_t in (5.17) and (5.18), respectively.

For a GK amplitude, we may understand Proposition 5.2 as follows. In this case, the coherent offset has intrinsic fluctuations (i.e., the boundaries ∂D and $\partial D'$ fluctuate in time). Substituting the volatility coefficients of a GK amplitude $e_t = ax_t$ from (5.16) into (5.26) yields, after a straightforward trigonometric identity

$$\tan\phi_t = -\frac{ax_t\sin\Theta_t}{Z_t^{1/2} + ax_t\cos\Theta_t} \tag{5.28}$$

(and minus the reciprocal). The above tangent corresponds to an axis of $\mathcal{S}^{\mathrm{GK}}$ along $R'P$ (as seen, e.g., by drawing a perpendicular from R' to the continuation in Fig. 5.1 of OP). The symmetry axes of the error surface $\mathcal{S}^{\mathrm{GK}}$ of the resultant amplitude are no longer aligned to those of the underlying K–amplitude - as opposed to the HK case (Field and Tough, 2005).

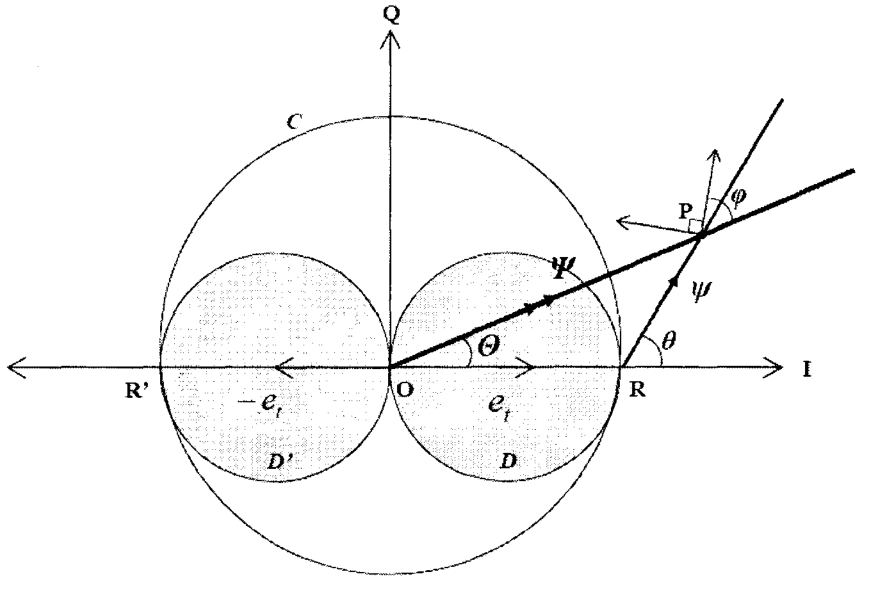

FIGURE 5.1: Geometry of fluctuations for the weak scattering process depicting orthogonal dyad w.r.t. which resultant amplitude fluctuations de-correlate.

5.2 Geometrical inference of the RCS

We have discussed in Section 4.1.2 how the RCS was observable, for a strongly scattered amplitude, through the intensity-weighted squared fluctuations of the phase. Interestingly, an equivalent set of results, based on the geometry described in Section 5.1.4, may be derived for a weakly scattered amplitude.

5.2.1 Phase fluctuations

If we write

$$f_t^{(\Theta)^2} = \left(f_t^{(\Theta)} f_t^{(Z)}\right)\left(\frac{f_t^{(\Theta)}}{f_t^{(Z)}}\right), \tag{5.29}$$

the second term in the right-hand side of (5.9) featuring $f_t^{(\Theta)2}$ is found to be determined by

$$\mathcal{A}\sigma f_t^{(\Theta)2} = Z_t \Sigma_t^{(Z,\Theta)} \tan\phi_t, \tag{5.30}$$

where we have taken advantage of the expressions for the radial-angular cross-volatility $\Sigma_t^{(Z,\Theta)}$ (5.8) and for $\tan\phi_t$ (5.27). Upon the substitution of (5.30) in (5.9), we obtain the following equation

$$4Z_t^2 \mathrm{d}\Theta_t^2 = 2\mathcal{B} Z_t x_t \mathrm{d}t + 2Z_t \Sigma_t^{(Z,\Theta)} \tan\phi_t., \tag{5.31}$$

where the first term in the right-hand side is a linear function of our quantity of interest, the RCS x_t. After rearranging the various terms we obtain the following proposition (Fayard and Field, 2011).

Proposition 5.3. *The instantaneous values of the scattering cross-section are observable through the intensity-weighted squared phase fluctuations, minus the intensity-phase cross-volatility weighted by the tangent of the dyad angle ϕ_t*

$$x_t = \frac{1}{\mathcal{B}} \left[2Z_t \Sigma_t^{(\Theta)} - \Sigma_t^{(Z,\Theta)} \tan\phi_t \right] \tag{5.32}$$

if x_t is an Ito process, not necessarily a diffusion, and throughout space and time.

Echoing the formula obtained for strong scattering (4.1), we observe that the RCS x_t is expressed in terms of quadratic variations (which are positive for Ito processes) and that the estimated state is known up to proportionality.

5.2.2 Intensity fluctuations

The similitude between the phase and intensity differentials (5.1) and (5.2) suggests that a result analogous to Proposition 5.3 but in terms of the intensity fluctuations may exist. Indeed, after taking the square of (5.5), we get

$$\mathrm{d}Z_t^2 = 2\mathcal{B} Z_t x_t \mathrm{d}t + 2\mathcal{A} f_t^{(Z)^2} \mathrm{d}t. \tag{5.33}$$

where the first term in the right-hand side is a linear function of the state x_t. We then write

$$f_t^{(Z)^2} = \left(f_t^{(\Theta)} f_t^{(Z)}\right)\left(\frac{f_t^{(Z)}}{f_t^{(\Theta)}}\right). \tag{5.34}$$

We can substitute in (5.33) an expression for $f_t^{(Z)}$ obtained from (5.8) and (5.27)

$$\mathrm{d}Z_t^2 = 2\mathcal{B}Z_t x_t \mathrm{d}t + \frac{2Z_t\Sigma_t^{(Z,\Theta)}}{\tan\phi_t} \tag{5.35}$$

which yields the following result where the RCS is expressed in terms of the intensity fluctuations - *in lieu of* the phase fluctuations as in Proposition 5.3 (*orig.* Fayard and Field, 2011).

Proposition 5.4. *The instantaneous values of the scattering cross-section are observable through the reciprocal intensity-weighted squared intensity fluctuations, minus the intensity-phase cross-volatility weighted by the reciprocal of the tangent of the dyad angle* ϕ_t

$$x_t = \frac{1}{\mathcal{B}}\left[\frac{\Sigma_t^{(Z)}}{2Z_t} - \frac{\Sigma_t^{(Z,\Theta)}}{\tan\phi_t}\right] \tag{5.36}$$

if x_t *is an Ito process, not necessarily a diffusion, and throughout space and time.*

5.3 Experimental implications

The practical consequences of Props. 5.3 and 5.4 are conveniently illustrated through synthetically generated data. In effect, and as opposed to experimentally collected data, this enables a comparison of the inferred cross-section obtained through the geometrical features of the scattered amplitude with the hidden state known from the simulation. These results are illustrated with a few distinct scattering situations. In both cases, the appropriate weakly scattered amplitude is generated through the numerical integration of (3.15) to which the appropriate coherence offset is adjoined as in (3.30). The amplitude ψ_t is more conveniently generated through the (independent) integration of the speckle (3.7) and the texture (3.12) SDEs by the Euler–Mayamura method (cf. Section 3.5 or Higham (2001)).

5.3.1 Phase fluctuations

For discretely sampled data, Proposition 5.3 yields the following estimate for the state

$$Z_i \delta\Theta_i^2 - \frac{1}{2}\delta Z_i \delta\Theta_i \left(\tan\phi_i\right) \propto x_i n_i^2 \tag{5.37}$$

where i is a discrete time index and $\{n_i\}$ are an independent collection of $\mathcal{N}(0,1)$ distributed random variables. Applying a smoothing average $\langle . \rangle_{\mathbf{\Delta}}$ to the left-hand side (the observations) of (5.37) with window $\mathbf{\Delta} = [t_0 - \Delta\delta_t, t_0 + \Delta\delta_t]$, where δ_t and Δ are respectively the sampling interval and the number of samples within a sampling window, yields an approximation to x_{t_0} with an error that tends to zero as the number of pulses inside $\mathbf{\Delta}$ tends to infinity and $\Delta \to 0$.

We then consider a homodyned weakly scattered amplitude (i.e., a constant coherent offset) for a Gamma distributed texture (which has respective drift and volatility coefficients $b = \alpha - x$ and $\sigma = x$). An estimate of the state is obtained through the smoothing of (5.37). Fig. 5.2 compares the cross-section obtained through the phase fluctuations (red solid) with the exact cross-section known from the simulation (black dotted), exhibiting a statistical correlation between the two of 0.9927.

Our second simulation example takes a generalized weakly scattered amplitude for an inverse Gamma distributed texture (cf. Section 2.3.1.2), that is $b = (\alpha - 1)(\alpha - x)$ and $\sigma = x^2$. The inferred RCS is also a close match of the exact RCS (as evidenced from Fig. 5.3 with a correlation coefficient of 0.9912.

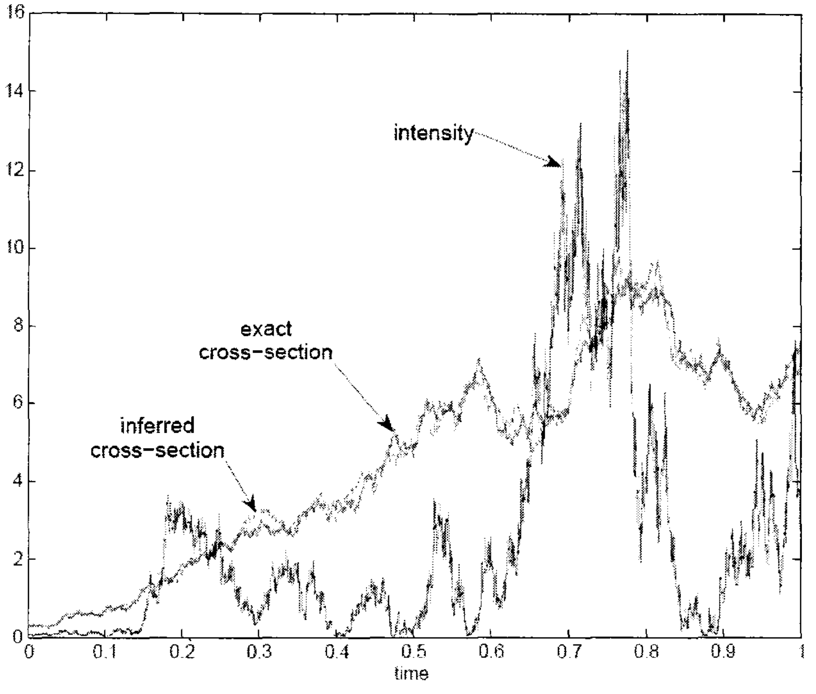

FIGURE 5.2: RCS inferred from a homodyned weakly scattered amplitude with a Gamma texture through the phase fluctuations Prop. 5.3. (For parameter values $\alpha = 5$, $\mathcal{A} = 10^{-3}$, $\mathcal{B} = 10^{-2}$, $\delta_t = 0.025$.)

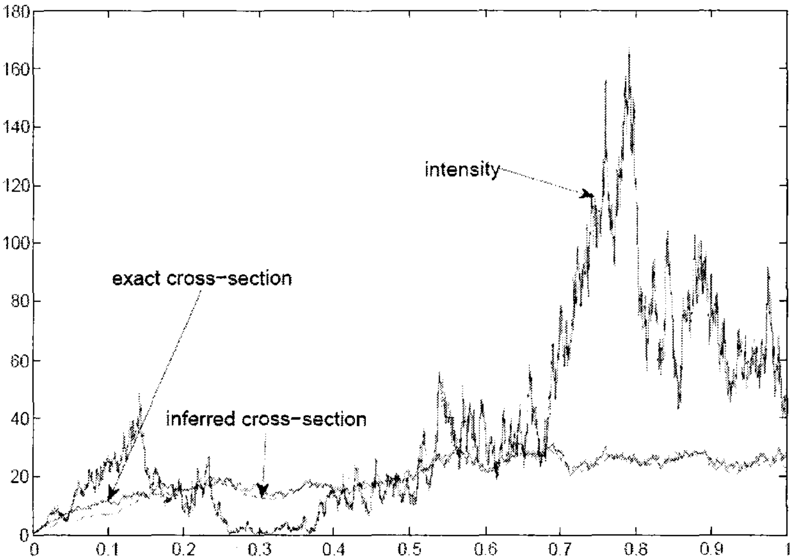

FIGURE 5.3: RCS inferred from a generalized weakly scattered amplitude with an inverse Gamma texture through the phase fluctuations Prop. 5.3. (For parameter values $\alpha = 5$, $\mathcal{A} = 10^{-3}$, $\mathcal{B} = 10^{-2}$, $\delta_t = 0.025$.)

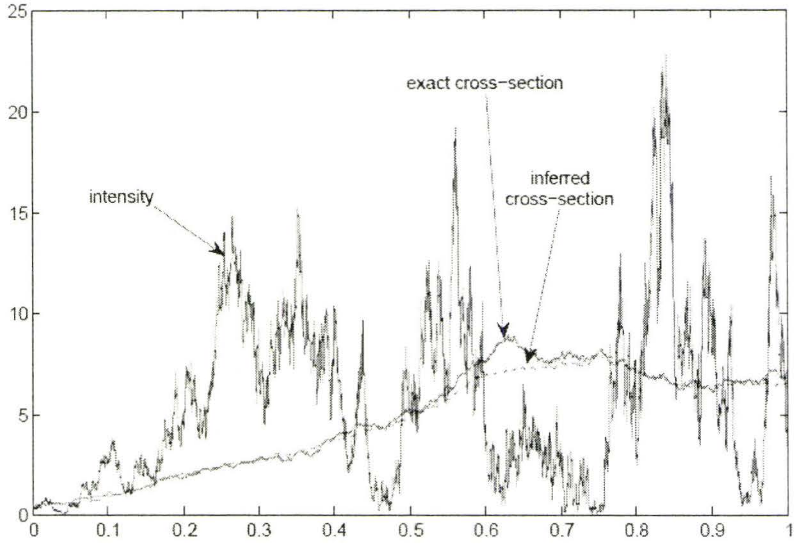

FIGURE 5.4: RCS inferred from a generalized weakly scattered amplitude with a Gamma texture through the intensity fluctuations Prop. 5.4. (For parameter values $\alpha = 20$, $\mathcal{A} = 10^{-3}$, $\mathcal{B} = 10^{-2}$, $\delta_t = 0.05$.)

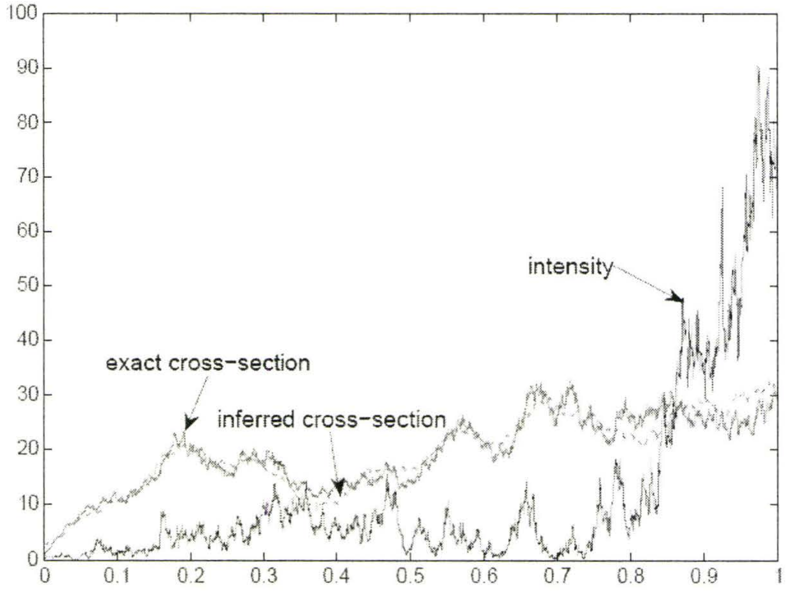

FIGURE 5.5: RCS inferred from a homodyned weakly scattered amplitude with an inverse Gamma texture through the intensity fluctuations Prop. 5.4. (For parameter values $\alpha = 20$, $\mathcal{A} = 10^{-3}$, $\mathcal{B} = 10^{-2}$, $\delta_t = 0.05$.)

5.3.2 Intensity fluctuations

The discretization of Proposition 5.4 yields the following estimate for the state

$$\delta Z_i^2/Z_i - 2\delta Z_i \delta\Theta_i/\left(\tan\phi_i\right) \propto x_i n_i^2 \tag{5.38}$$

where $\{n_i\}$ are an independent collection of $\mathcal{N}(0,1)$ distributed random variables (compare with (5.37)). As the companion estimate of (5.37), (5.38) yields another estimate of the RCS according to the procedure thoroughly described in Section 5.3.1 for Proposition 5.3.

Also provided are two simulation examples. First, a generalized weakly scattered amplitude for a Gamma distributed RCS for which the estimated state and the exact state have a correlation coefficient of 0.986 (cf. Fig. 5.4) and then a homodyned weakly scattered amplitude amplitude for an inverse Gamma texture (Fig. 5.5, statistical correlation of 0.974).

5.4 Discussion

5.4.1 Optimization

The discrepancy between the RCS estimates (obtained through Props. 5.3 and 5.4) and the exact RCS is an important criterion to asses the fidelity of the inference processes. The smoothing error, in a MSE sense, is defined as

$$\epsilon_{\text{sm}}(\Delta) \;=\; \mathbb{E}\left[\sum_{i=1}^{N}\left(x_i^{\text{sm}} - x_i\right)^2\right] \tag{5.39}$$

and depends on Δ, the number of pulses over which the intensity and phase fluctuations in, respectively, (5.37) and (5.38) are averaged. It is actually possible to derive analytical expressions for this analytical error and a subsequent condition on $\boldsymbol{\Delta}$ to optimize the inference. As the inference procedures for strongly and weakly scattered amplitude share many features, these formulae are bearing a certain similitude with those derived in the strong scattering case (cf. Section 4.2.1, *orig.* Fayard and Field, 2008). In effect, the derivation steps for a strongly scattered amplitude in Section 4.2.2 are only concerned with the left-hand side of (4.4) and do not depend on the right-hand side, that is on the estimate obtained from the amplitude time-series. In other words, these results are connected to the time-evolution of the RCS rather than to the expression of the RCS estimate.

Consequently, Propositions 4.2 and 4.3 are also valid for a weakly scattered amplitude. They are illustrated for a scattering pattern considered earlier in Section 5.3.1. We consider a generalized weakly scattered amplitude for an inverse Gamma distributed texture. A RCS estimate was obtained through the phase fluctuations (5.37). Simulation results are shown in Fig. 5.6. We can see therein that the analytical expression derived for a strongly scattered amplitude (4.6) captures also the MSE error for an inferred RCS extracted from a weakly scattered amplitude.

5.4.2 Link with the strong scattering case

Equation (5.32) is a generalization, for a weakly scattered amplitude, of an earlier result on the observability of the scattering cross-section for a strongly scattered amplitude (cf. Proposition 4.1, *orig.* Field, 2005). In this former situation, $\Sigma_t^{(Z,\Theta)} = 0$ and the scattering cross-section emerges as the intensity-weighted squared fluctuations of the phase. Before discussing further the connection between these two results, let us recall the respective expressions for the phases of the strong (from (3.26)) and weak (obtained from the drift (5.15) and volatility (5.16) diffusion tensors) scattering

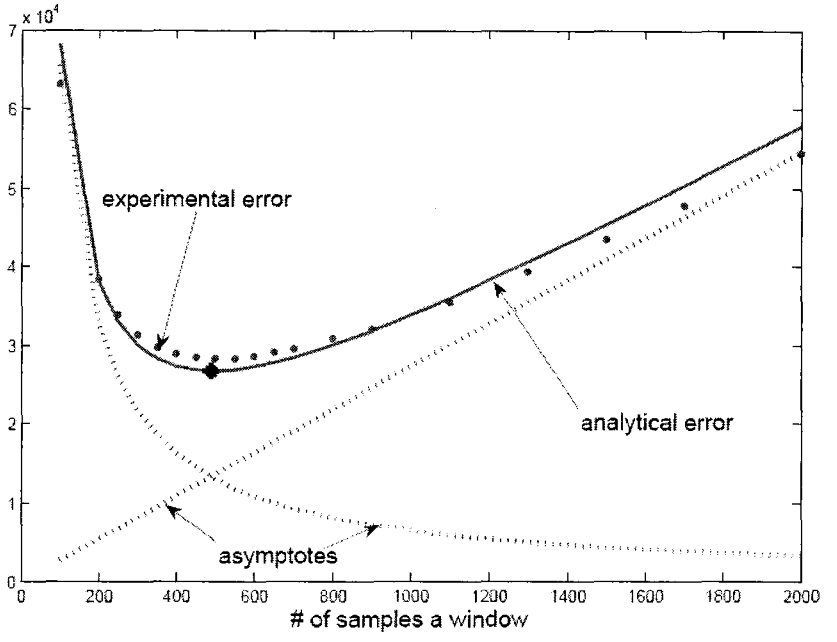

FIGURE 5.6: Experimental and analytical MSEs between the exact RCS and the RCS inferred from a generalized weakly scattered amplitude with an underlying inverse Gamma texture, whose amplitude random walk structure conforms to (3.35), through the phase fluctuations (5.3). (For parameter values $\alpha = 20$, $\mathcal{A} = 10^{-3}$, $\mathcal{B} = 10^{-2}$, $\delta_t = 0.05$.)

amplitude

$$\mathrm{d}\theta_t = \left(\frac{\mathcal{B}x_t}{2z_t}\right)^{\frac{1}{2}} \mathrm{d}W_t^{(\theta)} \tag{5.40}$$

$$\begin{aligned} \mathrm{d}\Theta_t &= \sin\Theta\left[\mathcal{A}\left(\frac{b}{2x} - \frac{\sigma}{4x^2} - e'b - e''\sigma\right) - \frac{1}{2}\mathcal{B}e\right]/Z^{\frac{1}{2}}\mathrm{d}t \\ &\quad -\frac{1}{x^2}Z_t^{\frac{1}{2}}\sin\Theta_t\left(e_t - 2e_t'x\right)\left[Z + Z^{\frac{1}{2}}\cos\Theta(2e_t'x_t - e_t)\right]/Z^2\mathrm{d}t \\ &\quad +\frac{1}{2Z_t}\left[2\left(\mathcal{B}x_t\right)^{1/2}\Im\left[\Psi_t^*\mathrm{d}\xi_t\right] + (2\mathcal{A}\sigma_t)^{\frac{1}{2}}\frac{Z_t^{\frac{1}{2}}\sin\Theta_t\left(e_t - 2e_t'x\right)}{x}\mathrm{d}W_t^{(x)}\right]. \end{aligned} \tag{5.41}$$

Since $\mathrm{d}\theta_t$ is a pure volatility process, the fact that the cross-section is observable through the phase fluctuations is rather intuitive. Guessing the corresponding result for $\mathrm{d}\Theta_t$ requires a bit more of imagination. In the natural radial/angular basis, the volatility coefficients are rather cumbersome whereas they have simpler expressions in the $\{\alpha_t, \beta_t\}$ basis when expressed in terms of θ_t. In effect, the presence of a coherent offset in (3.30) spoils the geometrical structures of a strongly scattered amplitude, namely the independence between the radial and angular fluctuations.

Upon the comparison of (4.1) and (5.32), the RCS estimate for a weakly scattered amplitude possesses an additional term originating in the radial/angular cross-volatility. It is instructive that it also involves the angle of rotation of the dyad from that aligned to the instantaneous radial direction θ_t. The result obtained in the strong scattering case was a consequence of the independence between the angular and radial fluctuations. Our discussion of the scattering amplitude fluctuations in Section 5.1.4 projects the weakly scattered amplitude onto a new basis $\{\alpha_t, \beta_t\}$ in which the RCS is observable as the radial/angular fluctuations $\mathrm{d}\Theta_t$ and $\mathrm{d}Z_t$ de-correlate like in the strong scattering case. Thereafter, the second term in the right-hand side of (5.32) accounts for the change of basis.

As the coherent offset e_t tends to zero, so strong scattering is approached, $\Sigma_t^{(Z,\Theta)}$ and $\tan\phi_t$ tend identically to zero, whereas their ratio tends to $\mathcal{A}Z_t\sigma_t/x_t^2$. In such a case, the cross-section can only be obtained by solving the resulting cubic equation for x_t or alternatively by taking the limit of the aforementioned ratio. On the other hand, (5.32) is directly expressed in terms of observable quantities for $e_t = 0$. Consequently, out of the two expressions for the cross-section (5.32) and (5.36), only the former offers a convenient means the inference of the cross-section when no coherent offset is present. Nevertheless, since the volatility coefficients and the angle ϕ_t are observable quantities, we have thus provided two procedures to extract the hidden cross-section from scattering data.

Interestingly, Propositions 5.3 and 5.4 are purely geometrical in nature. They only stem from the compound representation of the strongly scattered amplitude in terms of a Gaussian process modulated the square-root of a real-valued population or, alternatively, from the dynamical random walk model (Jakeman, 1980). Moreover, both this multiplicative nature and the underlying statistical independence between x_t and γ_t are well-established in the literature and have been justified on experimental grounds. An essential feature of these results (5.32) and (5.36) lies in their validity for a broad range of experimental situations (as evidenced by the quite distinct simulation examples). It does not only pertain for an arbitrary cross-section x_t but also for any coherent offset e_t. It is a direct consequence of the multiplicative nature (3.11) of the scattered amplitude in terms of two independent components. As such, this technique might be used without prior assumption concerning the scattering pattern, provided that it conforms to the compound representation (and is likewise less sensitive to the formalism).

Chapter 6

Conclusion

6.1 Summary

Firstly, in Chapter 2 we have described scattering from a rough medium, e.g., a marine surface. In particular, we have introduced the concepts of speckle and RCS. Owing to the complexity of the interaction between the incident wave and the rough surface, it is easier to provide a statistical description of the scattering process as opposed to one based on solutions of Maxwell's equations with boundary conditions (Blackledge, 2009). A widespread model for the received amplitude is that of a random walk with a fluctuating number of steps which paves the way towards the K-distribution for the scattered intensity that radar engineers are using to model radar returns. Of the two components it involves, the Rayleigh speckle and the local power (the RCS), the latter may be justified on the basis of an underlying discrete BDI population model (for which the transitions are linear functions of the actual population level). Next, we have provided a Fokker–Planck description for the texture of the scattered amplitude. Extending this model to a broader class of diffusion processes, the Pearson class, enables the derivation of a few other probability distributions, principled after an extension of the BDI process, that have been successfully confronted with actual radar data.

In Chapter 3, which does not contain any new result, we have provided a thorough account of the dynamical stochastic model (*orig.* Field and Tough, 2003b) accounting for the strong scattering amplitude, phase and intensity dynamics. Based on the same conceptual decomposition of the scattered amplitude as a random walk model with step number fluctuations, it yields the compound representation of the K-scattered amplitude in terms of a Rayleigh speckle and a Gamma texture most characteristic of actual scattering data (Ward, 1981). We have also defined the weak scattering situation in which the strongly scattered amplitude lies in the presence of a coherent offset. Next, we have recalled the spectral properties of a weakly scattered amplitude that can be obtained from the propagator of the RCS SDE. In effect, an advantage of the dynamical representation is the possibility to derive any high-order statistics from the propagator of the RCS. This chapter ends with a discussion of the numerical simulation of SDEs which enables one to emulate scattering patterns in order to assess this thesis' findings.

In Chapter 4 we have investigated how the RCS could be inferred from the time-series of a strongly scattered amplitude. Out of the two components of ψ_t introduced in Chapter 3, the slowly varying RCS and the more rapidly varying speckle, only the former is of interest for radar engineers. Walking in the steps of Field (2005) where a procedure to extract the RCS from the intensity-weighted fluctuations of the phase was outlined, we have provided an analytical expression for the subsequent discrepancy between the exact RCS and the estimated RCS. This formula, depending on the number of samples over which the phase de-coherence is averaged optimizes the inference procedure by specifying a condition on the smoothing window length. Also considered was another experimental situation where a strongly scattered amplitude lies in superposition with an additional white noise (see Watts, 1981). In this case, anomaly detection was shown to still be possible through the phase fluctuations after a filtering step which takes advantage of the known spectral properties of the received amplitude, derived from the stochastic dynamical model developed by Field and Tough (2003b).

Chapter 5 aims to extend the result given in Chapter 4 to a weakly scattered amplitude. An essential feature of the strongly scattered amplitude is the independence between its radial and angular fluctuations which permits the inference of the RCS. Owing to the presence of a coherent offset, this property is no longer valid for a weakly scattered amplitude. Nevertheless, scrutinizing the geometry of weakly scattered amplitude fluctuations permits the derivation of two distinct procedures to infer the RCS. In effect, the angle of rotation of the dyad ϕ_t w.r.t. which the fluctuations of Ψ_t de-correlate is connected to the cross-volatility of the process. As such, decomposing the scattered amplitude fluctuations into radial and angular components enables the expression of the RCS in terms of observable quantities. These results originate from the geometrical features of the weakly scattered amplitude and thus encompass the aforementioned equivalent result for a strongly scattered amplitude described in Chapter 4.

6.2 Discussion

The compound Gaussian model for the scattered amplitude posits a Gaussian speckle γ_t modulated by a slowly varying cross-section x_t. For the latter, we have considered four different probability densities: Gamma, inverse Gamma, beta of the first kind and beta prime distributions. The various scattered amplitudes resulting from these textures through (2.17) have all been shown to suit scattered data (Delignon et al., 1997; Gini et al., 2000; Delignon and Pieczynski, 2002; Balleri et al., 2007). They were obtained as the asymptotic densities of diffusions belonging to the Pearson class. Stating the dynamics of these textures under the form (2.46) has experimental advantages since their propagators, known from Wong (1963), enables the derivation of any higher-order statistics. This family of processes has been justified on the basis of an underlying discrete population model, accounting for the step number fluctuations of the random walk model (2.1), which is nothing but the BDI process (which yields a K–distributed amplitude) with additional quadratic terms in the state transition functions. Thus provided is a framework, physically motivated, that incorporates the aforementioned textures. As a parametric generalization of the BDI process, the Pearson class of diffusions could provide a more refined model for scattering data that exhibit a slight deviation from the K–distribution. Another advantage of the Pearson class of diffusions coupled with the multiplicative representation of the scattered amplitude is the possibility to extract the population model parameters from the scattered intensity moments.

The stochastic framework detailed in Chapter 3 enables the inference of the RCS from the scattered amplitude time-series (coherent data) through the intensity-weighted phase de-coherence (Field, 2005), as illustrated for the texture models discussed in Section 4.1.4. This theorem is of crucial importance for radar applications since it facilitates means of anomaly detection. In spite of the very strong correlation coefficient between the hidden and estimated cross-sections, they exhibit a certain discrepancy since the data are necessarily sampled/generated at finite pulse frequency. An important new result of the current thesis is to quantify analytically the extent of this error and the derivation of a condition (on the number of pulses over which the phase de-coherence is averaged) to minimize it. These formulae have been shown to capture precisely the inference error (as illustrated in Section 4.2.4 for synthetically generated data). They are rooted on the independence between the sampling process and the cross-section dynamics and as such, they solely depend on the RCS dynamics (more precisely, its volatility coefficient). In particular, they are neither impacted by the scattered amplitude time-series which they are extracted from nor by the exact expression of the state estimate which is proportional to $z_i\delta\theta_i^2$. In an experimental context, a benefit of these findings is to be equipped beforehand with an estimate of the number of samples necessary to obtain a proper estimate of the RCS. The strong correlation guaranteed by Proposition 4.1 could be lost if the smoothing window were to be too large or too small (cf. Fig. 4.5 for the impact of the smoothing length). Another advantage is to reduce the computational cost of the smoothing procedure. Without knowing Δ^{opt}, it would be necessary to try a number of different window lengths to make sure that the inferred state is a good estimate. Thanks to (4.7) this supplementary computational burden may be reduced. Furthermore, the derived formulae are only marginally sensitive to the range of the model parameters (e.g., sea-state, characteristic de-correlation time) as discussed in Section 4.2.5, thus asserting their robustness for experimental situations. Next, we have considered the experimental situation where the K–distributed noise lies in superposition with an additional white noise. The presence of this undesired term is a likely challenge to overcome for real scattering data. A first contribution was to give a dynamical representation of the noisy K-scattered amplitude originally described in Watts (1981). Indeed, (4.32) is easier to apprehend than the usual statistical description (4.33) and resembles a classic filtering problem which could be solved by the classical Wiener filter. After a filtering step, it is possible to extract the RCS from the de-noised amplitude. The resulting inferred RCS, though not as accurate as the RCS extracted from a pure K-scattering process, facilitates anomaly detection in the presence of an additional white noise.

The major contribution of the present work was to demonstrate how the RCS could be extracted from the time-series of a *weakly* scattered amplitude, thus generalizing the results described in Chapter 4 for strong scattering. We shall remind the reader of the definition of a weakly scattered amplitude

$$\Psi_t = e_t + \gamma_t x_t^{1/2} \tag{6.1}$$

as a strongly scattered amplitude lying in superposition with a coherent offset. This additional state-dependent term e_t annihilates the most important features of $\psi_t = \gamma_t x_t^{1/2}$ from which the results given in Chapter 4 are derived: its multiplicative representation and the independence between its angular and radial fluctuations. It should be appreciated that the argument for the observability of the RCS for a weakly scattered amplitude is rooted on two ingredients related to these two properties. The first element is to decompose the fluctuations of $\mathrm{d}Z_t$ and $\mathrm{d}\Theta_t$ into (independent) terms originating from the speckle and terms originating from the texture (for the coherent offset e_t is a function of the state x_t). It is as if we were to transpose the multiplicative nature of a strongly scattered amplitude to the fluctuations level. Incidently, this decomposition of $\mathrm{d}\Psi_t$ facilitates the derivation of the scattered amplitude dynamics for an arbitrary coherent offset (cf. the diffusion tensor (5.16) which can be seen as the transposition of the formulae anteriorly given in Field and Tough (2005) to a more natural basis). Moreover, this decomposition points out the analogies between the (fluctuations of the) radial and angular components of the scattered amplitude which are nothing but the real and imaginary parts of the same quantity $\Psi_t^* \mathrm{d}\Psi_t$. Also, from

(5.27), the (tangent of the) angle ϕ_t emerges as a measure of the relative strength of the radial and angular fluctuations originating from the texture. The second element is the geometry of a weakly scattered amplitude fluctuation (its investigation in Field and Tough (2005) is thereafter *a posteriori* motivated by the thesis' findings). As described in Field (2005), the observability of the RCS for a strongly scattered amplitude applies to a situation where the angular and radial fluctuations of ψ_t are independent. Keeping this in mind, our derivation of Propositions 5.3 and 5.4 may be seen as a basis transformation which projects the radial and angular fluctuations into a more natural basis where they de-correlate. Thereafter, the observability of the RCS is proven by the same token as in the strong scattering case. If we develop further this idea, the additional terms in (5.32) and (5.36) account for the change of basis. Thereafter, the observability of the RCS for a strongly scattered amplitude reported in Field (2005) is a particular instance of Proposition 5.3. In light of our present contribution, this earlier result is encompassed by our discussion when the second term in the right-hand side of (5.32) vanishes and thus requires the angular and radial components of the scattered amplitude fluctuations to be statistically independent. For certain radar applications, this is a legitimate assumption. For weak scattering however, this assumption fails (as evidenced by (5.8)) and the correlation structure represented by the cross-volatility provides an essential ingredient to observe the cross-section. Moreover, a supplementary method of inferring the RCS through the intensity fluctuations, which was not given in Field (2005), can be derived thanks to the aforementioned similarities between the radial and angular fluctuations. All these inference algorithms provide estimates for the RCS in local time at a small computational cost. The techniques, as in Field (2005), are also not confined to the category of diffusions, extending into the wider class of Ito processes for the various scattering quantities. Next, our methods can be applied with little assumptions concerning the amplitude model. In effect, both strong and weak scattering (for any coherent offset) are covered by this expression. As such, the techniques presented may be used without prior assumption concerning the detailed scattering dynamics, provided they conform to the compound representation. It is an advantage since the procedure is less sensitive to modeling approximations which could enhance its robustness w.r.t. real data. This is illustrated by the various simulation examples which show that the inference procedures work equally well for a HK/GK amplitude, or for any texture. Finally, it is comforting that the expressions derived in Chapter 4 to optimize the recovery of the RCS of a strongly scattered amplitude are also valid for our two procedures.

6.3 Future research

The performance of any processing scheme is ultimately limited by the extent to which its underlying modeling of the signal is realistic. The results given in this thesis are no exception. Although experimental accounts in Field and Tough (2003a) or in Bakker et al. (2007) have successfully confronted the theoretical description of the scattering amplitude given in Chapter 3 with actual radar returns, the inference techniques proposed in Chapters 4 and 5 are still awaiting experimental validation. We can anticipate the two following challenges for more practical applications. Firstly, real data are likely to be corrupted by an additive measurement noise that might spoil the geometrical properties of the scattered amplitudes on which our inference procedures are based. Secondly, data will need to be sampled at high enough frequency, as discussed in Section 4.1.2. A number of experimentalists (e.g. Farina et al., 1997) have observed that different polarizations yield distinct scattering patterns. Our discussion does not incorporate this issue and it would be interesting to see how the polarization influences the stochastic model discussed in Chapter 3. In particular, would it just impact the RCS parameter α in (3.13), as suggested by the empirical models for the RCS (Horst et al., 1978), or more generally, the drift and volatility functions. As discussed in Section 2.3.3, as the parameters of the underlying population model are observable through the intensity moments, experimental differences between polarization could be better understood in terms of the associated population model. One should observe that Proposition 5.3 is valid as it stands for: arbitrary cross-section dynamics x_t, weak or strong scattering, any coherent offset e_t. As such, the inference procedure may be expected not to be much impacted by modeling shortcomings. For actual scattering data, this feature represents an asset. In another more applied setting, it would also be useful to devise more efficient schemes to compute the cross-volatility

$\Sigma_t^{(Z,\Theta)}$ and $\tan\phi_t$ that feature on the right-hand sides of (5.32) and (5.36). Also, the statistical description of the sea clutter enables the derivation of probabilities of detection/false alarms which in turn permit to set up a radar's specifications. Our approach should also be translated in terms of radar specifications.

The findings highlighted in this thesis may also be relevant to spin dynamics in NMR and spectroscopy applications. In this context, the sample to be examined lies inside a constant magnetic field B_0 which aligns the spins of the protons. After being excited by a RF pulse, the orientation of the magnetization vector is shifted by 90°. The free induction decay (FID) signal arises from the motion of the spins moments back to their equilibrium situation. The random fluctuations of a spin system at equilibrium (as postulated by NMR pioneers like Bloch (1946)) is a key ingredient to understand the nature of the FID signal. Physically, these fluctuations originate from a number of small molecular interactions. As investigated in Field and Bain (2009) they may be accommodated by the random walk model (2.1) for a constant number of steps. In effect, NMR imaging and scattering from a random medium share certain features, that is, the in-phase and quadrature-phase decomposition of the received signal. Nevertheless, the analogy between NMR scattering and scattering from a rough medium is more mathematical than physical (since magnetic resonance is mainly near field). This random walk model could provide a theoretical description of the *spin noise* which recently attracted interest (Müller and Jerschow, 2006) where a spin-noise signal (weak compared to the signal following a pulse) is observed for a spin population at equilibrium. Thereafter, the relaxation time T_2 is observable as the reciprocal of the characteristic frequency $\mathcal{B}$ in (3.7). As opposed to the current thesis which aims to infer the time-varying population of scatterers, most NMR applications posit a spins' population constant over time. As such, most of the findings exposed in Chapters 4 and 5 are not directly relevant to NMR applications. Nonetheless, the coherent offset in (3.30) could account for an exogenous disturbance of ferromagnetic origin that would prompt the spins towards a particular orientation. Moreover, the K–distribution plus noise model (4.32) echoes spin noise experiments where the tiny signal of interest lies in an additional thermal noise. As such, the discussion of the spectral properties of the scattered amplitude and the algorithm to extract $\mathcal{B}$ could motivate further work to investigate the relevance of the current thesis to magnetic resonance applications.

We have discussed in Chapter 2 how the texture dynamics could be derived on the grounds of a first-order population model. Further extensions of this scheme may well deserve attention (e.g., considering higher-order transitions) to account for more exotic temporal correlation structure. Also, the current description (2.25) does not reflect the spatial correlation experimentally observed in the texture. Recent work has extended the population model for the RCS at a single point in space to be spatially a correlated one, in which the spatial correlation is induced by inter-site migration, and a corresponding continuum (space) limit in terms of a path integral formalism has been discovered (Field and Tough, 2010). Although this work is restrained to a discrete population (i.e., it does not cover the SDE description of scattering when the population's mean gets asymptotically large), it has significant potential for radar simulations, especially for the generation of spatially correlated RCS patterns.
For temporal correlation, non-stationary patterns may be introduced in (3.12) by allowing the variable $\mathcal{A}$ to be explicitly time-dependent. By virtue of the corresponding appearance of $\mathcal{A}(t)$ in (2.41), the asymptotic distribution of the RCS is unaffected. Another possibility is to consider stochastic delay differential equations where the drift term is expressed as Guillouzic et al. (1999)

$$\mathrm{d}x_t \quad = \quad \mathcal{A}b_t(x_t, x_{t-\tau})\mathrm{d}t + (2\mathcal{A}\sigma_t)^{\frac{1}{2}}\,\mathrm{d}W_t^{(x)} \tag{6.2}$$

for a delay τ. This recent extension of stochastic calculus was used for optics applications (García-Ojalvo and Roy, 1996) for example. Interestingly it is possible to justify (6.2) on the basis of a delayed random walk (Ohira, 1997). The advantage of this approach is that it enables the derivation of non-stationary processes whose autocorrelation exhibits the temporal correlation experimentally observed for radar clutters (cf. Farina et al., 1997, Fig. 11). Further work may also attempt encompass the spikes observed in the radar return by the means of discrete jumps in the scatterers' population. The class A (Middleton, 1983) model posits the presence of spikes that are coherently added. Physically, they correspond to scattering from the crests of incipiently breaking waves and to the whitecaps.

As discussed in Section 4.1.2, for a strongly scattered amplitude, the inference process may be seen as related to the generalized Kalman filter[1] (cf. Øksendal, 1988, Chap. 6) where we extract a hidden state x_t through an observable state z_t

$$\begin{aligned} \mathrm{d}x_t &= \mathcal{A}b_t\mathrm{d}t + (2\mathcal{A}\sigma_t)^{\frac{1}{2}}\,\mathrm{d}W_t^{(x)} \quad (6.3) \\ \mathrm{d}z_t &= \left[\mathcal{A}\left(\frac{b_t z_t}{x_t}\right) + \mathcal{B}(x_t - z_t)\right]\mathrm{d}t \\ &\quad + (2\mathcal{A}\sigma_t)^{\frac{1}{2}}\left(\frac{z_t}{x_t}\right)\mathrm{d}W_t^{(x)} + (2\mathcal{B}x_t z_t)^{\frac{1}{2}}\,\mathrm{d}W_t^{(r)}. \quad (6.4) \end{aligned}$$

Interestingly, the solution originally provided by Field (2005) to this non-linear problem is independent of the dynamics of the hidden-state since Proposition 4.1 is valid for an arbitrary RCS x_t. By comparison, the Kalman estimate builds upon the state transition model of the hidden state (here, the drift b_t and volatility σ_t parameters) to construct a state estimate continually updated by comparing the actual state to the expected one. In the current thesis, the procedure we have outlined provides the exact time-series of the hidden state, directly extracted from the observed state. The situation becomes more intriguing for a weakly scattered amplitude where

$$\begin{aligned} \mathrm{d}x_t &= \mathcal{A}b_t(t, x_t)\mathrm{d}t + \left(2\mathcal{A}\sigma_t^2(t, x_t)\right)^{1/2}\mathrm{d}W_t^{(x)} \quad (6.5) \\ \Psi_t &= e(t, x_t) + \gamma_t x_t^{1/2}. \quad (6.6) \end{aligned}$$

Noticeably, a broad range of processes are covered since the inference techniques stand for any texture x_t and any coherent offset e_t. The above coupled system of equations is more indirectly reminiscent of the generalized Kalman filter where e_t represents the observation model that maps the hidden state x_t into the observation state Ψ_t and where $\psi_t = \gamma_t x_t^{1/2}$ is a state-dependent non-linear noise additive component of the measurement. However, close scrutiny reveals that the weak scattering dynamics does not fit precisely into the standard filtering framework, even if one allows for non-linearity in the dynamical equations. This is due to the precise dependencies of the measurement process on the state in terms of the noise and dynamical parameters. Thus, a non-linear filter does not exist to extract an estimate of the state for weak

[1]which requires the Brownian terms of the hidden/observed states to be independent which is not the case for (6.3) and (6.4)

scattering. Similar remarks apply to attempts to estimate the cross-section from intensity time series, for strong (or weak) scattering. The approach developed in Chapter 5 is therefore of essential value, enabling filtering for situations in which standard non-linear filtering methods fail. In this vein, Propositions 5.4 and 5.3, which enable the recovery of the state x_t, emerge as a filtering algorithm that exploits the geometry of the observed state's volatility. Motivated by the change of perspective offered by these inference techniques, one may investigate whether in a more general situation, when ψ_t is not specified by (3.11), the observed state volatility also permits the inference of the state x_t. The performance of such an 'ideal filter' that extracts time-series of the hidden state should then be compared with existing (approximate) non-linear filtering techniques.

Appendix A

BDI model

The following appendix provides an overview of the BDI model. Refer to Bartlett (1966) for a complete exposition.

A.1 PDE for the partition function of a BDI model

For generation rate $G_N(t)$ and recombination rate $R_N(t)$, the master equation reads (cf. Fig. 2.2)

$$\frac{\mathrm{d}\mathcal{P}_N}{\mathrm{d}t} = G_{N-1}\mathcal{P}_{N-1} - (G_N + R_N)\mathcal{P}_N + R_{N+1}\mathcal{P}_{N+1}. \tag{A.1}$$

If we consider a BDI population model with transition rates $G_N(t) = \lambda N + \nu$ and $R_N(t) = \mu N$, (A.1) becomes

$$\frac{\mathrm{d}\mathcal{P}_N}{\mathrm{d}t} = (\lambda(N-1) + \nu)\,\mathcal{P}_{N-1} - ((\lambda + \mu)N + \nu)\,\mathcal{P}_N + (\mu(N+1))\,\mathcal{P}_{N+1}. \tag{A.2}$$

By considering the summation over N of (A.2) weighted by z^N, we obtain

$$\begin{aligned}
\frac{\mathrm{d}}{\mathrm{d}t}\sum_{N=0}^{\infty} z^N P_N &= \sum_{N=0}^{\infty}(\lambda N+\nu)\, z^{N+1}P_N - \sum_{N=0}^{\infty}(\lambda N+\mu N+\nu)\, z^N P_N + \sum_{N=1}^{\infty}(\mu N)\, z^{N-1}P_N \\
\frac{\mathrm{d}}{\mathrm{d}t}\sum_{N=0}^{\infty} z^N P_N &= \nu(z-1)\sum_{N=0}^{\infty} z^N P_N + (z-1)(\lambda z-\mu)\sum_{N=1}^{\infty} z^{N-1}P_N \\
\frac{\partial \Pi_t(z)}{\partial t} &= (\lambda z-\mu)(z-1)\frac{\partial \Pi_t(z)}{\partial z} + \nu(z-1)\Pi_t(z) \qquad \text{(A.3)}
\end{aligned}$$

with the initial condition

$$\Pi_0(z) = z^{N_0} \qquad \text{(A.4)}$$

where N_0 is the initial number of individuals.

A.2 Partition function for a BDI population

A.2.1 Forward Kolmogorov equation

To find the solution of the FPE (A.3) with initial condition (A.4), we first need to consider the partition function in discrete time $\Pi_r(z)_{r=0,1,2}$. Let us introduce the distribution of the progeny

$$G(z) = \langle z^{N_{r+1}} \rangle_{N_r=1}. \qquad \text{(A.5)}$$

$G(z)$ represents the evolution over one time-step of a single individual. Given G, one can propagate Π_r (under the assumption that the individuals behave identically, independently) through the backward and forward Kolmogorov equations

$$\Pi_{r+1} = G\left(\Pi_r(z)\right) \qquad \text{(A.6)}$$

$$\Pi_{r+1} = \Pi_r\left(G(z)\right) \qquad \text{(A.7)}$$

For a sufficiently small time-step δ_t, G can be expanded as

$$G(z) = z + g(z)\delta_t + \wr(\delta_t) \tag{A.8}$$

where the first time accounts for the self-replication of the individual if $\delta_t = 0$. The time-derivative of the partition function may be expressed as

$$\frac{\partial \Pi_t(z)}{\partial t} = \lim_{\delta_t \to 0} \frac{\Pi_r(z) - \Pi_{r-1}(z)}{\delta_t} \tag{A.9}$$

$$\frac{\partial \Pi_t(z)}{\partial t} = g(\Pi_t(z)) \tag{A.10}$$

where we have used the backward Kolmogorov equation (A.7) to substitue $\Pi_{r-1}(z + g(z)\delta_t + \wr(\delta_t)) \approx \Pi_{r-1}(z) + \partial \Pi_{r-1}/\partial z * g(z)\delta_t$. By identifying g between (A.2) and (A.10) without taking into account the immigration $\nu = 0$,

$$g(z) = \lambda(z^2 - z) + \mu(1 - z). \tag{A.11}$$

A.2.2 Birth-death process

Equation (A.10) is solved via the method of characteristic functions (Bartlett, 1966). Let $\Pi_t(z) = \Psi(Z)$. A constant Z corresponds to curves in (t, z) plane. Along such a curve,

$$\mathrm{d}\Pi = 0 \tag{A.12}$$

$$\frac{\partial \Pi}{\partial z}\mathrm{d}z + \frac{\partial \Pi}{\partial t}\mathrm{d}t = 0. \tag{A.13}$$

So, (A.10) reduces to the differential equation along a curve

$$\frac{\mathrm{d}z}{\mathrm{d}t} = \frac{-\frac{\partial \Pi}{\partial t}}{\frac{\partial \Pi}{\partial z}} \tag{A.14}$$

$$\frac{\mathrm{d}z}{\mathrm{d}t} = -(z - 1)(\lambda z - \mu). \tag{A.15}$$

Under the change of variables $z-1=1/u$, a solution to (A.15) reads

$$u\mathrm{e}^{\rho} = \int_0^t \lambda \mathrm{e}^{\rho}\mathrm{d}t + \text{constant}, \tag{A.16}$$

where we have introduced

$$\rho = \int_0^t (\mu-\lambda)\,\mathrm{d}t. \tag{A.17}$$

In terms of the partition function, (A.16) is recast as

$$\Pi_t(z) = \Psi\left(\frac{\mathrm{e}^{\rho}}{z-1} - \int_0^t \lambda \mathrm{e}^{\rho}\mathrm{d}t\right). \tag{A.18}$$

Next, we have to make sure that our solution complies with the initial condition (A.4), namely $\Pi_0(z)=z$. Therefore, we have $z=\Psi(1-1/z)$ and $\Psi(x)=1+1/x$. The solution to (A.3) is therefore

$$\Pi_t(z) = 1+\left[\frac{\mathrm{e}^{\rho}}{z-1} - \int_0^t \lambda \mathrm{e}^{\rho}\mathrm{d}t\right]^{-1} \tag{A.19}$$

A.2.3 Effect of immigration

Before taking into account the immigration, let us introduce $G(z,t,\tau)$, the partition function at time t for an individual present at time τ in absence of immigration. Next, at any given time, the number of individuals may be written as

$$N_t = N_t^{(\mathrm{BD})} + \sum_r N_t^{(\tau_r)} \tag{A.20}$$

where the superscripts (BD) and (τ_r) denote, respectively, the individuals of the pure birth-death process and the individuals that have immigrated at time τ_r.

Since the $N^{(\tau_r)}$ are independent over r, we can write the partition function as

$$\Pi_t(z) = \langle z^{N_t^{\mathrm{BD}}+\sum_r N_t^{\tau_r}} \rangle \tag{A.21}$$

$$\Pi_t(z) = \langle z^{N_t^{\mathrm{BD}}} \rangle \langle z^{\sum_r N_t^{\tau_r}} \rangle \tag{A.22}$$

where the first term can be written as $G^{N_0}(z,t,0)$[1] since it depicts the original individuals subjected to a birth-death process at time t. As the probability that one individual immigrates in the interval $[\tau_r, \tau_r + \Delta\tau)$ is given by $\nu(\tau_r)\Delta\tau$, we can substitute

$$\langle z^{N_t^{(\tau_r)}} \rangle = G(z,t,\tau_r)\nu(\tau_r)\Delta\tau + 1(1-\nu(\tau_r)\Delta\tau), \tag{A.23}$$

and the partition function reads

$$\Pi_t(z) = G^{N_0}(t,z,0)\prod_t \left(1+\nu(\tau_r)\Delta\tau\left[G(z,t,\tau_t)-1\right]\right) \tag{A.24}$$

which reduces to

$$\Pi_t(z) = G^{N_0}(t,z,0)\exp\left[\int_0^t \left(G(t,z,\tau)-1\right)\nu(\tau)\mathrm{d}\tau\right] \tag{A.25}$$

in the limit $\Delta\tau \to 0$.

For a BDI model with constant transition rates, (A.25) is found to be

$$\Pi_t(z) = \frac{(\lambda-\mu)^{\nu/\lambda}\left[\mu(T-1)-(\mu T-\lambda)z\right]^{N_0}}{\left[\lambda T-\mu-\lambda(T-1)z\right]^{N_0+\nu/\lambda}} \tag{A.26}$$

where $T = \mathrm{e}^{(\lambda-\mu)t}$ if we substitute $G(z,t,\tau)$ the formula (A.19) evaluated at time $t' = t - \tau$.

[1]this term actually tends to one since the original individuals will die at some point. Compare with (Vyasa, before 3[rd] century BCE): "For the born, death is certain. These bodies come to an end, only the vast embodied Âtman is eternal. Therefore, you must fight Arjun !"

Appendix B

Ito calculus

The following appendix provides an overview of stochastic calculus, for the reader unfamiliar with these concepts. Refer to Øksendal (1988) for a complete exposition.

B.1 Brownian motion

B.1.1 Derivation

Consider the independent coin tossing experiments with $p = q = 1/2$. Put

$$X_j = \begin{cases} 1 & \text{if} \quad w_j = H \\ -1 & \text{if} \quad w_j = -H \end{cases} \tag{B.1}$$

and define the 1-D symmetric random walk

$$M = \begin{cases} M_0 = 0 \\ M_k = \sum_{j=1}^{k} X_j \end{cases} \tag{B.2}$$

The 1-D random walk is a discrete stochastic process with positive quadratic variation The quadratic variation of the 1-D random walk, defined as

$$[M, M]_n \equiv \sum_{k=1}^{n} (M_k - M_{k-1})^2, \tag{B.3}$$

is positive and reads

$$[M, M]_n = \sum_{k=1}^{n} X_k^2 = n. \tag{B.4}$$

This notion of quadratic variation is a key ingredient of Ito calculus (Karatzas and Shreve, 1988, Chap. 3). The Wiener process is obtained as the limit for a large n of the scaled random walk

$$W_t^{(n)} = \frac{1}{\sqrt{n}} M_{nt}. \tag{B.5}$$

B.1.2 Properties

A Brownian motion or Wiener process W_t, illustrated in Fig. B.1, is a stochastic process satisfying the following three properties

1. Initial condition: $W_{t=0} = 0$

2. Independent increments

$$\mathbb{E}\left[(W_v - W_u)(W_t - W_s)\right] = 0 \tag{B.6}$$

where $s < t \leq u < v$ so that the increments over non-overlapping intervals are independent.

3. Normal increments

$$W_t - W_s \sim \mathcal{N}(0, |t - s|) \tag{B.7}$$

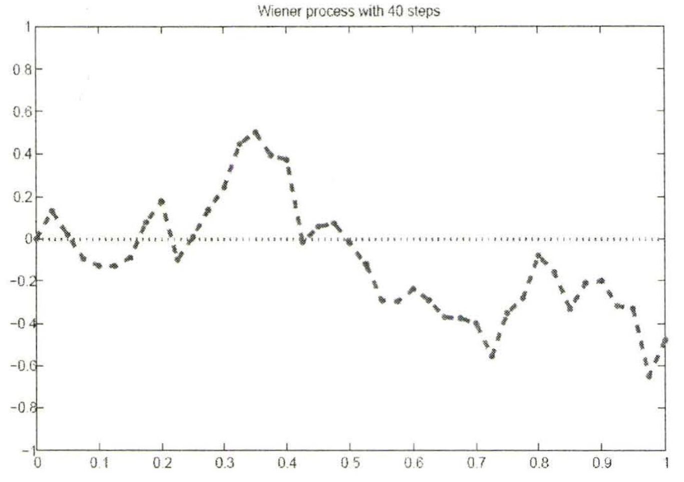

FIGURE B.1: Realization of a Wiener process.

B.2 Stochastic Differential Equation

A SDE for the stochastic process X_t is, in terms of the drift coefficient b_t and of the volatility coefficient Σ_t, an equation of the form:

$$\mathrm{d}X_t = b(t, X_t)\mathrm{d}t + \Sigma(t, X_t)\mathrm{d}W_t \tag{B.8}$$

which is a shorthand notation for

$$X_t \;=\; X_0 + \int_0^t b(s, X_s)\mathrm{d}s + \int_0^t \Sigma(s, X_s)\mathrm{d}W_s. \tag{B.9}$$

B.3 Ito integral

The definition of the SDE (B.8) makes use of an Ito integral, where the integrand is taken with respect to a Brownian motion W_t. This notion is a key point in stochastic calculus and appears as an extension of the Lebesgue integral. Let $0 = t_0 < t_1 < ... < t_n = T$ be a partition and $F_s(\omega)$ be a bounded and elementary stochastic process. We define its integrands f_j as $F_s(\omega) = \sum_{j=0}^{n-1} f_j(\omega)\mathbb{1}_{[t_j;t_{j+1})}$ where $\mathbb{1}$ is the indicator function. For these integrands, we can define the Itō integral I_s, for $t_k \leq s \leq t_{k+1}$ by

$$I_s = \sum_{j=0}^{n-1} f_j \left(W_{t_{j+1}} - W_{t_j}\right) + f_k(W_s - W_k). \tag{B.10}$$

for the Brownian motion W_t. The Ito integrand satisfies the additional property

$$(\mathrm{d}W_t)^\alpha = \mathrm{d}t, \quad \text{if } \alpha = 2 \tag{B.11}$$

$$= 0, \quad \forall \alpha > 2. \tag{B.12}$$

B.4 Ito's formula

For a twice continuously differentiable function f, the Ito differential of the random variable $Y_t = f(t, X_t)$ is given by

$$\mathrm{d}Y_t = \frac{\partial f}{\partial t}(t, X_t)\mathrm{d}t + \frac{\partial f}{\partial x}(t, X_t)\mathrm{d}X_t + \frac{1}{2}\frac{\partial^2 f}{\partial x^2}(t, X_t)\mathrm{d}X_t^2. \tag{B.13}$$

Ito's formula constitutes a departure from the classical rules of calculus as the process X_t has positive quadratic variation.

B.5 Ito product rule

Ito product rule is a modification of the classical Leibnitz rule. Explicitely, for a pair of stochastic processes $U_t V_t$, we write the product differential as

$$\mathrm{d}(U_t V_t) = U_t \mathrm{d}V_t + V_t \mathrm{d}U_t + \mathrm{d}U_t \mathrm{d}V_t \tag{B.14}$$

in which the third term accounts for the processes' quadratic variations.

B.6 Stratonovich vs Ito integrals

A stochastic process X_t has two concurrent representations

$$\mathrm{d}X_t = \begin{cases} b^{(I)}\mathrm{d}t + \Sigma \mathrm{d}W_t \\ b^{(S)}\mathrm{d}t + \Sigma \circ \mathrm{d}W_t \end{cases} \tag{B.15}$$

in which $b^{(I)}, b^{(S)}$ denote the drifts in the Ito and Stratonovich senses and '$\circ$' is a shorthand that indicates the Stratonovich prescription for taking the stochastic integral, i,e., the volatility is evaluated at the midpoint of each interval. These two prescriptions define uniquely a stochastic process X_t and their coefficients are related as (Field, 2009, pp. 155–156)

$$\Sigma \circ \mathrm{d}W_t = \Sigma \mathrm{d}W_t + \frac{1}{2}\Sigma\partial_x\Sigma \mathrm{d}t \tag{B.16}$$

$$b^{(I)} = b^{(S)} + \frac{1}{2}\Sigma\partial_x\Sigma \tag{B.17}$$

where the factor $\frac{1}{2}$ originates from the fact that the Stratonovich integral is evaluated at the midpoint.

Appendix C

Useful mathematical facts

This Appendix provides the reader with a definition of the common probability distributions mentioned in the thesis and of various special functions quoted from Abramowitz and Stegun (1972); Wolfram (1999). Also given are a few formulae from Gradshteyn and Ryzhik (1967).

C.1 Probability distributions

C.1.1 Poisson distribution

$$\mathbb{P}[x] = \frac{\alpha^x e^{-\alpha}}{x!} \tag{C.1}$$

for $x = 0, 1, 2 \ldots$.

$$\phi_x(s) = e^{\alpha(e^s - 1)} \quad \mathbb{E}[x] = \alpha \quad \mathrm{Var}(x) = \alpha$$

C.1.2 Negative binomial aka Pascal

$$\mathbb{P}[x] = \binom{x-1}{k-1} p^k (1-1)^{x-k} \tag{C.2}$$

for $x = 0, 1, 2...k$.

$$\phi_x(s) = \left(\frac{p\mathrm{e}^s}{1-(1-p)\mathrm{e}^s}\right)^k \tag{C.3}$$

$$\mathbb{E}[x] = k/p \qquad \mathrm{Var}(x) = k(1-p)/p^2$$

C.1.3 Gaussian

$$\mathbb{P}[x] = \frac{1}{\sqrt{2\pi\sigma^2}} \exp\left(-(x-m)^2/2\sigma^2\right) \tag{C.4}$$

for $-\infty < x < \infty$.

$$\phi_x(s) = \mathrm{e}^{s\mu + s^2\sigma^2/2} \quad \mathbb{E}[x] = \mu \quad \mathrm{Var}(x) = \sigma^2$$

C.1.4 Gamma

$$\mathbb{P}[x] = \frac{b^\nu}{\Gamma(\nu)} x^{\nu-1} \exp(-bx) \tag{C.5}$$

for $x > 0$.

$$\phi_x(s) = \frac{1}{1-s/b}^{\nu} \quad \mathbb{E}[x] = \tfrac{\nu}{b} \quad \mathrm{Var}(x) = \frac{\nu}{b^2}$$

for $x \geq 0$.

C.1.5 Cauchy

$$\mathbb{P}[x] = \frac{1}{\pi} \frac{b}{(x-m)^2 + b^2} \tag{C.6}$$

for $x > 0$.

$$\phi_x(s) = \mathrm{e}^{ims - b|s|^2} \tag{C.7}$$

The moments μ_n are undefined for $n \geq 1$.

C.1.6 Rayleigh

$$\mathbb{P}[x] = a^2 x \mathrm{e}^{-a^2 x^2/2} \tag{C.8}$$

for $x > 0$.

$$\mathbb{E}[x] = \sqrt{\frac{\pi}{2a^2}} \qquad \mathrm{Var}(x) = \frac{2 - \pi/2}{a^2}$$

C.1.7 *K*–distribution

$$\mathbb{P}[z] = \frac{b^\nu}{\Gamma(\nu)} \int_0^\infty x^{\nu-2} \exp(-bx) \exp(-z/x) dx \tag{C.9}$$

$$\begin{aligned}
\langle z^n \rangle &= \frac{b^\nu}{\Gamma(\nu)} \int_0^\infty x^{\nu-2} \exp(-bx) dx \int_0^\infty z^n \exp(-z/x) dz && \text{(C.10)} \\
&= n! \frac{b^\nu}{\Gamma(\nu)} \int_0^\infty x^{\nu+n-1} \exp(-bx) dx && \text{(C.11)} \\
&= n! \frac{\Gamma(\nu+n)}{b^n \Gamma(\nu)} && \text{(C.12)}
\end{aligned}$$

$$\langle \exp(-uz) \rangle = \frac{b^\nu}{\Gamma(\nu)} \int_0^\infty x^{\nu-2} \exp(-bx)dx \int_0^\infty \exp(-uz - z/x)dz \quad \text{(C.13)}$$
$$= \frac{b^\nu}{\Gamma(\nu)} \int_0^\infty \frac{x^{\nu-1}\exp(-bx)}{1+ux}dx \quad \text{(C.14)}$$
$$= \frac{b}{u} \int_0^\infty \frac{\exp(-bs/u)}{(1+s)^\nu}ds \quad \text{(C.15)}$$

from which the moments (C.10) are recovered by an appropriate small u expansion.

The behaviour of the tail of (C.9) is approximated by the same token as (C.28) (Ward et al., 2006)

$$\mathbb{P}[z] = \frac{b^\nu}{\Gamma(\nu)} z^{(\nu-1)/2} \int_0^\infty s^{\nu-2} \exp(-\sqrt{z}(bs+1/s))\mathrm{d}s \quad \text{(C.16)}$$
$$\approx \frac{b^{\nu/2+1}}{\Gamma(\nu)} z^{(\nu-1)/2} \exp(-2\sqrt{zb}) \int_{-\infty}^\infty \exp(-b\sqrt{bz}p^2)\mathrm{d}p \quad \text{(C.17)}$$
$$\approx \frac{b^{(2\nu+1)/4}}{\Gamma(\nu)} z^{(2\nu-3)/4} \exp(-2\sqrt{zb})\sqrt{\pi}. \quad \text{(C.18)}$$

C.2 Special functions

C.2.1 Bessel functions

The n^{th} Bessel function of the first kind $J_n(x)$ is defined as the solution to the differential equation

$$x^2 \frac{\mathrm{d}^2 y}{\mathrm{d}x^2} + x\frac{\mathrm{d}y}{\mathrm{d}x} + (x^2 - n^2)y = 0 \quad \text{(C.19)}$$

that is non-singular at the origin. It can also be defined by the contour integral

$$J_n(z) = \frac{1}{2\pi j} \oint \mathrm{e}^{\frac{z}{2}\left(t-\frac{1}{t}\right)} t^{-n-1}\mathrm{d}t \quad \text{(C.20)}$$

for a contour containing the origin, traversed in counterclockwise direction.

The n^{th} Bessel function of the second kind $Y_n(x)$ is the solution to (C.19) that is singular at the origin. It is related to $J_n(x)$ by

$$Y_n(x) = \frac{J_n(x)\cos(n\pi) - J_{-n}(x)}{\sin(n\pi)}. \tag{C.21}$$

The modified Bessel function of the first kind $I_n(x)$ is defined by the contour integral

$$I_n(z) = \frac{1}{2\pi j}\oint e^{\frac{z}{2}\left(t+\frac{1}{t}\right)} t^{-n-1}\mathrm{d}t \tag{C.22}$$

for a contour containing the origin, traversed in counterclockwise direction.

The modified Bessel function of the second kind $K_n(x)$ is defined as

$$K_n(x) = \frac{\pi}{2}\frac{I_n(x) - I_n(x)}{\sin(n\pi)}. \tag{C.23}$$

C.2.2 Gamma function

The Gamma function is defined to be an extension of the factorial to complex and real number arguments. Thus, for an integer argument, the Gamma function reduces to

$$\Gamma(n) = (n-1)!. \tag{C.24}$$

If $\Re(z) > 0$, it has the integral representation

$$\Gamma(z) = \int_0^\infty \exp(-t)t^{z-1}\mathrm{d}t. \tag{C.25}$$

The Gamma function may be recast as

$$\Gamma(z) = z^z \int_0^\infty \exp(z(\log(t) - t))\mathrm{d}t, \tag{C.26}$$

which can be approximated as (Stirling's approximation)

$$\Gamma(z) \approx z^z \exp(-z) \int_{-\infty}^{\infty} \exp(-zp^2/2)\mathrm{d}p \quad \text{(C.27)}$$

$$\Gamma(z) \approx z^z \exp(-z)\sqrt{\frac{2\pi}{z}}. \quad \text{(C.28)}$$

C.2.3 Hypergeometric function

The hypergeometric function ${}_pF_q(a_1, \dots, a_p; b_1, \dots, b_q; x)$ is a function defined in forms of a hypergeometric series, that it, the ratio of successive terms is given by

$$\frac{c_{k+1}}{c_k} = \frac{(k+a_1)(k+a_2)\dots(k+a_p)}{(k+b_1)(k+b_2)\dots(k+b_p)(k+1)}x, \quad \text{(C.29)}$$

where the terms $(k+1)$ is present for historical reasons.

C.3 Formulae

$$\int_0^{\infty} \mathrm{e}^{-x} x^{\gamma-1} L_n^{\mu}(x)\mathrm{d}x = \frac{\Gamma(\gamma)\Gamma(1+\mu+n-\gamma)}{n!\Gamma(1+\mu-\gamma)} \quad \text{for } \Re[\gamma] > 0 \quad \text{(C.30)}$$

$$\int_0^{\infty} x^{\nu-1}\mathrm{e}^{-\frac{\beta}{x}-\gamma x}\mathrm{d}x = 2\left(\frac{\beta}{\gamma}\right)^{\frac{\nu}{2}} K_v(2\sqrt{\beta\gamma}) \quad \text{for } \Re[\gamma] > 0, \Re[\beta] > 0 \quad \text{(C.31)}$$

$$\int_0^{\infty} \frac{J_\nu(bx)x^{\nu+1}}{(a^2+x^2)^{\mu+1}}\mathrm{d}x = \frac{a^{\nu-\mu}b^{\mu}}{2^{\mu}\Gamma(\mu+1)}K_{\nu-\mu}(ab) \quad \text{(C.32)}$$

Bibliography

M. Abramowitz and I.A. Stegun. *Handbook of Mathematical Functions with Formulas, Graphs, and Mathematical Tables.* Dover Publications, New York, 1972.

W. Alpers and I. Hennings. "A theory of the imaging mechanism of underwater bottom topography by real and syntethic aperture radar". *J. Geo. Res.*, 89(6): 10529–10546, Nov 1984.

V. Anastassopoulos, G.A. Lampropoulos, A. Drosopoulos, and M. Rey. "high resolution radar clutter statistics". *IEEE Trans. Aero. Elec. Syst.*, 35(1):43–60, Jan 1999.

D. Applebaum. *Lévy processes and stochastic calculus*, volume 93 of *Cambridge studies in advanced mathematics.* Cambridge Univ. Press, 2004.

R. Bakker, B. Currie, and S. Haykin. *"Two new strategies for target detection in sea clutter"*, chapter 6. Adaptive signal processing. Wiley Interscience, Hoboken, NJ, 2007. *Eds:* S. Haykin.

A. Balleri, A. Nehorai, and J. Wang. "Maximum likelihood estimation for compound-Gaussian clutter with inverse Gamma texture". *IEEE Trans. Aerosp. Electron. Syst.*, 43(2):775–780, Apr 2007.

M.S. Bartlett. *An Introduction to Stochastic Processes.* Cambridge Univ. Press, Cambridge, 1966.

P. Beckmann and A. Spizzichino. *The scattering of electromagnetic waves from rough surfaces.* Artech House, Inc.,, Norwood, MA, 1987. *Eds:* P. Beckmann and A. Spizzichino.

J. Blackledge. Book review. *Waves Random Complex Media*, 19:367, 2009.

D. Blacknell and R.J.A. Tough. Clutter discrimination in polarimetric sar imagery. In *SAR and Passive Microwave Sensing*, volume 2584(1), pages 188–199. SPIE, 1995. *Eds:* G. Franceschetti, C.J. Oliver, J.C. Shiue and S. Tajbakhsh.

F. Bloch. "Nuclear Induction". *Phys. Rev.*, 70(7-8):460–474, Oct 1946.

A.L. Bowley. "Births and Population in Great Britain". *The Economic Journal*, 34 (34):188–192, 1924.

T Bucciarelli, P. Lombardo, and S. Tamburrini. "Optimum CFAR detection against compound Gaussian clutter with partially correlated texture". In *IEE Proc. Radar, sonar and navigation*, volume 143, pages 95–104, 1996.

E. Conte, A. De Maio, and C. Galdi. "Statistical validation of the compound-Gaussian model on clutter data from IPIX radar". In *RADAR 2004*, Toulouse.

Y. Delignon and W. Pieczynski. "Modelling non-Rayleigh speckle distribution in SAR images". *IEEE Trans. Geosci. Remote Sens.*, 40(6):1430–1435, June 2002.

Y. Delignon, R. Garello, and A. Hillion. "Statistical modelling of ocean SAR images". *IEE Proc. Radar, Sonar Navig.*, 144(6):95–99, 1997.

V. Ditt and J.F. Greenleaf. "Ultrasound echo envelope analysis using a homodyned K distribution signal model". *Ultrasound Imaging*, 16(4):265–287, Oct 1994.

J.L. Doob. "The Brownian Movement and Stochastic Equations". *Ann. Math.A*, 43: 351–369, Apr 1942.

A. Einstein. "On the movement of small particles suspended in statoinary liquids required by the molecular-kinetic theory of heat". *Annalen der Physik*, 17:549–560, 1905.

A. Farina, F. Gini, M.V. Greco, and L. Verrazzani. "High resolution sea clutter data: statistical analysis of recorded live data". *IEE Proc. Radar, Sonar and Navigation*, 18(3):121–130, June 1997.

F.A. Fay, J. Clarke, and R.S. Peters. "Weibull distribution applications to sea clutter". *IEE Conf. Publ.*, 155:1012, 1977.

P. Fayard and T.R. Field. "Optimal inference of the scattering cross-section through the phase de-coherence". *Waves Rand. Comp. Media*, 18(4):571–584, Nov 2008.

P. Fayard and T.R. Field. "Optimal inference of the inverse Gamma texture for a compound-Gaussian clutter". In *2009 IEEE ICASSP*, pages 2969–2972, Apr 2009.

P. Fayard and T.R. Field. "Inference of a generalized texture for a compound–Gaussian clutter". *IET Radar, Sonar and Navigation*, 4(2):187–194, Apr 2010a.

P. Fayard and T.R. Field. "Estimation of the K–scattered amplitude in additive noise". *IEEE Aero. Elec. Syst.*, 46(4), October 2010b.

P. Fayard and T.R. Field. "Discrete models for scattering populations". *Journal Appplied Probabilities*, 2010c. under review.

P. Fayard and T.R. Field. "Geometrical implications of the compound representation for weakly scattered amplitudes". *Waves Rand. Comp. Media*, 2011. in press.

T. Feng, T.R. Field, and S. Haykin. "SDE theory applied to wireless channels". *IEEE Trans. Commun.*, 55(8):1478–1483, Aug 2007.

T. R. Field. *"Spin diffusion – a new perspective in magnetic resonance imaging"*, chapter 5. New Directions in Statistical Signal Processing: From Systems to Brain. MIT Press, Cambridge, MA, 2006. *Eds:* S. Haykin , J. Pincipe, T. Sejnowski and J. McWhirter.

T. R. Field. *Electromagnetic scattering from random media*, volume 144 of *International Series of Monographs on Physics*. Oxford Univ. Press, 2009.

T. R. Field and A.D. Bain. "Origins of Spin Noise". *Appl. Magn. Reson.*, 2009.

T.R. Field. "Observability of the scattering cross-section through phase decoherence". *J. Math. Phys.*, 46(6):063305 1–8, June 2005.

T.R. Field and R.J.A. Tough. "Diffusion processes in electromagnetic scattering generating K–distributed noise". *Proc. R. Soc. Ser. A*, 459:2169–2193, 2003a.

T.R. Field and R.J.A. Tough. "Stochastic dynamics of the scattering amplitude generating K-distributed noise". *J. Math. Phys.*, 44(11):5212–5223, Nov 2003b.

T.R. Field and R.J.A. Tough. "Dynamical models of weak scattering". *J. Math. Phys.*, 46:13302–13320, Jan 2005.

T.R. Field and R.J.A. Tough. "Coupled dynamics of populations supported by discrete sites and their continuum limit (in press, appear in September issue)". *Proc. R. Soc. Ser. A*, 2010.

J.L. Forman and M. Sørensen. "The Pearson Diffusions: A Class of Statistically Tractable Diffusion Processes". *Scand. J. Stat.*, 35(3):438–465, Apr 2008.

J. García-Ojalvo and R. Roy. "Noise amplification in a stochastic Ikeda model". *Phys. Lett. A*, 224:51–56, February 1996.

F. Gini, M.V. Greco, M. Diani, and L. Verrazzani. "Performance analysis of two adaptive radar detectors against non-Gaussian real sea clutter data". *IEEE Trans. Aerosp. Electron. Syst.*, 36(4):1429–1439, Oct 2000.

H. Goldstein. *Sea echo in propagation of short radio waves*, volume 13 (6) of *MIT Radiation Laboratory Series.* DE Kerr. McGraw-Hill, New York, NJ, 1951.

I.S. Gradshteyn and I.M. Ryzhik. *Table of Integrals, Series, and Products.* Academic Press, New York, 1967.

S. Guillouzic, I. L'heureux, and A. Longtin. "Small delay approximation of stochastic delay differential equations". *Phys. Rev. E*, 59:3970–3982, April 1999.

S. Haykin and S. Puthusserypady. "Chaotic dynamics of sea clutter". *Chaos*, 7: 777–802, December 1997.

C.W. Helstrom. *Statistical theory of signal detection.* Pergamon, Oxford, 1960.

D.J. Higham. "An Algorithmic Introduction to Numerical Simulation of Stochastic Differential Equations". *SIAM Review*, 43(3):525–546, Sep 2001.

D. Holliday, G. St-Cyr, and N. E. Woods. "Comparison of a new radar ocean imaging model with SARSEX internal wave image data". *Int. J. Remote Sensing*, 8:1423–1430, September 1987.

M. M. Horst, F. B. Dyer, and M. T. Tuley. "Radar sea clutter model". In *Int. Conf. Antenna Propag., London, England, Nov 28-30, 1978, Proceedings. Part 2. (A80-15812 04-32) London, IET, 1978, p. 6-10.*, pages 6–10, 1978.

B. A. Hughes. "The effect of internal waves on surface wind waves 2. Theoretical analysis". *J. Geo. Res.*, 83:455–465, January 1978.

M. Jahangir and C. J. Oliver. *Weak scattering model applied to coherent sonar images*, volume 3217 of *Image Processing, Signal Processing, and SAR for Remote Sensing*, pages 98–103. Proc. SPIE, 1997. *Eds:* Desachy, J, and Tajbakhsh, S.

E. Jakeman. "On the statistics of K–distributed noise". *J. Phys. A*, 13:31–48, Jan 1980.

E. Jakeman. "Discrete population processes derived from quantum optics". In *Rank Prize Mini-Symposium Grasmere*, 2005.

E. Jakeman and P.N. Pusey. "A model for non-Rayleigh sea echo". *IEEE Trans. Ant. Prop.*, 24:806–814, Nov. 1976.

E. Jakeman and P.N. Pusey. "Significance of K Distributions in Scattering Experiments". *Phys. Rev. Lett.*, 40(9):546–550, Feb 1978.

E. Jakeman and R.J.A. Tough. "The generalized K–distribution: a statistical model for weak scattering". *J. Opt. Soc. Am. A.*, 4(9):1764–1772, Sep 1987.

E. Jakeman and R.J.A. Tough. "Non-Gaussian models for the statistics of scattered waves". *Adv. Phys.*, 37(5):471–529, Oct 1988.

E. Jakeman and S.M. Watson. "Intensity-weighted phase-derivative statistics". *J. Opt. Soc. Am. A*, 18(9):2121–2131, Sep 2001.

J.K. Jao. "Amplitude distribution of composite terrain radar clutter and the K–distribution". *IEEE Trans. Antennas Propag.*, 32:1049–1062, Oct 1984.

B.H. Jeffreys and H. Jeffreys. *Methods of mathematial physics.* Cambridge Univ. Press, Cambridge, UK, 3rd edition, 1956.

I.R. Joughin, D.B. Percival, and D.P. Winebrenner. "Maximum likelihood estimation of K distribution parameters for SAR data". *IEEE Trans. Geosci. Remote Sens.*, 31(5):989–999, Sep 1993.

E.W. Kamen and J. Su. *Introduction to optimal estimation.* Springer NY, 1984.

I. Karatzas and E.S. Shreve. *Brownian Motion and Stochastic Calculus.* Springer-Verlag, New York, 1988.

J.F. Kenney and E.S. Keeping. *Mathematics of Statistics: Part 2.* Van Nostrand, Princeton, NJ, 2nd edition, 1951.

H.A. Kramers. "Brownian motion in a field of force and the diffusion model of chemical reactions". *Physica*, 4:284–304, Apr 1940.

B. Lacaze. "A stochastic model for backscattering on the sea". *Waves Rand. Comp. Media*, 16:69–74, February 2006.

T. Lamont-Smith, K.D. Ward, and D. Walker. "A comparison of EM scattering results and radar sea clutter". In *RADAR 2002*, pages 439–443.

P. H. Y. Lee, J. D. Barter, K. L. Beach, B. M. Lake, H. Rungaldier, H. R. Thompson, and R. Yee. "Scattering from breaking gravity waves without wind". *IEEE Trans. Ant. Prop.*, 46:14–26, January 1998.

M.W. Long. *Radar reflectivity of land and sea.* Artech House, Boston, MA, 1983.

D. Middleton. "Canonical and quasi-canonical probability models of class A interference". *IEEE Trans. Elec. Comp.*, 25:76–106, May 1983.

D. Middleton. "New physical-statistical methods and models for clutter and reverberation: the KA distribution and related probability structures". *IEEE J. Ocean Eng.*, 24(3):261–184, 1999.

J. Minkoff. *Signal processing fundamentals and applications for communications and sensing systems.* Artech House, Norwood, MA, 2002.

J.E. Moyal and M.S. Bartlett. "Quantum mechanics as a statistical theory". In *Proc. Cambridge Philo. Soc.*, volume 45, page 99, 1949.

N. Müller and A. Jerschow. "Nuclear spin noise imaging". *Proc. Nat. Acad. Sc.*, 103: 6790–6792, May 2006.

J.P. Nolan. *Stable Distributions: Models for Heavy Tailed Data.* Birkhäuser, 2005.

A.S. Novozhilov, G.P. Karev, and E.V. Koonin. "Biological applications of the theory of birth-and-death processes ". *Briefings in Bioinformatics*, 7(1):70–85, Feb 2006.

T. Ohira. "Oscillatory correlation of delayed random walks". *Phys. Rev. E*, 55: 1255–1258, February 1997.

B. Øksendal. *Stochastic Differential Equations: An Introduction with Applications.* Springer, Berlin, 5$^{\text{th}}$ edition, 1988.

A. Papoulis. *Probability, random variables and stochastic processes.* McGraw–Hill, New York, 2$^{\text{nd}}$ edition, 1984.

E.S. Pearson. *Research papers in statistics*, chapter The Neymann-Pearson story. John Wiley and Sons, London, 1966. *Ed:* F.N. David.

K. Pearson. "Second Supplement to a Memoir on Skew Variation". *Phil. Trans. A*, 216:191–214, 1916.

S.O. Rice. "Reflection of electromagnetic waves from slightly rough surfaces". *Comm. on Pure Appl. Math.*, 4(2):351–378, Apr 1951.

H. Risken. *The Fokker–Planck Equation.* Springer, Berlin, 1989.

J. Salmi, A. Richter, and V. Koivunen. "Detection and tracking of MIMO propagation path parameters using statespace approach". *IEEE Trans. Sig. Proc*, 57(4):1538–1550, 2009.

D.A. Shnidman. "Radar detection probabilities and their calculation". *IEEE Trans. Aero. Elec. Syst.*, 31(3):928–950, 1995.

M.I Skolnik. *Introduction to radar systems.* McGraw-Hill, Berlin, 1980.

P. Swerling. "Radar probability of detection for fluctuating targets". *IRE Trans IT-6*, pages 269–308, 1960.

P. Swerling. "Radar probability of detection for some additional fluctuating target cases". *IEEE Trans. Aero. Elec. Syst.*, 33:698–709, April 1997.

S. Tavaré. *Mathematical evolutionary theory*, chapter 3. The genealogy of the birth, death and immigration process. Princeton Univ. Press, Berlin, 1987. *Ed:* M.W. Feldman.

R.J.A. Tough. "A Fokker–Planck description of K–distributed noise". *J. Phys. A*, 20:561–567, Feb 1987.

R.J.A. Tough and K.D. Ward. "The correlation properties of Gamma and other non-Gaussian processes generated by memoryless nonlinear transformation". *J. Phys. D*, 32:3075–3084, 1999.

R.J.A. Tough, D. Blacknell, and S. Quegan. "A statistical description of polarimetric and interferometric SAR data". *Proc. R. Soc. A*, 449:567–589, 1995.

G. Trunk and S. George. "Detection of Targets in Non-Gaussian Sea Clutter". *IEEE Trans. Aero. Elec. Syst.*, 6:620–628, September 1970.

C.P. Unsworth, M.R. Cowper, S. McLaughlin, and B. Mulgrew. "Re-examining the nature of radar sea clutter". *IEE Proc.: Radar, Sonar and Navigation*, 149(3): 105–114, June 2002.

G.R. Valenzuela. "Reflection of electromagnetic waves from slightly rough surfaces". *Boundary-Layer Meteorology*, 13:61–85, Jan 1978.

Vyasa. *Bhagavad Gita.* Susil Gupta, Calcutta, before 3$^{\text{rd}}$ century BCE.

D. Walker. "Experimentally motivated model for low grazing angle radar Doppler spectra of the sea surface". *IEE Proc.: Radar, sonar and navigation*, 147(3):114–120, April 2000.

K.D. Ward. "Compound representation of high resolution sea clutter". *Elec. Lett.*, 17(16):561–563, Aug 1981.

K.D. Ward, R.J.A. Tough, and P.W. Shepherd. "Modelling sea clutter: correlation, resolution and non-Gaussian statistics". In *Proc. Radar 97*, pages 95–99.

K.D. Ward, R.J.A. Tough, and S. Watts. *Sea clutter: Scattering, the K-distribution and Radar Performance.* IEE Publishing, London, 2006.

S.M. Watson, E. Jakeman, and K.D. Ridley. "Phase statistics in non-Gaussian scattering". *J. Phys. A: Math. Gen*, 39:7621–7640, May 2006.

S. Watts. "Radar detection prediction in K-distributed sea clutter and thermal noise". *IEEE Trans. Aero. Elec. Syst.*, 17(16):613–620, Aug 1981.

S. Watts. "Radar detection prediction in sea clutter using the compound K-distribution". *IEE Proc. Comm., Radar Sig. Proc.,*, 132(7):613–620, Dec 1985.

L. Weng, J.M. Reid, P.M. Shankar, and K. Soetanto. "Ultrasound speckle analysis based on the K distribution". *J. Accoust. Soc. Am.*, 89(6):2992–2995, June 1991.

S. Wolfram. *The Mathematica Book.* Cambridge Univ. Press, Cambridge, 1999.

E. Wong. "The construction of a class of stationary Markoff processes". In *Amer. Math. Soc. Proc. XVIth Symp. Appl. Math*, pages 264–276, 1963.

J. Wright. "A new model for sea clutter". *IEEE Trans. Antennas Prop.*, 16:217–223, March 1968.

N. Yasuda. "The random walk model of human migration". *Theo. pop. bio.*, 7(2): 156–167, Apr 1975.

S. Ye, Y. Wang, and Y. Tseng. "A Jamming-Based MAC Protocol for Wireless Multihop Ad Hoc Networks". In *Vehicular Technology Conference*, volume 3, pages 1396–1400, 2003.

M. Yor and B. Bru. "comments on the life and mathematical legacy of wolfgang doeblin". *Finance and Stochastics*, 6(1):3–47, 2002.

List of Symbols

${}_2F_1$	Hypergeometric function	49
$\mathcal{A}$	RCS characteristic frequency	26
$\mathcal{B}$	Speckle characteristic frequency	38
$\mathcal{N}(a,b)$	Normal distribution, mean a and variance b	53
$\mathcal{P}_N(t)$	Probability density for the number of scatterers N_t	22
C_N	Characteristic function for the random walk amplitude	17
$D^{(n)}$	Kramers–Moyal moments of the scatterers' density $\mathcal{P}_N(t)$	23
E	Modulus of the random walk amplitude	17
G_N	Generation transition function of the population model	22
I	n^{th} modified Bessel function of the first kind	50
I_t	In-phase component of the strongly scattered amplitude ψ_t	50
J_n	n^{th} Bessel function of the first kind	17
K_n	n^{th} modified Bessel function of the second kind	19
L_n^α	Laguerre polynomials	50
$\overline{N}$	Time asymptotic population of the scatterers' population N_t	18
N_t	Number of scatterers	16
Q_t	Quadrature-phase component of the strongly scattered amplitude ψ_t	45
R_N	Recombination transition function of the population model	22
R_t	Strongly scattered amplitude modulus $R_t = \lvert\psi_t\rvert$	43
R_{fg}	Cross-correlation function $R_{fg}(\tau) = \langle f(t+\tau)g(t)\rangle$	82
R	RCS relative variance $R = \mathrm{Var}[x]/\langle x\rangle^2$	74
S_t	Weak scattering vector $S_t = (x_t, Z_t, \Theta_t)^{\mathrm{tr}}$	92

S_z	Power spectral density $S_z(\omega) = \mathcal{F}[R_z(\tau)]$	52
$W_t^{(j)}$	Phase Wiener process for the j^{th} phasor of the random walk	38
$W_t^{(x)}$	RCS Wiener process	40
Z_t	Weakly scattered intensity $Z_t = \lvert\Psi_t\rvert^2$	48
a	Pearson diffusions volatility parameter	28
a_j	Form factor of the j^{th} phasor of the random walk	15
b	Pearson diffusions volatility parameter	28
b_t	Drift coefficient of a FPE	26
b	Scale parameter K–distribution	19
b^i	Drift coefficient of the weak scattering vector S_t^i	92
c	Pearson diffusions volatility parameter	28
$\mathrm{d}q_t$	Ito differential of the process q_t	11
$\mathrm{d}q_t^2$	Diffusion coefficient $\mathrm{d}q_t\mathrm{d}q_t$	11
e_t	Coherent offset for a weakly scattered amplitude $\Psi_t = \psi_t + e_t$	46
$f_t^{(\Theta)}$	Weak scattering angular volatility due to the RCS	90
$f_t^{(Z)}$	Weak scattering radial volatility due to the RCS	90
h_t	Wiener filter impulse response	81
m	Pearson diffusions drift parameter	28
n_i	Sampling process, i.i.d random variables $\sim \mathcal{N}(0,1)$	62
p	Pearson distribution parameter (Beta and Beta prime)	80
p	Parameter of the population model for Pearson diffusions	32
q	Pearson distribution parameter (Beta and Beta prime)	29
r_t	RCS square-root $r_t = \sqrt{x_t}$	75
t	Time	22
u_t	Speckle intensity $u_t = \lvert\gamma_t\rvert^2$	52
w_t	Phase-wrapped process $w_t = \exp(i\theta_t)$	61
x_t	Radar cross-section (texture) $x_t = \lim_{N_t\to\infty}[N_t/\overline{N}]$	20
x_t^{sm}	Smoothed RCS, average of $z_i\delta\theta_i^2$ over a window $\boldsymbol{\Delta}$	66
z	Strongly scattered intensity $z_t = \lvert\psi_t\rvert^2$	3
$\widetilde{z}_t$	Noisy scattered intensity $\widetilde{z}_t = \lvert\widetilde{\psi}_t\rvert^2$ for $\widetilde{\psi}_t = \psi_t + \Gamma_t$	80

$\Gamma(\alpha, b)$	Gamma distribution with parameters α and b	20
$\boldsymbol{\Delta}$	Smoothing window around t_0, $\boldsymbol{\Delta} = [t_0 - \Delta\delta_t, t_0 + \Delta\delta_t]$	62
Δ	Number of samples per smoothing window	62
Δ^{opt}	Optimal smoothing window length	67
$\Delta^{(j)}$	Phase initialization of the j^{th} phasor of the random walk	38
Θ_t	Weakly scattered phase $\Theta_t = \angle\Psi_t$	48
Λ	Detection likelihood ratio	4
$\Pi_t(z)$	Partition function $\Pi_t(z) = \langle z^{N_t} \rangle$ for $N_t e$	25
Σ^{ij}	Volatility coefficient of the weak scattering vector S_t^i	92
$\Sigma_t^{(q,p)}$	Diffusion coefficient $\mathrm{d}q_t \mathrm{d}p_t/\mathrm{d}t$	11
Ψ_t	Weakly scattered amplitude $\Psi_t = \psi_t + e_t$	46
α	Shape parameter for the K-distribution	18
α_t	Wiener component for the dyad representation	96
α	Pearson distribution parameter (inverse Γ)	29
β	Pearson distribution parameter (Beta, Beta prime and inverse Γ)	29
β_t	Wiener component for the dyad representation	96
γ_t	Normalized Rayleigh amplitude (speckle) $\gamma_t = \lim_{N\to\infty}[\varrho_t^{(N_t)}/N_t^{\frac{1}{2}}]$	39
δ_t	Sampling interval	53
ϵ	Parameter for the population model of Pearson diffusions	32
ϵ_{sm}	Smoothing error for the RCS inference	66
ϵ_{xi}	Smoothing error for the RCS inference due to the x_i's	69
ϵ_{ni}	Smoothing error for the RCS inference due to the n_i's	72
θ_t	Scattered amplitude phase $\theta_t = \angle(\psi_t)$	3
λ	Parameter for population model (BDI and Pearson diffusions)	24
μ	Parameter for population model (BDI and Pearson diffusions)	24
ν	Parameter for population model (BDI and Pearson diffusions)	24
ξ_t	Speckle Wiener process derived from the $\{W_t^{(j)}\}$	39
$\varrho_t^{(N)}$	Scattered amplitude random walk	15
σ_t	Volatility coefficient of a FPE	26
$\phi_t^{(j)}$	Phase diffusion model for the j^{th} phasor of the random walk	15
ϕ_t	Weak amplitude fluctuations de-correlate w.r.t. the orthogonal dyad rotated by angle ϕ_t from angular/radial directions	3

$\Gamma(\alpha, b)$	Gamma distribution with parameters α and b	20
$\boldsymbol{\Delta}$	Smoothing window around t_0, $\boldsymbol{\Delta} = [t_0 - \Delta\delta_t, t_0 + \Delta\delta_t]$	62
Δ	Number of samples per smoothing window	62
Δ^{opt}	Optimal smoothing window length	67
$\Delta^{(j)}$	Phase initialization of the j^{th} phasor of the random walk	38
Θ_t	Weakly scattered phase $\Theta_t = \angle\Psi_t$	48
Λ	Detection likelihood ratio	4
$\Pi_t(z)$	Partition function $\Pi_t(z) = \langle z^{N_t}\rangle$ for $N_t e$	25
Σ^{ij}	Volatility coefficient of the weak scattering vector S_t^i	92
$\Sigma_t^{(q,p)}$	Diffusion coefficient $\mathrm{d}q_t \mathrm{d}p_t/\mathrm{d}t$	11
Ψ_t	Weakly scattered amplitude $\Psi_t = \psi_t + e_t$	46
α	Shape parameter for the K–distribution	18
α_t	Wiener component for the dyad representation	96
α	Pearson distribution parameter (inverse Γ)	29
β	Pearson distribution parameter (Beta, Beta prime and inverse Γ)	29
β_t	Wiener component for the dyad representation	96
γ_t	Normalized Rayleigh amplitude (speckle) $\gamma_t = \lim_{N\to\infty}[\varrho_t^{(N_t)}/N_t^{\frac{1}{2}}]$	39
δ_t	Sampling interval	53
ϵ	Parameter for the population model of Pearson diffusions	32
ϵ_{sm}	Smoothing error for the RCS inference	66
ϵ_{xi}	Smoothing error for the RCS inference due to the x_i's	69
ϵ_{ni}	Smoothing error for the RCS inference due to the n_i's	72
θ_t	Scattered amplitude phase $\theta_t = \angle(\psi_t)$	3
λ	Parameter for population model (BDI and Pearson diffusions)	24
μ	Parameter for population model (BDI and Pearson diffusions)	24
ν	Parameter for population model (BDI and Pearson diffusions)	24
ξ_t	Speckle Wiener process derived from the $\{W_t^{(j)}\}$	39
$\varrho_t^{(N)}$	Scattered amplitude random walk	15
σ_t	Volatility coefficient of a FPE	26
$\phi_t^{(j)}$	Phase diffusion model for the j^{th} phasor of the random walk	15
ϕ_t	Weak amplitude fluctuations de-correlate w.r.t. the orthogonal dyad rotated by angle ϕ_t from angular/radial directions	3

$\chi(n)$ Chi distribution 61
ψ_t Normalized scattered amplitude $\psi_t = \lim_{N\to\infty}[\varrho_t^{(N_t)}/\overline{N}^{1/2}]$ 40
$\widetilde{\psi}$ Noisy scattered amplitude $\widetilde{\psi}_t = \psi_t + \Gamma_t$ 80
$\widehat{\psi}$ Optimal estimation of the noisy $\widetilde{\psi}_t$ 81
ω_t Normally distributed sample for SDE discretization 53

List of Acronyms

ACF	Auto-Correlation Function
BDI	Birth-Death-Immigration
CFAR	Constant False Alarm Rate
COU	Complex Ornstein-Uhlenbeck
FID	Free Induction Decay
FIR	Finite Impulse Response
FPE	Fokker-Planck Equation
FWHM	Full Width at Half Maximum
GK	Generalized K–distribution
HK	Homodyned K–distribution
H/V	Horizontal / Vertical polarization
MMSE	Minimum Mean Square Error
MSE	Mean Square Error
NMR	Nuclear Magnetic Resonance
ODE	Ordinary Differential Equation
PDE	Partial Differential Equation
PMF	Probability Mass Function
PSD	Power Spectral Density
RCS	Radar Cross-Section
SAR	Synthetic Aperture Radar
SDE	Stochastic Differential Equation
SNR	Signal to Noise Ratio
w.r.t.	with respect to